

1 LEVERAGING MULTI-MESSENGER ASTROPHYSICS FOR DARK MATTER SEARCHES

By

Daniel Nicholas Salazar-Gallegos

A DISSERTATION

Submitted to
Michigan State University
in partial fulfillment of the requirements
for the degree of

Physics—Doctor of Philosophy
Computational Mathematics in Science and Engineering—Dual Major

Today

ABSTRACT

3 I did Dark Matter with HAWC and IceCube. I also used Graph Neural Networks

⁴ Copyright by

⁵ DANIEL NICHOLAS SALAZAR-GALLEGOS

⁶ Today

ACKNOWLEDGMENTS

8 I love my friends. Thanks to everyone that helped me figure this out. Amazing thanks to the people
9 at LANL who supported me. Eames, etc Dinner Parties Jenny and her child Kaydince Kirsten, Pat,
10 Andrea Family. You're so far but so critical to my formation. Unconditional love. Roommate

TABLE OF CONTENTS

12	LIST OF TABLES	vii
13	LIST OF FIGURES	viii
14	LIST OF ABBREVIATIONS	xv
15	CHAPTER 1 INTRODUCTION	1
16	CHAPTER 2 DARK MATTER IN THE COSMOS	2
17	2.1 Introduction	2
18	2.2 Dark Matter Basics	3
19	2.3 Evidence for Dark Matter	4
20	2.4 Searching for Dark Matter: Particle DM	11
21	2.5 Sources for Indirect Dark Matter Searches	16
22	2.6 Multi-Messenger Dark Matter	18
23	CHAPTER 3 HIGH ALTITUDE WATER CHERENKOV (HAWC) OBSERVATORY	21
24	3.1 The Detector	21
25	3.2 Events Reconstruction and Data Acquisition	21
26	3.3 Remote Monitoring	21
27	CHAPTER 4 ICECUBE NEUTRINO OBSERVATORY	22
28	4.1 The Detector	22
29	4.2 Events Reconstruction and Data Acquisition	22
30	4.3 Northern Test Site	22
31	CHAPTER 5 GLORY DUCK: MULTI-WAVELENGTH SEARCH FOR DARK MATTER ANNIHILATION TOWARDS DWARF SPHEROIDAL GALAXIES	23
32	5.1 Introduction	23
33	5.2 Dataset and Background	25
34	5.3 Analysis	26
35	5.4 Likelihood Methods	31
36	5.5 HAWC Results	37
37	5.6 Glory Duck Combined Results	40
38	5.7 HAWC Systematics	45
39	5.8 J -factor distributions	46
40	5.9 Discussion and Conclusions	52
43	CHAPTER 6 MULTITHREADING HAWC ANALYSES FOR DARK MATTER SEARCHES	56
44	6.1 Introduction	56
45	6.2 Dataset and Background	56
46	6.3 Analysis	58

48	6.4	Likelihood Methods	61
49	6.5	Computational Methods: Multithreading	62
50	6.6	Analysis Results	68
51	6.7	Systematics	73
52	6.8	Conclusion and Discussion	73
53	CHAPTER 7	HEAVY DARK MATTER ANNIHILATION SEARCH WITH ICE-CUBE'S NORTH SKY TRACK DATA	75
54	7.1	Introduction	75
55	7.2	Dataset and Background	76
56	7.3	Analysis	77
58	CHAPTER 8	NU DUCK	84
59	APPENDIX A	MULTI-EXPERIMENT SUPPLEMENTARY FIGURES	85
60	APPENDIX B	MULTITHREADING DARK MATTER ANALYSES SUPPLEMENTARY MATERIAL	86
61	B.1	Remaining Spectral Models	86
62	B.2	<code>mpu_analysis.py</code>	87
63	B.3	Comparison with Glory Duck	96
65	APPENDIX C	ICECUBE HEAVY DARK MATTER ANALYSIS SUPPLEMENTARY MATERIAL	99
66	C.1	Docker Image for Oscillating Neutrino Spectra	99
68	BIBLIOGRAPHY	102

LIST OF TABLES

<p>70 Table 5.1 Summary of the relevant properties of the dSphs used in the present work. Column 1 lists the dSphs. Columns 2 and 3 present their heliocentric distance and galactic coordinates, respectively. Columns 4 and 5 report the J-factors of each source given from the \mathcal{GS} and \mathcal{B} independent studies and their estimated $\pm 1\sigma$ uncertainties. The values $\log_{10} J$ (\mathcal{GS} set) [45] correspond to the mean J-factor values for a source extension truncated at the outermost observed star. The values $\log_{10} J$ (\mathcal{B} set) [47] are provided for a source extension at the tidal radius of each dSph. Bolded sources are within HAWC's field of view and provided to the Glory Duck analysis.</p> <p>79 Table 5.2 Summary of dSph observations by each experiment used in this work. A ‘-’ indicates the experiment did not observe the dSph for this study. For Fermi-LAT, the exposure at 1 GeV is given. For HAWC, $\Delta\theta$ is the absolute difference between the source declination and HAWC latitude. HAWC is more sensitive to sources with smaller $\Delta\theta$. For IACTs, we show the zenith angle range, the total exposure, the energy range, the angular radius θ of the signal or ON region, the ratio of exposures between the background-control (OFF) and signal (ON) regions (τ), and the significance of gamma-ray excess in standard deviations, σ.</p> <p>88 Table 6.1 Summary of the relevant properties of the dSphs used in the present work. Column 1 lists the dSphs. Columns 2 and 3 present their heliocentric distance and galactic coordinates, respectively. Column 4 reports the J-factors of each source given from the \mathcal{LS} studies and estimated $\pm 1\sigma$ uncertainties. The values $\log_{10} J$ (\mathcal{LS} set) [65] correspond to the mean J-factor values for a source extension truncated at 0.5°.</p> <p>94 Table 6.2 Timing summaries for analyses for serial and multithreaded processes. M tasks is the number of functional-parallel tasks ran for the computation. $T_{p,c}$ is a single run time in hours:minutes:seconds for runs utilizing p nodes and c threads. Runs are run interactively on the same computer to maximize consistency. Empty entries are indicated with ‘-’. (.) entries are estimated entries extrapolated from data earlier in the column.</p> <p>100 Table 6.3 Speed up summaries for analyses for serial and multithreaded processes. M tasks is the number of functional-parallel tasks ran for the computation. $S_{p,c}$ is a single speedup comparison for runs utilizing p nodes and c threads. $[\cdot]$ are the estimated speedups calculated from Tab. 6.2, Eq. (6.10), and Eq. (6.5). Empty entries are indicated with ‘-’.</p> <p>105 Table 7.1 TODO: fill me daddy</p> <p>106 Proof I know how to include</p>	<p>31</p> <p>32</p> <p>62</p> <p>66</p> <p>68</p> <p>83</p>
--	---

LIST OF FIGURES

108	Figure 2.1	Rotation curve fit to NGC 6503 from [7]. Dashed line is the contribution 109 from visible matter. Dotted curves are from gas. Dash-dot curves are from 110 dark matter (DM). Solid line is the composite contribution from all matter 111 and DM sources. Data are indicated with bold dots with error bars. Data 112 agree strongly with a matter + DM composite prediction.	5
113	Figure 2.2	Light from distant galaxy is bent in unique ways depending on the distribution 114 of mass between the galaxy and Earth. Yellow dashed lines indicate where 115 the light would have gone if the matter were not present [8].	7
116	Figure 2.3	(left) Optical image of galactic cluster 1E0657-558. (right) X-ray image of the 117 cluster with redder meaning hotter and higher baryon density. (both) Green 118 contours are reconstruction of gravity contours from weak lensing. White 119 rings are the best fit mass maxima at 68.3%, 95.5%, and 99.7% confidence. 120 The matter maxima of the clusters are clearly separated from x-ray maxima. [9]	8
121	Figure 2.4	Plank CMB sky. Sky map features small variations in temperature in primor- 122 dial light. These anisotropies are used to make inferences about the universe's 123 energy budget and developmental history. [10]	9
124	Figure 2.5	Observed Cosmic Microwave Background power spectrum as a function of 125 multipole moment from Plank [10]. Blue line is best fit model from Λ CDM. 126 Red points and lines are data and error, respectively.	10
127	Figure 2.6	Predicted power spectra of CMB for different $\Omega_m h^2$ values for fixed baryon 128 density from [11]. (left) Low $\Omega_m h^2$ increases the prominence of first and 129 second peaks. (middle) $\Omega_m h^2$ is most similar to the observed power spectrum. 130 The second and third peaks are similar in height. (right) $\Omega_m h^2$ is large which 131 suppresses the first peak and raises the prominence of the third peak.	10
132	Figure 2.7	The Standard Model (SM) of particle physics. Figure taken from http://www.quantumdiaries.org/2014/03/14/the-standard-model-a-beautiful-but-flawed-theory/	12
135	Figure 2.8	Simplified Feynman diagram demonstrating with different ways DM can 136 interact with SM particles. The 'X's refer to the DM particles whereas the 137 SM refer to fundamental particles in the SM. The large circle in the center 138 indicates the vertex of interaction and is purposely left vague. The colored 139 arrows refer to different directions of time as well as their respective labels. 140 The arrows indicate the initial and final state of the DM -SM interaction in time.	13

141	Figure 2.9 A single jet event in ATLAS detector from 2017 [16]. Jet momentum was 142 observed to be 1.9 TeV. Missing transverse momentum was observed to be 143 1.9 TeV compared to the initial transverse momentum of the event was 0. 144 Implied MET is traced by a red dashed line in event display.	14
145	Figure 2.10 More detailed pseudo-Feynman diagram of particle cascade from dark matter 146 annihilation into 2 quarks. The quarks hadronize and down to stable particles 147 like γ or the anti-proton (p^-). Diagram pulled from ICRC 2021 presentation 148 on DM annihilation search [17].	15
149	Figure 2.11 Dark Matter (DM) decay spectrum for $b\bar{b}$ initial state and γ final state. Redder 150 spectra are for larger DM masses. Bluer spectra are light DM masses. x is a 151 unitless factor defined as the ratio of the mass of DM, m_χ , and the final state 152 particle energy E_γ . Figure from [19].	17
153	Figure 2.12 Different dark matter density profiles compared. Some models produce ex- 154 ceptionally large densities at small r [20].	18
155	Figure 2.13 The Milky Way Galaxy in photons (γ) and neutrinos (ν) [22]. The Galactic 156 center is at $l=0^\circ$ and is the brightest region in all panels. (top) An Optical 157 color image of the Milky Way galaxy seen from Earth. Clouds of gas and dust 158 obscure some light from stars. (2nd down) Integrated flux of γ -rays observed 159 by the Fermi-LAT telescope [23]. (middle) Expected neutrino emission 160 that corresponds with Fermi-LAT observations. (2nd up) Expected neutrino 161 emission profile after considering detector systematics of IceCube. (bottom) 162 Observed neutrino emission from region of the galactic plane. Substantial 163 neutrino emission was detected.	19
164	Figure 2.14 Dark Matter annihilation spectra for different final state particle and standard 165 model annihilation channels [24]. Photons (red), e^\pm (green), \bar{p} (blue), ν (black).	20
166	Figure 5.1 Sensitivities of five gamma-ray experiments compared to percentages of the 167 Crab nebula's emission and dark matter annihilation. Solid lines present 168 estimated sensitivities to power law spectra [FACT CHECK THIS] for each 169 experiment. Green lines are Fermi-LAT sensitivities where lighter green is 170 the sensitivity to the galactic center and dark green is its sensitivity to higher 171 declinations. Orange, red, and purple solid lines represent the MAGIC, HESS, 172 and VERITAS 50 hour sensitivities respectively. The maroon and brown lines 173 are the HAWC 1 year and 5 year sensitivities. Across four decades of gamma- 174 ray energy, these experiments have similar sensitivities on the order 10^{-12} 175 $\text{erg cm}^{-2}\text{s}^{-1}$. The dotted lines are estimated dark matter fluxes assuming 176 $m_\chi = 5 \text{ TeV}$ DM annihilating to bottom quarks (red), tau leptons (blue), 177 and W bosons (green). Faded gray lines outline percentage flux of the Crab 178 nebula. Figure is an augmented version of [25]	24

179	Figure 5.2	Effect of Electroweak (EW) corrections on expected DM annihilation spectrum for $\chi\chi \rightarrow W^-W^+$. Solid lines are spectral models that consider EW corrections. Dash-dot lines are spectral models without EW corrections. Red lines are models for $M_\chi = 1$ TeV. Blue lines represent models for $M_\chi = 100$ TeV. All models are sourced from the PPPC4DMID [44].	28
184	Figure 5.3	$\frac{dJ}{d\Omega}$ maps for Segue1 (top) and Coma Berenices (bottom). Origin is centered on the specific dwarf spheroidal galaxies (dSph). X and Y axes are the angular separation from the center of the dwarf. Plots of the remaining 11 dSph HAWC studied are linked in Fig. A.1.	30
188	Figure 5.4	Illustration of the combination technique showing a comparison between $-2 \ln \lambda$ provided by four instruments (colored lines) from the observation of the same dSph without any J nuisance and their sum, <i>i.e.</i> the resulting combined likelihood (thin black line). According to the test statistics of Equation (5.6), the intersection of the likelihood profiles with the line $-2 \ln \lambda = 2.71$ indicates the 95% C.L. upper limit on $\langle \sigma v \rangle$. The combined likelihood (thin black line) shows a smaller value of upper limit on $\langle \sigma v \rangle$ than those derived by individual instruments. We also show how the uncertainties on the J factor effects the combined likelihood and degrade the upper limit on $\langle \sigma v \rangle$ (thick black line). All likelihood profiles are normalized so that the global minimum $\widehat{\langle \sigma v \rangle}$ is 0. We note that each profile depends on the observational conditions in which a target object was observed. The sensitivity of a given instrument can be degraded and the upper limits less constraining if the observations are performed in non-optimal conditions such as a high zenith angle or a short exposure time.	35
203	Figure 5.5	38
204	Figure 5.6	HAWC TS values for best fit $\langle \sigma v \rangle$ versus m_χ for seven SM annihilation channels with J factors from \mathcal{GS} . The solid black line shows the combined best fit TS values. The colored, dashed lines are the TS values for each of the 13 sources HAWC studied.	39
208	Figure 5.7	HAWC Brazil bands at 95% confidence level on $\langle \sigma v \rangle$ versus DM mass for seven annihilation channels with J -factors from \mathcal{GS} [53]. The solid line represents the combined limit from 13 dSphs. The dashed line is the expected limit. The green band is the 68% containment. The yellow band is the 95% containment.	40

213	Figure 5.8	Upper limits at 95% confidence level on $\langle \sigma v \rangle$ in function of the DM mass for 214 eight annihilation channels, using the set of J factors from Ref. [53] (\mathcal{GS} set 215 in Table 5.1). The black solid line represents the observed combined limit, 216 the black dashed line is the median of the null hypothesis corresponding 217 to the expected limit, while the green and yellow bands show the 68% and 218 95% containment bands. Combined upper limits for each individual detector 219 are also indicated as solid, colored lines. The value of the thermal relic 220 cross-section in function of the DM mass is given as the red dotted-dashed 221 line [54].	41
222	Figure 5.9	Same as Fig. 5.8, using the set of J factors from Ref. [47, 55] (\mathcal{B} set in Table 5.1).	42
223	Figure 5.10	Comparisons of the combined limits at 95% confidence level for each of the 224 eight annihilation channels when using the J factors from Ref. [53] (\mathcal{GS} set in 225 Table 5.1), plain lines, and the J factor from Ref. [47, 55] (\mathcal{B} set in Table 5.1), 226 dashed lines. The cross-section given by the thermal relic is also indicated [54].	44
227	Figure 5.11	Comparisons of the combined limits at 95% confidence level for a point source 228 analysis and extended source using [53] \mathcal{GS} J-factor distributions and PPPC 229 [44] annihilation spectra. Shown are the limits for Segue1 which will have 230 the most significant impact on the combined limit. 6 of the 7 DM annihilation 231 channels are shown. Solid lines are extended source studies. Dashed lines 232 are point source studies. Overall, the extended source analysis improves the 233 limit by a factor of 2.	46
234	Figure 5.12	Same as Fig. 5.11 on Coma Berenices. This dSph also contributes signifi- 235 cantly to the limit. The limits are identical in this case.	47
236	Figure 5.13	Comparison of combined limits when correcting for HAWC's pointing sys- 237 tematic. All DM annihilation channels are shown. The solid black line is the 238 ratio between published limit to the declination corrected limit. The blue solid 239 line or "Combined_og" represented the limits computed for Glory Duck. The 240 solid orange line or "Combined_ad" represented the limits computed after 241 correcting for the pointing systematic.	48
242	Figure 5.14	Differential map of dJ/Ω from model built in Section 5.8.1 and profiles 243 provided directly from authors. (Top) Differential from Segue1. (bottom) 244 Differential from Coma Berenices. Note that their scales are not the same. 245 Segue1 shows the deepest discrepancies which is congruent with its large 246 uncertainties. Both models show anuli where unique models become apparent.	49

247	Figure 5.15 HAWC limits for Coma Berenices (top) and Segue1 (bottom) for two different 248 map sets. Blue lines are limits calculated on maps with poor model repre- 249 sentation. Orange lines are limits calculated on spatial profiles provided by 250 the authors of [45]. Black line is the ratio of the poor spatial model limits to 251 the corrected spatial models. The left y-axis measures $\langle\sigma v\rangle$ for the blue and 252 orange lines. The right y-axis measures the ratio and is unitless.	50
253	Figure 5.16 Comparisons between the J -factors versus the angular radius for the com- 254 putation of J factors from Ref. [53] (\mathcal{GS} set in Table 5.1) in blue and for 255 the computation from Ref. [47, 55] (\mathcal{B} set in Tab. 5.1) in orange. The solid 256 lines represent the central value of the J -factors while the shaded regions 257 correspond to the 1σ standard deviation.	53
258	Figure 5.17 Comparisons between the J -factors versus the angular radius for the computa- 259 tion of J factors from Ref. [53] (\mathcal{GS} set in Tab. 5.1) in blue and for the 260 computation from Ref. [47, 55] (\mathcal{B} set in Tab. 5.1) in orange. The solid 261 lines represent the central value of the J -factors while the shaded regions 262 correspond to the 1σ standard deviation.	54
263	Figure 6.1 Difference between spectral hypotheses from PPPC [44] and HDM [64]. 264 Shown is the expected DM annihilation spectrum for $\chi\chi \rightarrow W^-W^+$. Solid 265 lines are spectral models with EW corrections from the PPPC. Dash-dot lines 266 are spectral models from HDM. Red lines are models for $M_\chi = 1$ TeV. Blue 267 lines represent models for $M_\chi = 100$ TeV.	59
268	Figure 6.2 Photon spectra for $\chi\chi \rightarrow \gamma\gamma$ (left) and $\chi\chi \rightarrow ZZ$ (right) after Gaussian 269 convolution of line features. Both spectra have δ -features at photon energies 270 equal to the DM mass. Bluer lines are annihilation spectra with lower DM 271 mass. Redder lines are spectra from larger DM mass. All Spectral models are 272 sourced from the Heavy Dark Matter models [64]. Axes are drawn roughly 273 according to the energy sensitivity of HAWC.	60
274	Figure 6.3 $\frac{dJ}{d\Omega}$ maps for Coma Berenices, Draco, Segue1, and Sextans. Columns are 275 divided for the $\pm 1\sigma$ uncertainties in $dJ/d\Omega$ around the mean value from \mathcal{LS} 276 [65]. Origin is centered on the specific dwarf spheroidal galaxies (dSph). θ 277 and ϕ axes are the angular separation from the center of the dwarf	61
278	Figure 6.4 Infographic on how jobs and DM computation was organized in Section 5.3. 279 Jobs were built for each permutation of CHANS and SOURCES shown by the 280 left block in the figure. Each job, which took on the order 2 hrs to compute, 281 had the following work flow: 1. Import HAWC analysis software, 2 min to 282 run. 2. Load HAWC count maps, 5 min to run. 3. Load HAWC energy and 283 spatial resolutions, 4 min. 5. Load DM spatial source templates and spectral 284 models, less than 1 s. 6. Perform likelihood fit on data and model, about 8 285 min per DM mass. 7. Write results to file, less than 1s.	63

286	Figure 6.5	Graphic of Gustafson parallel coding pattern. f_s is the fraction of a program, in time, spent on serial computation. f_p is the fraction of computing time that is parallelizable. T_p is the total time for a parallel program to run. T_1 is the total time for a parallel program to run if only 1 processor is allocated. P_N is the N -th processor where it's row is the computation the processor performs. The Gustafson pattern is most similar to what is implemented for this analysis. Figure is pulled from [67].	64
293	Figure 6.6	Task chart for one multithreaded job developed for this project. Green blocks indicate a shared resource across the threads AND computation performed serially. Red blocks indicate functional parallel processing within each thread. 3 threads are represented here, yet many more can be employed during the full analysis. Jobs are defined by the SOURCE as these require unique maps to be loaded into the likelihood estimator. The m_χ , CHAN, and $\langle\sigma v\rangle$ variables are entered into the thread pool and allocated as evenly as possible across the threads.	66
301	Figure 6.7	HAWC upper limits at 95% confidence level on $\langle\sigma v\rangle$ versus DM mass for $\chi\chi \rightarrow b\bar{b}, t\bar{t}, u\bar{u}, d\bar{d}, s\bar{s}, c\bar{c}, gg, W^+W^-$, and hh . Limits are with \mathcal{LS} J - factors [65]. The solid line represents the observed combined limit. Dashed lines represent limits from individual dSphs.	69
305	Figure 6.8	HAWC upper limits at 95% confidence level on $\langle\sigma v\rangle$ versus DM mass for $\chi\chi \rightarrow \nu_e\bar{\nu}_e, \nu_\mu\bar{\nu}_\mu, \nu_\tau\bar{\nu}_\tau, e\bar{e}, \mu\bar{\mu}, \tau\bar{\tau}, \gamma\gamma$ and ZZ . Limits use \mathcal{LS} J factors [65]. The solid line represents the observed combined limit. Dashed lines represent limits from individual dSphs.	70
309	Figure 6.9	HAWC TS values for best fit $\langle\sigma v\rangle$ versus m_χ for SM annihilation channels: $\chi\chi \rightarrow b\bar{b}, t\bar{t}, u\bar{u}, d\bar{d}, s\bar{s}, c\bar{c}, gg, W^+W^-$, and hh . Limits use \mathcal{LS} J factors. The solid black line shows the combined best fit TS values. The colored, dashed lines are the TS values from each dSph.	71
313	Figure 6.10	HAWC TS values for best fit $\langle\sigma v\rangle$ versus m_χ for SM annihilation channels: $\chi\chi \rightarrow \nu_e\bar{\nu}_e, \nu_\mu\bar{\nu}_\mu, \nu_\tau\bar{\nu}_\tau, e\bar{e}, \mu\bar{\mu}, \tau\bar{\tau}, \gamma\gamma$ and ZZ . Limits use \mathcal{LS} J factors. The solid black line shows the combined best fit TS values. The colored, dashed lines are the TS values from each dSph.	72
317	Figure 6.11	Comparison of HAWC limits from this analysis to Glory Duck (Fig. 5.5) for 3 dSphs and 3 SM annihilation channels: $b\bar{b}, \tau\bar{\tau}$, and $e\bar{e}$. Each sector shows the 95% confidence limit from Glory Duck (blue line) and this analysis (orange line) in the top plot. The lower plot features the ratio in log scale of Glory Duck to this analysis in a red solid line. Horizontal dashed lines are for ratios of 1.0 (black) and $\sqrt{2}$ (blue). Ratios larger than 1.0 are for limits smaller, or stricter, than Glory Duck. Ratios larger than $\sqrt{2}$ indicates limits are stricter than a simple doubling of the Glory Duck data.	74

325	Figure 7.1	Neutrino spectra at production (left panels) and after oscillation at Earth 326 (right panels). Blue, orange, and green lines are the ν_e , ν_μ , and ν_τ spectra 327 respectively. Top panels show the spectra in $\frac{dN}{dE}$. Lower panels plot the flavor 328 ratio to $\nu_e + \nu_\mu + \nu_\tau$. SM annihilation channels $b\bar{b}$, $\tau\bar{\tau}$, and $\nu_\mu\bar{\nu}_\mu$ are shown 329 for $M_\chi = 1$ PeV, TeV, and EeV.	79
330	Figure 7.2	Signal recovery for 100 TeV DM annihilation into $\nu_\mu\bar{\nu}_\mu$ for a source at Dec 331 = 16.06° . n_{inj} is the number of injected signal events in simulation. n_s is 332 the number of reconstructed signal events from the simulation. Although 333 the uncertainties are small and tight, the reconstructed n_s are systematically 334 underestimated.	80
335	Figure 7.3	Top left panel shows the two kernels overlayed the original spectrum from 336 Charon. delta I is the difference in the integral of the peaks with respect to the 337 original spectrum. The vertical red line indicated where the original neutrino 338 line is maximized. Lower right shows the signal recovers of the DM model 339 using the Gaussian kernel with parameters enumerated above.	81
340	Figure A.1	Sister figure to Figure 5.3. Sources in the first row from left to right: Bootes 341 I, Canes Venatici I, II. In second row: Draco, Hercules, Leo I. In the first row: 342 Leo II, Leo IV, Sextans. In the final row: Ursa Major I, Ursa Major II.	85
343	Figure B.1	Sister figure to Figure 6.2 for remaining SM primary annihilation channels 344 studied for this thesis. These did not require any post generation smoothing 345 and so are directly pulled from [64] with a binning scheme most helpful for a 346 HAWC analysis.	86
347	Figure B.2	TODO: fill this out	96
348	Figure B.3	TODO: fill this out	97
349	Figure B.4	TODO: fill this out	98

LIST OF ABBREVIATIONS

- 351 **MSU** Michigan State University
352 **LANL** Los Alamos National Laboratory
353 **DM** Dark Matter
354 **SM** Standard Model
355 **HAWC** High Altitude Water Cherenkov Observatory
356 **dSph** Dwarf Spheroidal Galaxy

CHAPTER 1

INTRODUCTION

358 Is the text not rendering right? Ah ok it knows im basically drafting the doc still

CHAPTER 2

359

DARK MATTER IN THE COSMOS

360 **2.1 Introduction**

361 The dark matter problem can be summarized in part by the following thought experiment.

362 Let us say you are the teacher for an elementary school classroom. You take them on a field
363 trip to your local science museum and among the exhibits is one for mass and weight. The exhibit
364 has a gigantic scale, and you come up with a fun problem for your class.

365 You ask your class, "What is the total weight of the classroom? Give your best estimation to
366 me in 30 minutes, and then we'll check your guess on the scale. If your guess is within 10% of the
367 right answer, we will stop for ice cream on the way back."

368 The students are ecstatic to hear this, and they get to work. The solution is some variation of
369 the following strategy. The students should give each other their weight or best guess if they do
370 not know. Then, all they must do is add each student's weight and get a grand total for the class.

371 The measurement on the giant scale should show the true weight of the class. When comparing
372 the measured weight to your estimation, multiply the measurement by 1.0 ± 0.1 to get the $\pm 10\%$
373 tolerances for your estimation.

374 Two of your students, Sandra and Mario, return to you with a solution.

375 They say, "We weren't sure of everyone's weight. We used 65 lbs. for the people we didn't
376 know and added everyone who does know. There are 30 of us, and we got 2,000 lbs.! That's a ton!"

377 You estimated 1,900 lbs. assuming the average weight of a student in your class was 60 lbs.
378 So, you are pleased with Sandra's and Mario's answer. You instruct your students to all gather on
379 the giant scale and read off the weight together. To all your surprise, the scale reads *10,000 lbs.*!
380 10,000 is significantly more than a 10% error from 2,000. In fact, it is approximately 5 times more
381 massive than either your or your students' estimates. You think to yourself and conclude there
382 must be something wrong with the scale. You ask an employee to check the scale and verify it is
383 well calibrated. They confirm that the scale is in working order. You weigh a couple of students
384 individually to assess that the scale is well calibrated. Sandra weighs 59 lbs., and Mario weighs

385 62 lbs., typical weights for their age. You then weigh each student individually and see that their
386 weights individually do not deviate greatly from 60 lbs. So, where does all the extra weight come
387 from?

388 This thought experiment serves as an analogy to the Dark Matter problem. The important
389 substitution to make however is to replace the students with stars and the classroom with a galaxy,
390 say the Milky Way. Individually the mass of stars is well measured and defined with the Sun as our
391 nearest test case. However, when we set out to measure the mass of a collection of stars as large as
392 galaxies, our well-motivated estimation is wildly incorrect. There simply is no way to account for
393 this discrepancy except without some unseen, or dark, contribution to mass and matter in galaxies.
394 I set out in my thesis to narrow the possibilities of what this Dark Matter could be.

395 This chapter is organized like the following... **TODO: Text should look like ... Chapter x has**
396 **blah blah blah.**

397 2.2 Dark Matter Basics

398 Presently, a more compelling theory of cosmology that includes Dark Matter (DM) in order
399 to explain a variety of observations is Λ Cold Dark Matter, or Λ CDM. I present the evidence
400 supporting Λ CDM in Section 2.3 yet discuss the conclusions of the Λ CDM model here. According
401 to Λ CDM fit to observations on the Cosmic Microwave Background (CMB), DM is 26.8% of the
402 universe's current energy budget. Baryonic matter, stuff like atoms, gas, and stars, contributes to
403 4.9% of the universe's current energy budget [1, 2, 3].

404 DM is dark; it does not interact readily with light at any wavelength. DM also does not interact
405 noticeably with the other standard model forces (Strong and Weak) at a rate that is readily observed
406 [3]. DM is cold, which is to say that the average velocity of DM is below relativistic speeds [1].
407 'Hot' DM would not likely manifest the dense structures we observe like galaxies, and instead
408 would produce much more diffuse galaxies than what is observed [3, 1]. DM is old; it played a
409 critical role in the formation of the universe and the structures within it [1, 2].

410 Observations of DM have so far been only gravitational. The parameter space available to what
411 DM could be therefore is extremely broad. The broad DM parameter space is iteratively tested in

412 DM searches by supposing a hypothesis that has not yet been ruled out and performing observations
413 to test them. When the observations yield a null result, the parameter space is constrained further.
414 I present some approaches for DM searches in Section 2.4.

415 **2.3 Evidence for Dark Matter**

416 Dark Matter (DM) has been a looming problem in physics for almost 100 years. Anomalies
417 have been observed by astrophysicists in galactic dynamics as early as 1933 when Fritz Zwicky
418 noticed unusually large velocity dispersion in the Coma cluster. Zwicky's measurement was the
419 first recorded to use the Virial theorem to measure the mass fraction of visible and invisible matter
420 in celestial bodies [4]. From Zwicky in [5], "*If this would be confirmed, we would get the surprising*
421 *result that dark matter is present in much greater amount than luminous matter.*" Zwicky's and
422 others' observation did not instigate a crisis in astrophysics because the measurements did not
423 entirely conflict with their understanding of galaxies [4]. In 1978, Rubin, Ford, and Norbert
424 measured rotation curves for ten spiral galaxies [6]. Rubin et al.'s 1978 publication presented a
425 major challenge to the conventional understanding of galaxies that could no longer be dismissed by
426 measurement uncertainties. Evidence has been mounting ever since for this exotic form of matter.
427 The following subsections provide three compelling pieces of evidence in support of the existence
428 of DM.

429 **2.3.1 First Clues: Stellar Velocities**

430 Zwicky, and later Rubin, measured the stellar velocities of various galaxies to estimate their
431 virial mass. The Virial Theorem upon which these observations are interpreted is written as

$$2T + V = 0. \quad (2.1)$$

432 Where T is the kinetic energy and V is the potential energy in a self-gravitating system. The
433 classical Newton's law of gravity from stars and gas was used for gravitational potential modeled in
434 the observed galaxies:

$$V = -\frac{1}{2} \sum_i \sum_{j \neq i} \frac{m_i m_j}{r_{ij}}. \quad (2.2)$$

435 Zwicky et al. measured just the velocities of stars apparent in optical wavelengths [5]. Rubin et al.
 436 added by measuring the velocity of the hydrogen gas via the 21 cm emission line of Hydrogen [6].
 437 The velocities of the stars and gas are used to infer the total mass of galaxies and galaxy clusters
 438 via Equation (2.1). An inferred mass is obtained from the luminosity of the selected sources. The
 439 two inferences are compared to each other as a luminosity to mass ratio which typically yielded [1]

$$\frac{M}{L} \sim 400 \frac{M_{\odot}}{L_{\odot}} \quad (2.3)$$

440 M_{\odot} and L_{\odot} referring to stellar mass and stellar luminosity, respectively. These ratios clearly indicate
 441 a discrepancy in apparent light and mass from stars and gas and their velocities.

442 Rubin et al. [6] demonstrated that the discrepancy was unlikely to be an underestimation of
 443 the mass of the stars and gas. The inferred "dark" mass was up to 5 times more than the luminous
 444 mass. This dark mass also needed to extend well beyond the extent of the luminous matter.

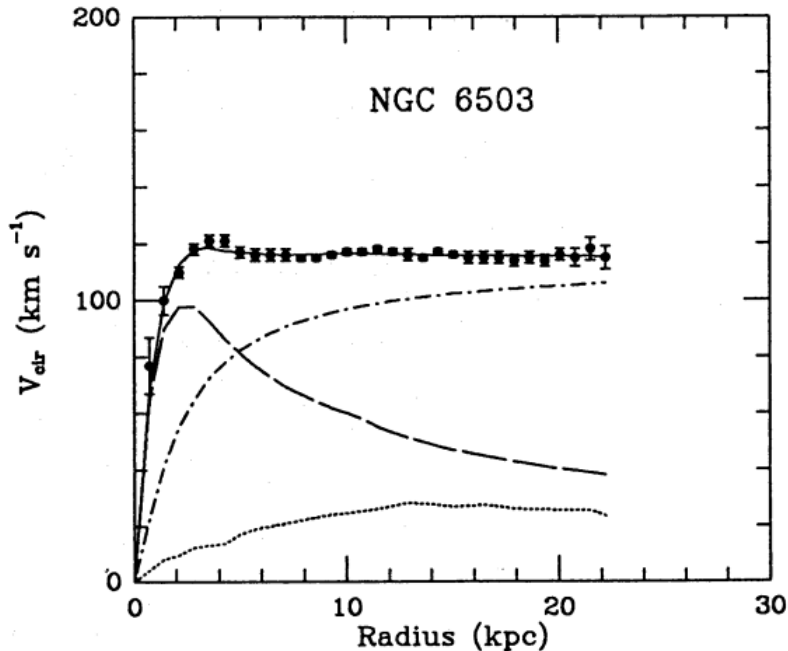


Figure 2.1 Rotation curve fit to NGC 6503 from [7]. Dashed line is the contribution from visible matter. Dotted curves are from gas. Dash-dot curves are from dark matter (DM). Solid line is the composite contribution from all matter and DM sources. Data are indicated with bold dots with error bars. Data agree strongly with a matter + DM composite prediction.

445 Figure 2.1 features one of many rotation curves plotted from the stellar velocities within galaxies.

446 The measured rotation curves mostly feature a flattening of velocities at higher radius which is not
447 expected if the gravity was only coming from gas and luminous matter. The extension of the
448 flat velocity region also indicates that the DM is distributed far from the center of the galaxy.
449 Modern velocity measurements include significantly larger objects, galactic clusters, and smaller
450 objects, dwarf galaxies. Yet, measurements along this regime are leveraging the Virial theorem
451 with Newtonian potential energies. We know Newtonian gravity is not a comprehensive description
452 of gravity. New observational techniques have been developed since 1978, and those are discussed
453 in the following sections.

454 **2.3.2 Evidence for Dark Matter: Gravitational Lensing**

455 Modern evidence for dark matter comes from new avenues beyond stellar velocities. Grav-
456 itational lensing from DM is a new channel from general relativity. General relativity predicts
457 aberrations in light caused by massive objects. In recent decades we have been able to measure the
458 lensing effects from compact objects and DM halos. Figure 2.2 shows how different massive ob-
459 jects change the final image of a faraway galaxy resulting from gravitational lensing. Gravitational
460 lensing developed our understanding of dark matter in two important ways.

461 Gravitational lensing provides additional compelling evidence for DM. The observation of two
462 merging galactic clusters in 2006, shown in Figure 2.3, provided a compelling argument for DM
463 outside the Standard Model. These clusters merged recently in astrophysical time scales. Galaxies
464 and star cluster have mostly passed by each other as the likelihood of their collision is low. Therefore,
465 these massive objects will mostly track the highest mass, dark and/or baryonic, density. Yet, the
466 intergalactic gas is responsible for the majority of the baryonic mass in the systems [4]. These gas
467 bodies will not phase through and will heat up as they collide together. The hot gas is located via
468 x-ray emission from the cluster. Two observations of the clusters were performed independently of
469 each other.

470 The first was the lensing of light around the galaxies due to their gravitational influences.
471 When celestial bodies are large enough, the gravity they exert bends space and time itself. The
472 warped space-time lenses light and will deflect in an analogous way to how glass lenses will bend

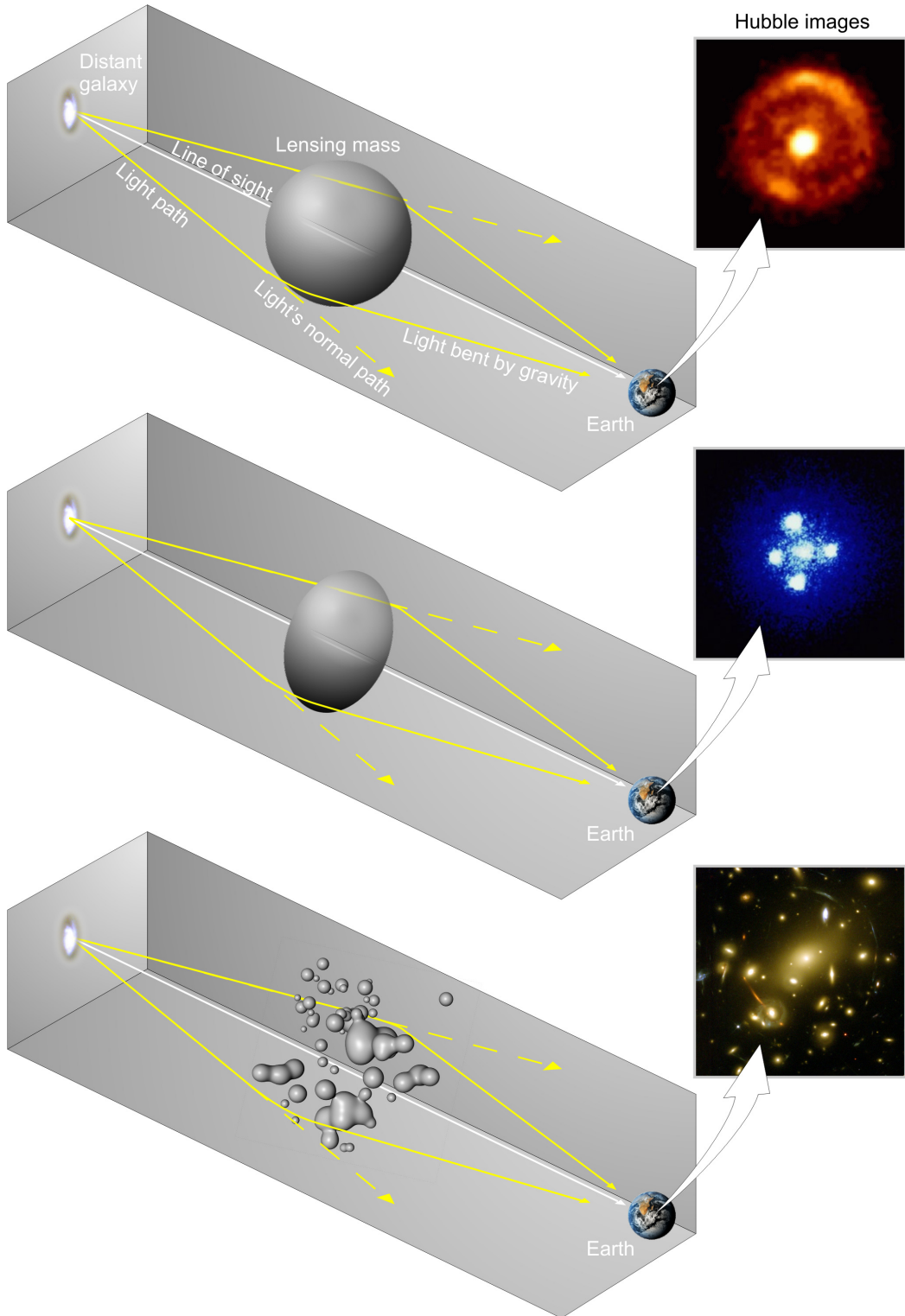


Figure 2.2 Light from distant galaxy is bent in unique ways depending on the distribution of mass between the galaxy and Earth. Yellow dashed lines indicate where the light would have gone if the matter were not present [8].

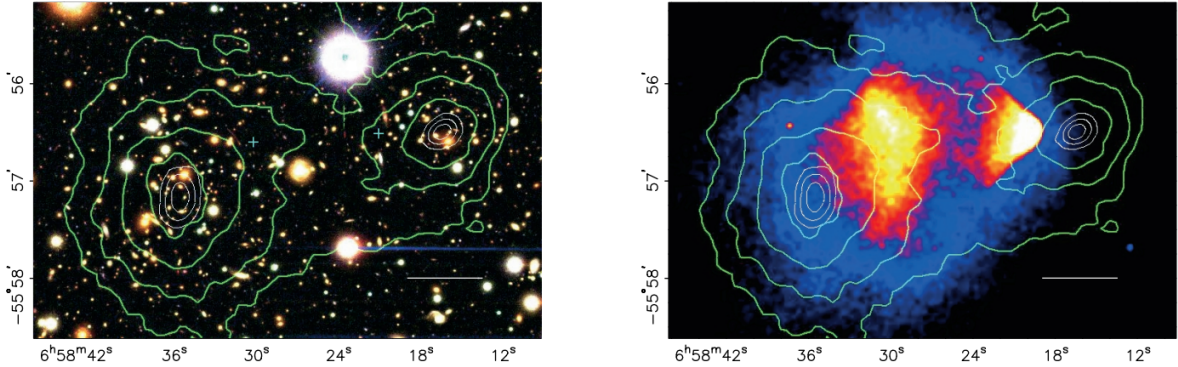


Figure 2.3 (left) Optical image of galactic cluster 1E0657-558. (right) X-ray image of the cluster with redder meaning hotter and higher baryon density. (both) Green contours are reconstruction of gravity contours from weak lensing. White rings are the best fit mass maxima at 68.3%, 95.5%, and 99.7% confidence. The matter maxima of the clusters are clearly separated from x-ray maxima. [9]

473 light, see Figure 2.2. With a sufficient understanding of light sources behind a massive object, we
 474 can reconstruct the contours of the gravitational lenses. The gradient of the contours shown in
 475 Figure 2.3 then indicates how dense the matter is and where it is.

476 The x-ray emission can then be observed from the clusters. Since these galaxies are mostly gas
 477 and are merging, then the gas should be getting hotter. If they are merging, the x-ray emissions
 478 should be the strongest where the gas is mostly moving through each other. Hence, X-ray emission
 479 maps out where the gas is in the merging galaxy cluster.

480 The lensing and x-ray observations were done on the Bullet cluster featured on Figure 2.3.
 481 The x-ray emissions do not align with the gravitational contours from lensing. The incongruence
 482 in mass density and baryon density suggests that there is a lot of matter somewhere that does
 483 not interact with light. Moreover, this dark matter cannot be baryonic [9]. The Bullet Cluster
 484 measurement did not really tell us what DM is exactly, but it did give the clue that DM also does
 485 not interact with itself very strongly. If DM did interact strongly with itself, then it would have been
 486 more aligned with the x-ray emission [9]. There have been follow-up studies of galaxy clusters with
 487 similar results. The Bullet Cluster and others like it provide a persuasive case against something
 488 possibly amiss in our gravitational theories.

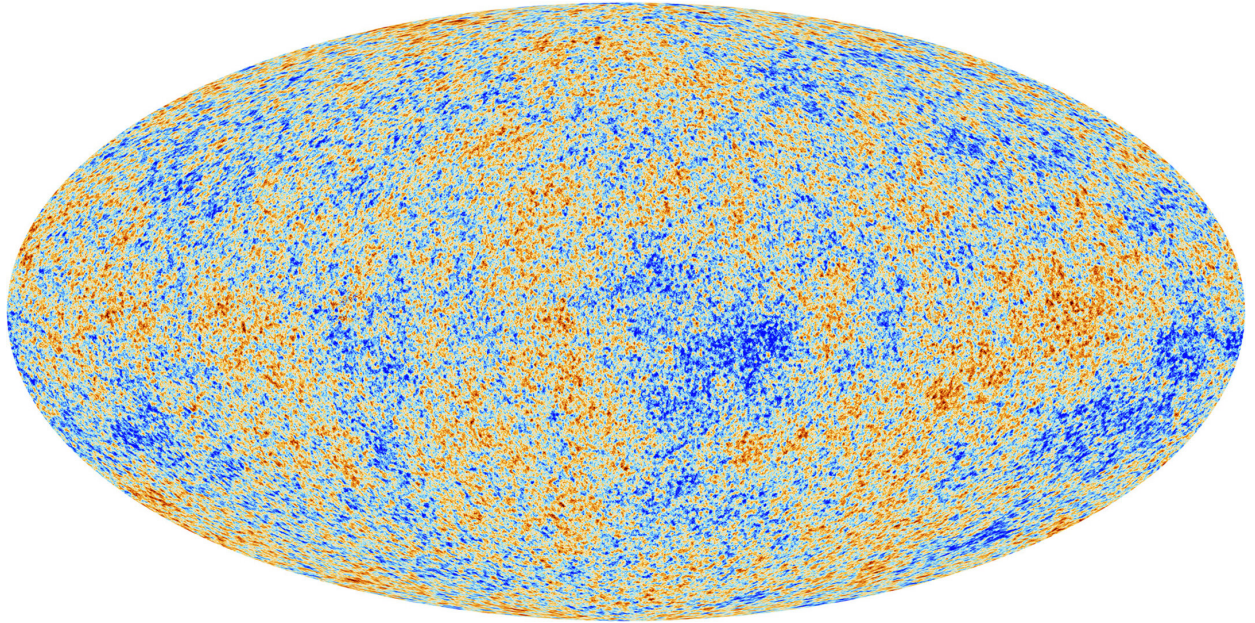


Figure 2.4 Plank CMB sky. Sky map features small variations in temperature in primordial light. These anisotropies are used to make inferences about the universe’s energy budget and developmental history. [10]

489 **2.3.3 Evidence for Dark Matter: Cosmic Microwave Background**

490 The Cosmic Microwave Background (CMB) is the primordial light from the early universe
491 when Hydrogen atoms formed from the free electron and proton soup in the early universe. The
492 CMB is the earliest light we can observe; released when the universe was about 380,000 years old.
493 Then we look at how the simulated universes look like compared to what we see. Figure 2.4 is the
494 most recent CMB image from the Plank satellite after subtracting the average value and masking the
495 galactic plane [10]. Redder regions indicate a slightly hotter region in the CMB, and blue indicates
496 colder. The intensity variations are on the order of 1 in 1000 with respect to the average value.

497 The Cosmic Microwave Background shows that the universe had DM in it from an incredibly
498 early stage. To measure the DM, Dark Energy, and matter fractions of the universe from the CMB,
499 the image is analyzed into a power spectrum, which shows the amplitude of the fluctuations as
500 a function of spherical multipole moments. Λ CDM provides the best fit to the power spectra of
501 the CMB as shown in Figure 2.5. The CMB power spectrum is quite sensitive to the fraction
502 of each energy contribution in the early universe. Low l modes are dominated by variations
503 in gravitational potential. Intermediate l emerge from oscillations in photon-baryon fluid from

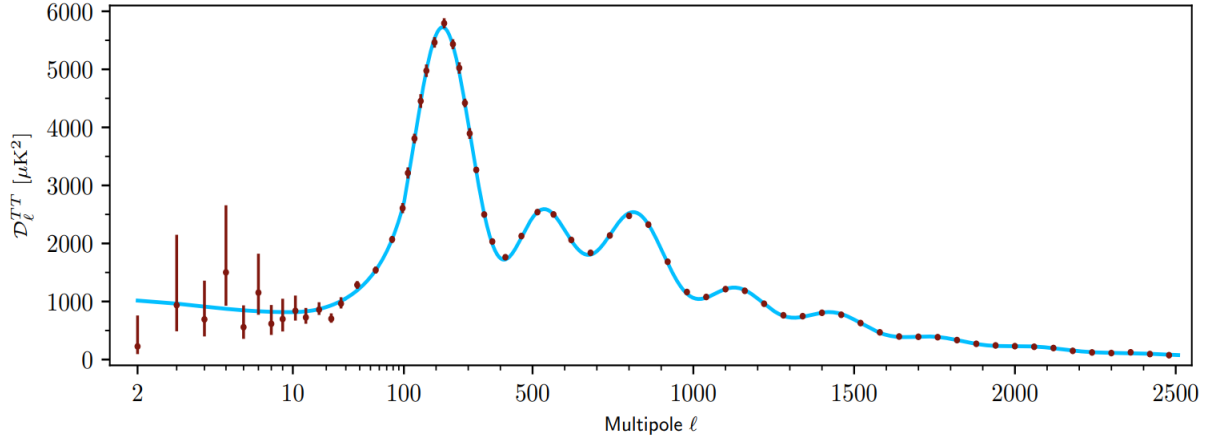


Figure 2.5 Observed Cosmic Microwave Background power spectrum as a function of multipole moment from Plank [10]. Blue line is best fit model from Λ CDM. Red points and lines are data and error, respectively.

504 competing baryon pressures and gravity. High l is a damped region from the diffusion of photons
 505 during electron-proton recombination. [1]

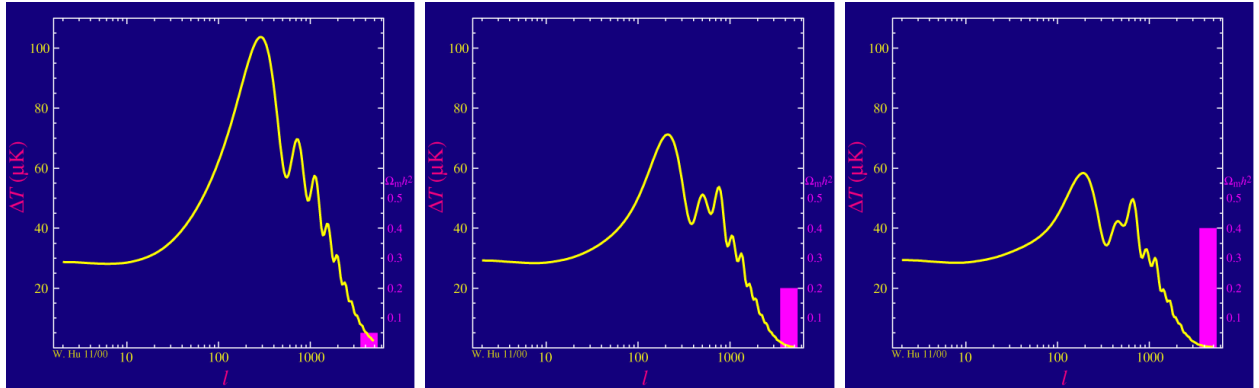


Figure 2.6 Predicted power spectra of CMB for different $\Omega_m h^2$ values for fixed baryon density from [11]. (left) Low $\Omega_m h^2$ increases the prominence of first and second peaks. (middle) $\Omega_m h^2$ is most similar to the observed power spectrum. The second and third peaks are similar in height. (right) $\Omega_m h^2$ is large which suppresses the first peak and raises the prominence of the third peak.

506 The harmonics would look quite different for a universe with less DM. Figure 2.6 demonstrates
 507 the effect $\Omega_m h^2$ has on the expected power spectrum for fixed baryon matter density. [11] Sweeping
 508 $\Omega_m h^2$ in this way clearly shows the effect dark matter has on the CMB power spectrum. The
 509 observations fit well with the Λ CDM model, and the derived fractions are as follows. The matter
 510 fraction: $\Omega_m = 0.3153$; and the baryon fraction: $\Omega_b = 0.04936$ [10]. Plank's observations also
 511 provide a measure of the Hubble constant, H_0 . H_0 especially has seen a growing tension in the

512 past decade that continues to deepened with observations from instruments like the James Webb
513 Telescope [12, 13]. As Hubble tensions deepen, we may find that perhaps Λ **CDM**, despite its
514 successes, is missing some critical physics.

515 Overall, the Newtonian motion of stars in galaxies, weak lensing from galactic clusters, and
516 power spectra from primordial light form a compelling body of research in favor of dark matter.
517 It takes another leap of theory and experimentation to make observations of DM that are non-
518 gravitational in nature. In Section 2.3, the evidence for DM implies strongly that the DM is matter
519 and not a lost parameter in the gravitational fields between massive objects. Finally, if we take one
520 axiom: that this matter has quantum behavior, such as being described by some Bohr wavelength
521 and abiding by some fermion or boson statistics; then we arrive at particle dark matter. One particle
522 DM hypothesis is the Weakly Interacting Massive Particle (WIMP). This DM candidate theory is
523 discussed further in the next section and is the focus of this thesis.

524 **2.4 Searching for Dark Matter: Particle DM**

525 Section 2.4 shows the Standard Model of particle physics and is currently the most accurate
526 model for the dynamics of fundamental particles like electrons and photons. The current status
527 of the SM does not have a viable DM candidate. When looking at the standard model, we can
528 immediately exclude any charged particle because charged particles interact strongly with light.
529 Specifically, this will rule out the following charged, fundamental particles: $e, \mu, \tau, W, u, d, s, c, t, b$
530 and their corresponding antiparticles. Recalling from Section 2.2 that DM must be long-lived and
531 stable over the age of the universe which excludes all SM particles with decay half-lives at or shorter
532 than the age of the universe. The lifetime constraint additionally eliminates the Z and H bosons.
533 Finally, the candidate DM needs to be somewhat massive. Recall from Section 2.2 that DM is cold
534 or not relativistic through the universe. This eliminates the remaining SM particles: $\nu_{e,\mu,\tau}, g, \gamma$ as
535 DM candidates. Because there are no DM candidates within the SM, the DM problem strongly
536 hints to physics beyond the SM (BSM).

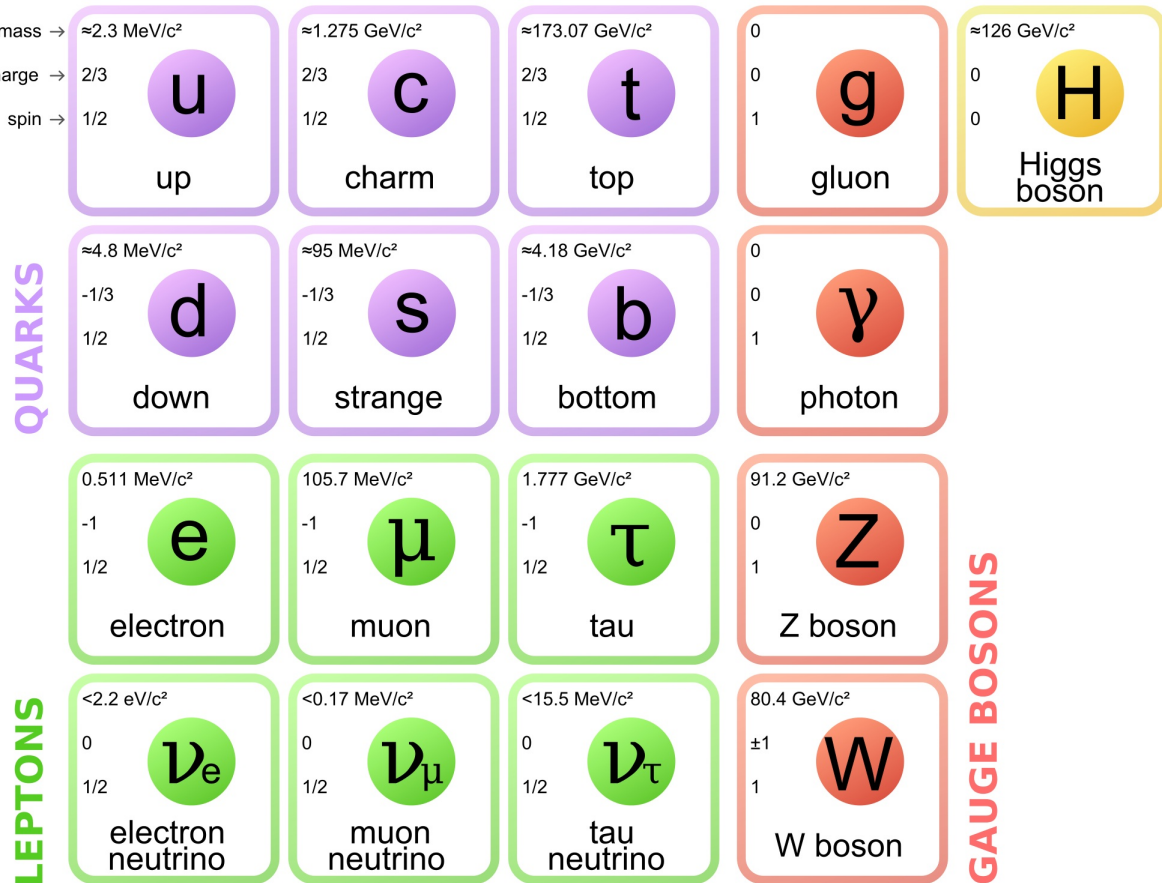


Figure 2.7 The Standard Model (SM) of particle physics. Figure taken from <http://www.quantumdiaries.org/2014/03/14/the-standard-model-a-beautiful-but-flawed-theory/>

537 2.4.1 Shake it, Break it, Make it

538 When considering DM that couples in some way with the SM, the interactions are roughly
 539 demonstrated by interaction demonstrated in Figure 2.8. The figure is a simplified Feynman
 540 diagram where the arrow of time represents the interaction modes of: **Shake it, Break it, Make it.**

541 **Shake it** refers to the direct detection of dark matter. Direct detection interactions start with
 542 a free DM particle and an SM particle. The DM and SM interact via elastic or inelastic collision
 543 and recoil away from each other. The DM remains in the dark sector and imparts some momentum
 544 onto the SM particle. The hope is that the momentum imparted onto the SM particle is sufficiently
 545 high enough to pick up with extremely sensitive instruments. Because we cannot create the DM in
 546 the lab, a direct detection experiment must wait until DM is incident on the detector. Most direct
 547 detection experiments are therefore placed in low-background environments with inert detection

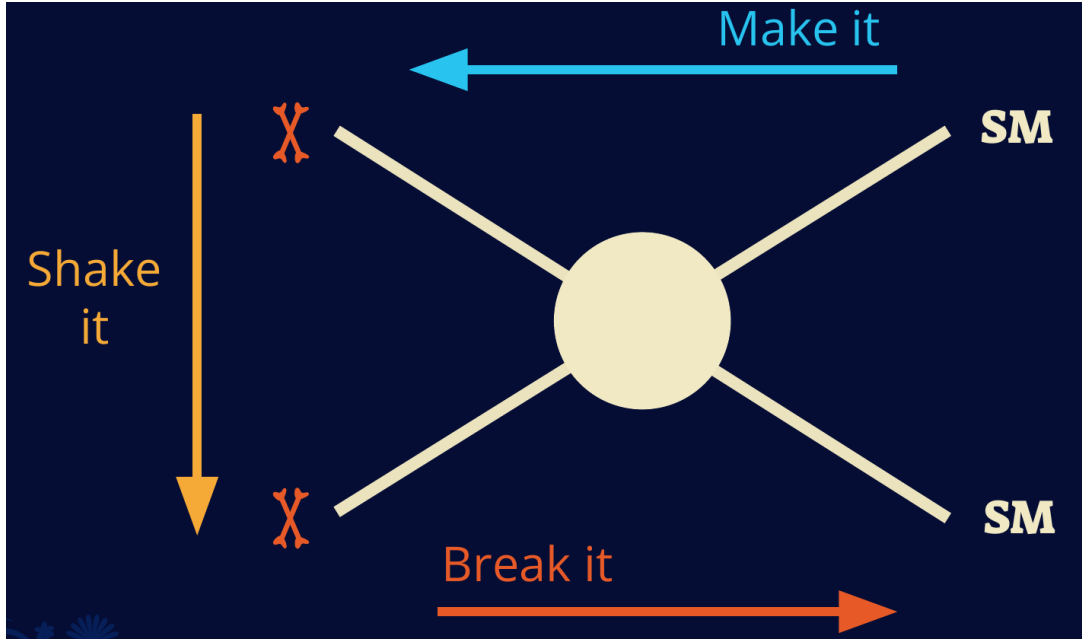


Figure 2.8 Simplified Feynman diagram demonstrating different ways DM can interact with SM particles. The 'X's refer to the DM particles whereas the SM refer to fundamental particles in the SM. The large circle in the center indicates the vertex of interaction and is purposely left vague. The colored arrows refer to different directions of time as well as their respective labels. The arrows indicate the initial and final state of the DM -SM interaction in time.

548 media like the noble gas Xenon. [14]

549 **Make it** refers to the production of DM from SM initial states. The experiment starts with
 550 particles in the SM. These SM particles are accelerated to incredibly high energies and then collide
 551 with each other. In the confluence of energy, DM hopefully emerges as a byproduct of the SM
 552 annihilation. Often it is the collider experiments that are energetic enough to hypothetically produce
 553 DM. These experiments include the world-wide collaborations ATLAS and CMS at CERN where
 554 proton collide together at extreme energies. The DM searches, however, are complex. DM likely
 555 does not interact with the detectors and lives long enough to escape the detection apparatus of
 556 CERN's colliders. This means any DM production experiment searches for an excess of events
 557 with missing momentum or energy in the events. An example event with missing transverse
 558 momentum is shown in Figure 2.9. The missing momentum with no particle tracks implies a
 559 neutral particle carried the energy out of the detector. However, there are other neutral particles
 560 in the SM, like neutrons or neutrinos, so any analysis has to account for SM signatures of missing

561 momentum. [15]

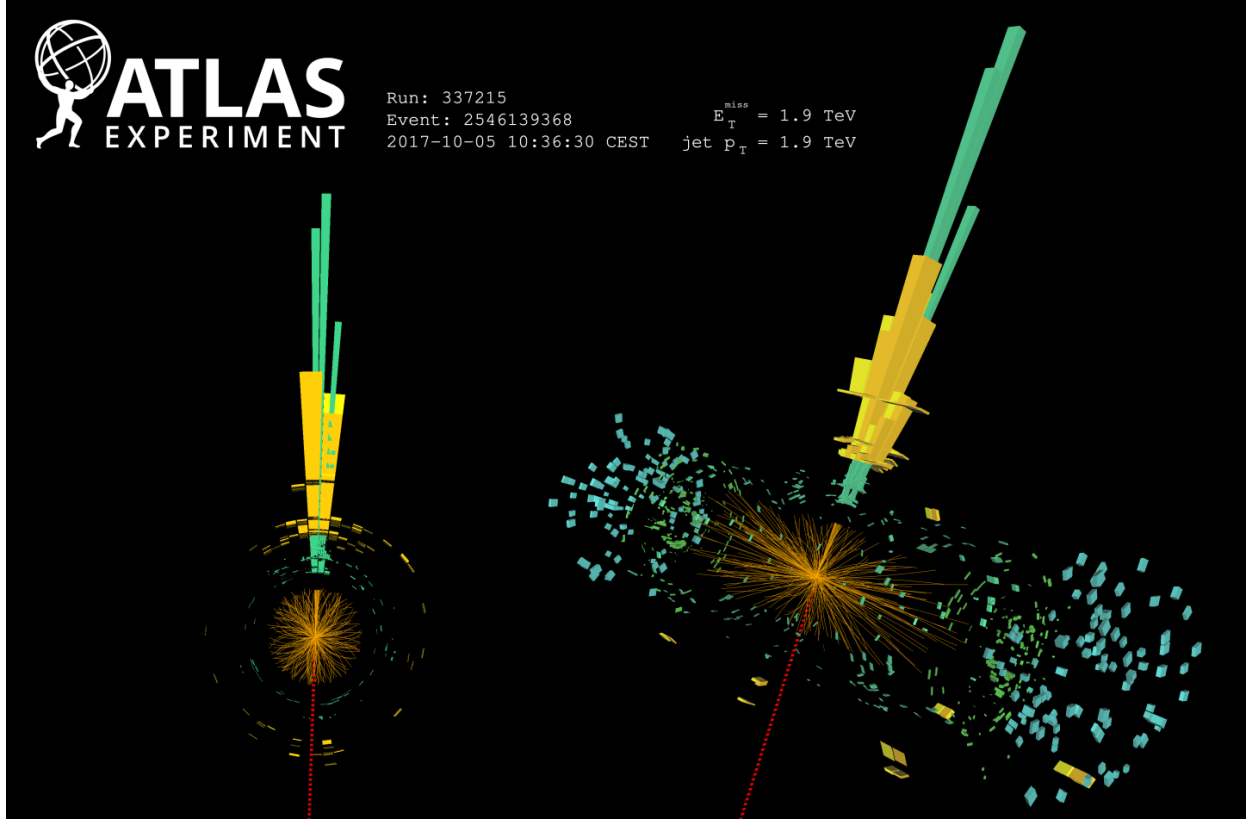


Figure 2.9 A single jet event in ATLAS detector from 2017 [16]. Jet momentum was observed to be 1.9 TeV. Missing transverse momentum was observed to be 1.9 TeV compared to the initial transverse momentum of the event was 0. Implied MET is traced by a red dashed line in event display.

562 2.4.2 Break it: Standard Model Signatures of Dark Matter through Indirect Searches

563 **Break it** refers to the creation of SM particles from the dark sector, and it is the primary focus
564 of this thesis. The interaction begins with DM or in the dark sector. The hypothesis is that this
565 DM will either annihilate with itself or decay and produce an SM byproduct. This method is
566 often referred to as the Indirect Detection of DM because we have no lab to directly control or
567 manipulate the DM. Therefore, most indirect DM searches are performed using observations of
568 known DM densities among the astrophysical sources. The strength is that we have the whole of the
569 universe and its 13.6-billion-year lifespan to use as a detector and particle accelerator. Additionally,
570 locations of dark matter are well cataloged since it was astrophysical observations that presented

571 the problem of DM in the first place.

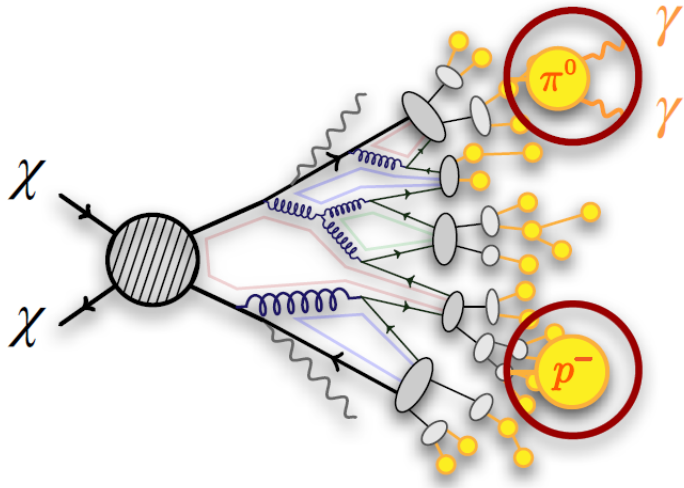


Figure 2.10 More detailed pseudo-Feynman diagram of particle cascade from dark matter annihilation into 2 quarks. The quarks hadronize and down to stable particles like γ or the anti-proton (p^-). Diagram pulled from ICRC 2021 presentation on DM annihilation search [17].

572 However, anything can happen in the universe. There are many difficult to deconvolve back-
573 grounds when searching for DM. One prominent example is the galactic center. We know the
574 galactic center has a large DM content because of stellar kinematics in our Milky Way and DM halo
575 simulations. Yet, any signal from the galactic center is challenging to parse apart from the extreme
576 environment of our supermassive black hole, unresolved sources, and diffuse emission from the
577 interstellar medium [18]. Despite the challenges, any DM model that yields evidence in the other
578 two observation methods, **Shake it or Make it** must be corroborated with indirect observations of
579 the known DM sources. Without corroborating evidence, DM observation in the lab is hard-pressed
580 to demonstrate that it is the model contributing to the DM seen at the universal scale.

581 In the case of WIMP DM, signals are described in terms of primary SM particles produced
582 from DM decay or annihilation. The SM initial state particles are then simulated down to stable
583 final states such as the γ , ν , p , or e which can traverse galactic lengths to reach Earth.

584 Figure 2.10 shows the quagmire of SM particles that emerges from SM initial states that are not
585 stable [17]. There are many SM particles with varying energies that can be produced in such an

586 interaction. For any arbitrary DM source and stable SM particle, the SM flux from DM annihilating
 587 to a neutral particle in the SM, ϕ , from a region in the sky is described by the following.

$$\frac{d\Phi_\phi}{dE_\phi} = \frac{\langle\sigma v\rangle}{8\pi m_\chi^2} \frac{dN_\phi}{dE_\phi} \times \int_{\text{source}} d\Omega \int_{l.o.s} \rho_\chi^2 dl(r, \theta') \quad (2.4)$$

588 In Equation (7.1), $\langle\sigma v\rangle$ is the velocity-weighted annihilation cross-section of DM to the SM. m_χ
 589 refers to the mass of DM, noted with Greek letter χ . $\frac{dN_\phi}{dE_\phi}$ is the N particle flux weighted by the
 590 particle energy. An example is provided in Figure 2.11 for the γ final state. The integrated terms
 591 are performed over the solid angle, $d\Omega$, and line of sight, l.o.s. ρ is the density of DM for a
 592 location (r, θ') in the sky. The terms left of the '×' are often referred to as the particle physics
 593 component. The terms on the right are referred to as the astrophysical component. For decaying
 594 DM, the equation changes to...

$$\frac{d\Phi_\phi}{dE_\phi} = \frac{1}{4\pi\tau m_\chi} \frac{dN_\phi}{dE_\phi} \times \int_{\text{source}} d\Omega \int_{l.o.s} \rho_\chi dl(r, \theta') \quad (2.5)$$

595 In Equation (6.1), τ is the decay lifetime of the DM. Just as in Equation (7.1), the left and right
 596 terms are the particle physics and the astrophysical components respectively. The integrated
 597 astrophysical component of Equation (7.1) is often called the J-Factor. Whereas the integrated
 598 astrophysical component of Equation (6.1) is often called the D-Factor.

599 Exact DM $\text{DM} \rightarrow \text{SM SM}$ branching ratios are not known, so it is usually assumed to go 100%
 600 into an SM particle/anti-particle. Additionally, when a DM annihilation or decay produces one of
 601 the neutral, long-lived SM particles (ν or γ), the particle is traced back to a DM source. For DM
 602 above GeV energies, there are very few SM processes that can produce particles with such a high
 603 energy. Seeing such a signal would almost certainly be an indication of the presence of dark matter.
 604 Fortunately, the universe provides us with the largest volume and lifetime ever for a particle physics
 605 experiment.

606 2.5 Sources for Indirect Dark Matter Searches

607 The first detection of DM relied on optical observations. Since then, we have developed new
 608 techniques to find DM dense regions. As described in Section 2.3.1, many DM dense regions were
 609 through observing galactic rotation curves. Our Milky Way galaxy is among DM dense regions

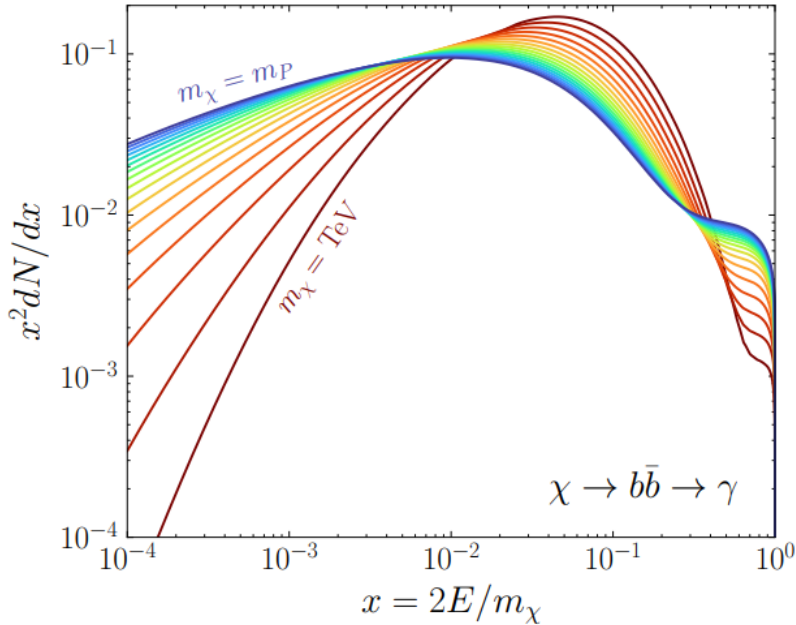


Figure 2.11 Dark Matter (DM) decay spectrum for $b\bar{b}$ initial state and γ final state. Redder spectra are for larger DM masses. Bluer spectra are light DM masses. x is a unitless factor defined as the ratio of the mass of DM, m_χ , and the final state particle energy E_γ . Figure from [19].

discovered, and it is the largest nearby DM dense region to look at. Additionally, the DM halo surrounding the Milky Way is clumpy [18]. There are regions in the DM halo of the Milky Way that have more DM than others that have captured gas over time. These sub-halos were dense enough collapse gas and form stars. These apparent sub galaxies are known as dwarf spheroidal galaxies and are the main sources studied in this thesis. Each source type comes with different trade-offs. Galactic Center studies will be very sensitive to the assumed distribution of DM. The central DM density can vary substantially as demonstrated in Figure 2.12. At distances close to the center of the galaxy, or small r , the differences in DM densities can be 3-4 orders of magnitude. Searches toward the galactic center will therefore be quite sensitive to the assumed DM distribution.

Searches toward Dwarf Spheroidal Galaxies (dSph's) suffer from uncertainties in the DM density less than the galactic center studies. This is mostly from their diminutive size being smaller than the angular resolution of most γ -ray observatories [18]. The DM content dSph's are typically determined with the Virial theorem, Equation (2.1), and are usually majority DM [18] in mass. DSph's tend to be ideal sources to look at for DM searches. Their environments are quiet with little

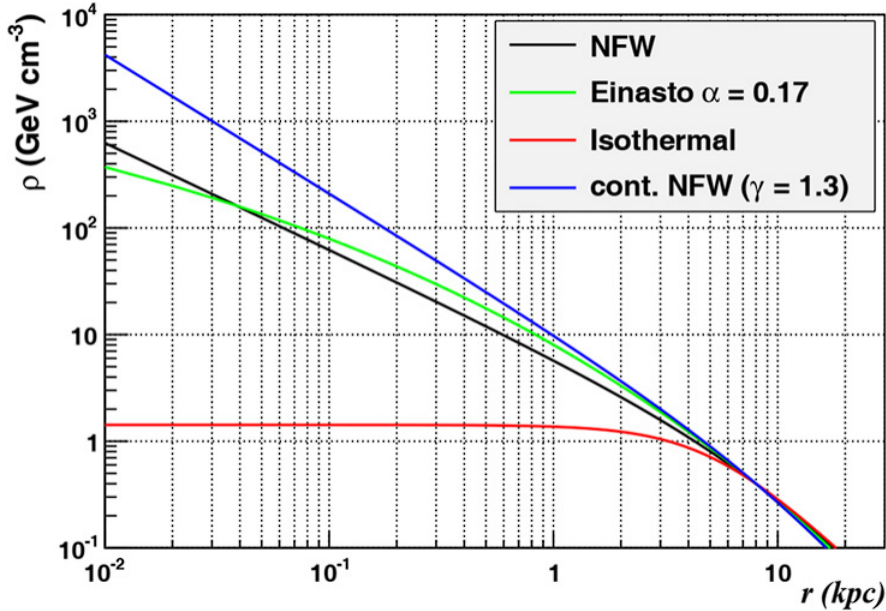


Figure 2.12 Different dark matter density profiles compared. Some models produce exceptionally large densities at small r [20].

624 astrophysical background. Unlike the galactic center, the most active components of dSph's are the
 625 stars within them versus a violent accretion disc around a black hole. All this together means that
 626 dSph's are among the best sources to look at for indirect DM searches. dSph's are the targets of
 627 focus for this thesis.

628 2.6 Multi-Messenger Dark Matter

629 Astrophysics entered a new phase in the past few decades that leverages our increasing sensitivity
 630 to SM channels and general relativity (GR). Up until the 21st century, astrophysical observations
 631 were performed with photons (γ) only. Astrophysics with this 'messenger' is fairly mature now.
 632 Novel observations of the universe have since only adjusted the sensitivity of the wavelength of
 633 light that is observed except at MeV energies. Gems like the CMB [10], and more have ultimately
 634 been observations of different wavelengths of light. Multi-messenger astrophysics proposes using
 635 other SM particles such the p^{+-} , or ν or gravitation waves predicted by general relativity.

636 The experiment LIGO had a revolutionary discovery in 2016 with the first detection of a binary
 637 black hole merger [21]. This opened the collective imagination to observing the universe through
 638 gravitational waves. There has also been a surge of interest in the neutrino (ν) sector. IceCube

639 demonstrated that we are sensitive to neutrinos in regions that correlate with significant photon
 640 emission like the galactic plane [22]. Neutrinos, like gravitational waves and light, travel mostly
 641 unimpeded from their source to our observatories. This makes pointing to the originating source
 642 of these messengers much easier than it is for cosmic rays which are deflected from their source by
 643 magnetic fields.

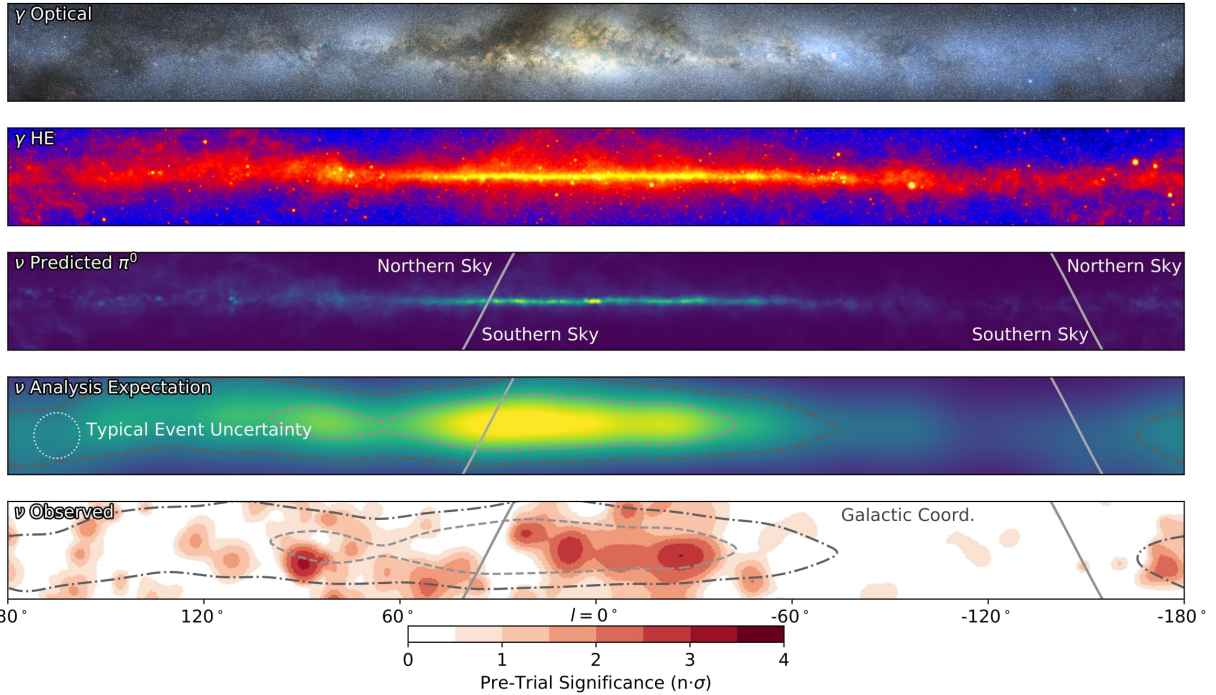


Figure 2.13 The Milky Way Galaxy in photons (γ) and neutrinos (ν) [22]. The Galactic center is at $l=0^\circ$ and is the brightest region in all panels. (top) An Optical color image of the Milky Way galaxy seen from Earth. Clouds of gas and dust obscure some light from stars. (2nd down) Integrated flux of γ -rays observed by the Fermi-LAT telescope [23]. (middle) Expected neutrino emission that corresponds with Fermi-LAT observations. (2nd up) Expected neutrino emission profile after considering detector systematics of IceCube. (bottom) Observed neutrino emission from region of the galactic plane. Substantial neutrino emission was detected.

644 The IceCube collaboration recently published a groundbreaking result of the Milky Way in
 645 neutrinos. The recent result from IceCube, shown in Figure 2.13, proves that we can make
 646 observations under different messenger regimes. The top two panels show the appearance of the
 647 galactic plane to different wavelengths of light. Some sources are more apparent in some panels,
 648 while others are not. This new channel is powerful because neutrinos are readily able to penetrate
 649 through gas and dust in the Milky Way. This new image also refines our understanding of how high

650 energy particles are produced. For example, the fit to IceCube data prefers neutrino production
 651 from the decay of π^0 [22].

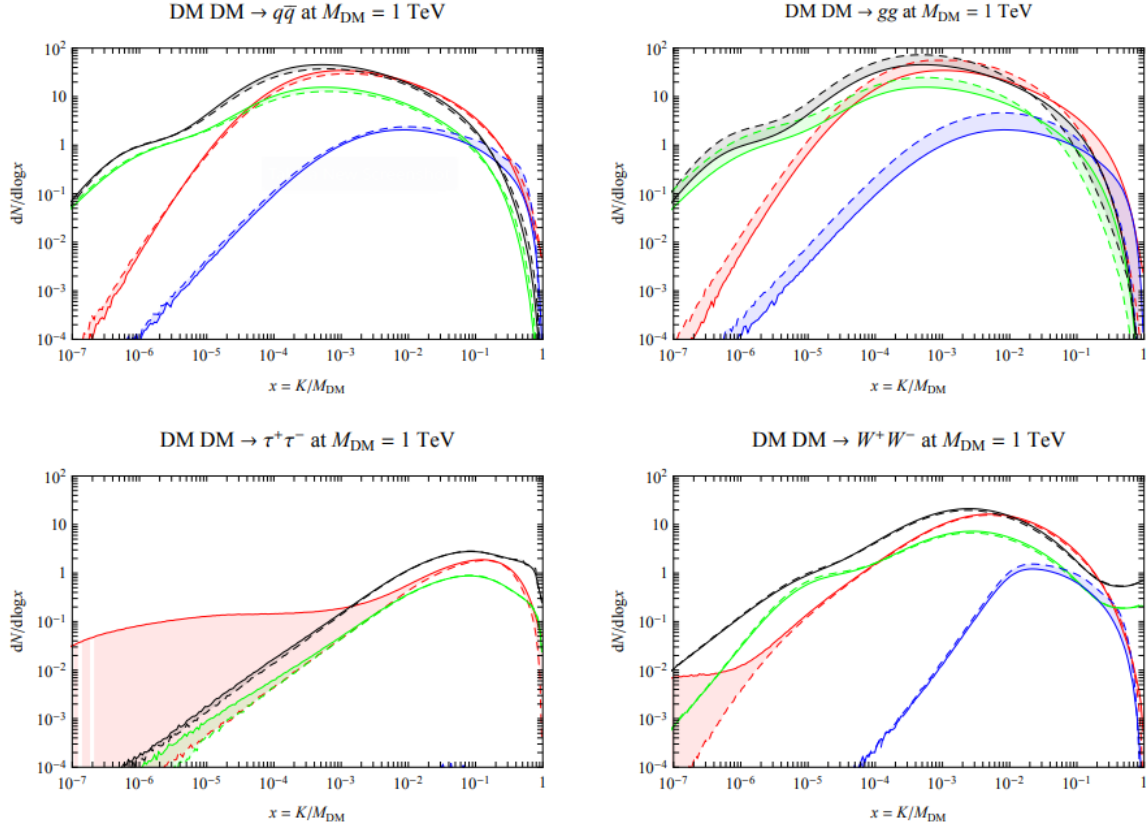


Figure 2.14 Dark Matter annihilation spectra for different final state particle and standard model annihilation channels [24]. Photons (red), e^\pm (green), \bar{p} (blue), ν (black).

652 Exposing our observations to more cosmic messengers greatly increases our sensitivity to
 653 rare processes. In the case of DM, Figure 2.14, there are many SM particles produced in DM
 654 annihilation. Among the final state fluxes are gammas and neutrinos. Charged particles are also
 655 produced however they would not likely make it to Earth since they will be deflected by magnetic
 656 fields between the source and Earth. This means observatories that can see the neutral messengers
 657 are especially good for DM searches and for combining data for a multi-messenger DM search.

CHAPTER 3

658 **HIGH ALTITUDE WATER CHERENKOV (HAWC) OBSERVATORY**

659 **3.1 The Detector**

660 **3.2 Events Reconstruction and Data Acquisition**

661 **3.2.1 G/H Discrimination**

662 **3.2.2 Angle**

663 **3.2.3 Energy**

664 **3.3 Remote Monitoring**

665 **3.3.1 ATHENA Database**

666 **3.3.2 HOMER**

667

CHAPTER 4

ICECUBE NEUTRINO OBSERVATORY

668 **4.1 The Detector**

669 **4.2 Events Reconstruction and Data Acquisition**

670 **4.2.1 Angle**

671 **4.2.2 Energy**

672 **4.3 Northern Test Site**

673 **4.3.1 PIgeon remote dark rate testing**

674 **4.3.2 Bulkhead Construction**

CHAPTER 5

675 **GLORY DUCK: MULTI-WAVELENGTH SEARCH FOR DARK MATTTER** 676 **ANNIHILATION TOWARDS DWARF SPHEROIDAL GALAXIES**

677 **5.1 Introduction**

678 The field of astrophysics now has several instruments and observatories sensitive to high
679 energy gamma-rays. The energy sensitivity for the modern gamma-ray program spans many orders
680 of magnitude. Figure 5.1 demonstrates these similar sensitivities across energies for the five
681 experiments: Fermi-LAT, HAWC, HESS, MAGIC, and VERITAS.

682 Each of the five experiments featured in Figure 5.1 have independently searched for DM
683 annihilation from dwarf spheroidal galaxies (dSph) and set limits. Intriguingly, there are regions of
684 substantial overlap in their energy sensitivities. This clearly motivates an analysis that combines data
685 from these five. Each experiment has unique gamma-ray detection methods and their weaknesses
686 and strengths can be leveraged with each other. The HAWC gamma-ray observatory is extensively
687 introduced in chapter 3, so it is not introduced here. A brief description of the remaining experiments
688 are in the following paragraphs.

689 The Large Area Telescope (LAT) is a pair conversion telescope mounted on the NASA Fermi
690 satellite in orbit \sim 550 km above the Earth [26]. LAT's field of view covers about 20% of the
691 whole sky, and it sweeps the whole sky approximately every 3 hours. LAT's gamma-ray energy
692 sensitivity ranges from 20 MeV up to 1 TeV. Previous DM searches towards dSphs using Fermi-LAT
693 are published in [27] and [28]

694 The High Energy Spectroscopic System (HESS), Major Atmospheric Gamma Imaging
695 Cherenkov (MAGIC), and Very Energetic Radiation Imaging Telescope Array System (VERI-
696 TAS) are arrays of Imaging Atmospheric Cherenkov Telescopes (IACT). These telescopes observe
697 the Cherenkov light emitted from gamma-ray showers in the Earth's atmosphere. The field of
698 view for these telescopes is no larger than 5° with energy sensitivities ranging from 30 GeV up
699 to 100 TeV [29, 30, 31]. IACTs are able to make precise observations in selected regions of the
700 sky, however can only be operated in ideal dark conditions. HESS's observations of the dwarves

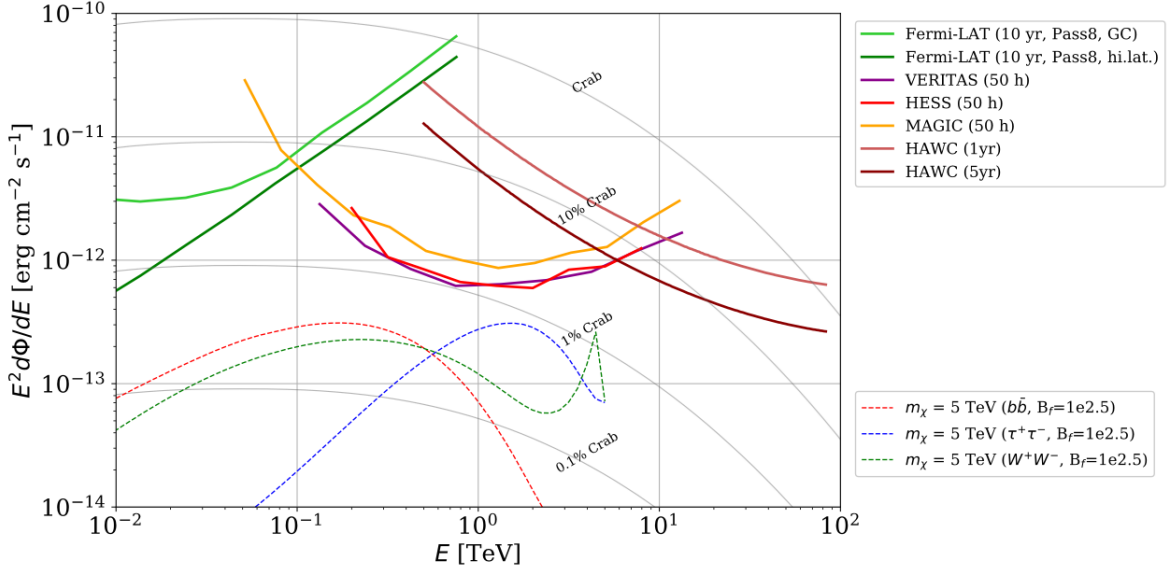


Figure 5.1 Sensitivities of five gamma-ray experiments compared to percentages of the Crab nebula’s emission and dark matter annihilation. Solid lines present estimated sensitivities to power law spectra [FACT CHECK THIS] for each experiment. Green lines are Fermi-LAT sensitivities where lighter green is the sensitivity to the galactic center and dark green is its sensitivity to higher declinations. Orange, red, and purple solid lines represent the MAGIC, HESS, and VERITAS 50 hour sensitivities respectively. The maroon and brown lines are the HAWC 1 year and 5 year sensitivities. Across four decades of gamma-ray energy, these experiments have similar sensitivities on the order 10^{-12} erg $\text{cm}^{-2}\text{s}^{-1}$. The dotted lines are estimated dark matter fluxes assuming $m_\chi = 5$ TeV DM annihilating to bottom quarks (red), tau leptons (blue), and W bosons (green). Faded gray lines outline percentage flux of the Crab nebula. Figure is an augmented version of [25]

701 Sculptor and Carina were between January 2008 and December 2009. HESS’s observations of
 702 Coma Berenices were from 2010 to 2013, and Fornax was observed in 2010 [32, 33, 34]. MAGIC
 703 provided deep observations of Segue1 between 2011 and 2013 [35]. MAGIC also provides data
 704 for three dwarves: Coma Berenices, Draco, and Ursa Major II where observations were made
 705 in: January - June 2019 [36], March - September 2018 [36], and 2014 - 2016 [37] respectively.
 706 VERITAS provided data for Boötes I, Draco, Segue 1, and Ursa Minor from 2009 to 2016 [38].

707 This chapter presents the Glory Duck analysis, the name given for the search for dark matter
 708 annihilation from dSph by combining data from the five gamma-ray observatories: Fermi-LAT,
 709 HAWC, HESS, MAGIC, and VERITAS. Specifically, the methods in analysis and modeling are
 710 presented for the HAWC gamma-ray observatory. This work was published to the Journal of
 711 Cosmology and Astroparticle Physics and presented at the International Cosmic Ray Conference

712 in 2019, 2021, and 2023 [39, 40, 41] and others.

713 **5.2 Dataset and Background**

714 This section enumerates the data and background methods used for HAWC’s study of dSphs.
715 Section 5.2.1 and Section 5.2.2 are most useful for fellow HAWC collaborators looking to replicate
716 the Glory Duck analysis.

717 **5.2.1 Itemized HAWC files**

- 718 • Detector Resolution: `response_aerie_svn_27754_systematics_best_mc_test_no`
719 `broadpulse_10pctlogchargesmearing_0.63qe_25kHzNoise_run5481_curvatu`
720 `re0_index3.root`
- 721 • Data Map: `maps-20180119/liff/maptree_1024.root`
- 722 • Spectral Dictionary: `DM_CirrelliSpectrum_dict_gammas.npy`
- 723 • Analysis wiki: https://private.hawc-observatory.org/wiki/index.php/Glory_Duck_Multi-Experiment_Dark_Matter_Search

725 **5.2.2 Software Tools and Development**

726 This analysis was performed using HAL and 3ML [42, 43] in Python version 2. I built software
727 to implement the *A Poor Particle Physicist Cookbook for Dark Matter Indirect Detection* (PPPC)
728 [44] DM spectral model and dSphs spatial model from [45] for HAWC analysis. A NumPy version
729 of this dictionary was made for both Py2 and Py3. The code base for creating this dictionary is
730 linked on my GitLab sandbox:

- 731 • Py2: [Dictionary Generator \(Deprecated\)](#)
- 732 • Py3: [PPPC2Dict](#)

733 The analysis was performed using the f_{hit} framework performed in the HAWC Crab paper
734 [42]. The Python2 NumPy dictionary file for gamma-ray final states is `dmCirSpecDict.npy`. The
735 corresponding Python3 file is `DM_CirrelliSpectrum_dict_gammas.npy`. These files can also

736 be used for decay channels and the PPPC describes how [44]. All other software used for data
737 analysis, DM profile generation, and job submission to SLURM are also kept in my sandbox for
738 [the Glory Duck](#) project.

739 **5.2.3 Data Set and Background Description**

740 The HAWC data maps used for this analysis contain 1017 days of data between runs 2104
741 (2014-11-26) and 7476 (2017-12-20). They were generated from pass 4.0 reconstruction. The
742 analysis is performed using the f_{hit} energy binning scheme with bins (1-9) similar to what was done
743 for the Crab and previous HAWC dSph analysis [42, 46]. Bin 0 was excluded as it has substantial
744 hadronic contamination and poor angular resolution.

745 This analysis was done on dSphs because of their large DM mass content relative to baryonic
746 mass. We consider the following to estimate the background to this study.

- 747 • The dSphs are small in HAWC’s field of view, so the analysis is not sensitive to large or small
748 scale anisotropies.
- 749 • The dSphs used in this analysis are off the galactic plane.
- 750 • The dSphs are baryonically faint relative to their expected dark matter content and are not
751 expected to contain high energy gamma-ray sources.

752 Therefor we make no additional assumptions on the background from our sources and use
753 HAWC’s standard direct integration method for background estimation [42]. It is possible for
754 gamma rays from DM annihilation to scatter in transit to HAWC via Inverse Compton Scattering
755 (ICS). This was investigated and its impact on the flux is basically zero. Supporting information
756 on this is in Section 5.7.1

757 **5.3 Analysis**

758 The expected differential photon flux from DM-DM annihilation to standard model particles,
759 $d\Phi_\gamma/dE_\gamma$, over solid angle, Ω is described by the familiar equation.

$$\frac{d\Phi_\gamma}{dE_\gamma} = \frac{\langle\sigma v\rangle}{8\pi m_\chi^2} \frac{dN_\gamma}{dE_\gamma} \times \int_{\text{source}} d\Omega \int_{l.o.s} \rho_\chi^2 dl(r, \theta') \quad (5.1)$$

760 Where $\langle \sigma v \rangle$ is the velocity weighted annihilation cross-section. $\frac{dN}{dE}$ is the expected differential
 761 number of photons produced at each energy per annihilation. m_χ is the rest mass of the supposed
 762 DM particle. ρ_χ is the DM density. J is the astrophysical J-factor and is defined as

$$J = \int d\Omega \int_{l.o.s} dl \rho_\chi^2(r, \theta') \quad (5.2)$$

763 l is the distance to the source from Earth. r is the radial distance from the center of the source. θ' is
 764 the half angle defining a cone containing the DM source. How each component is synthesized and
 765 considered for HAWC's analysis is presented in the following sections. Section 5.3.1 presents the
 766 particle physics model for DM annihilation. Section 5.3.2 presents the spatial distributions built
 767 for each dSph.

768 **5.3.1 $\frac{dN_\gamma}{dE_\gamma}$ - Particle Physics Component**

769 For these spectra, we import the PPPC with Electroweak (EW) corrections [44]. The spectrum
 770 is implemented as a model script in astromodels for 3ML. The EW corrections were previously not
 771 considered for HAWC and are significant for DM annihilating to EW coupled SM particles such
 772 as all leptons, and the γ , Z , and W bosons [46]. Figure 5.2 demonstrates the significance of EW
 773 corrections for W boson annihilation. Across EW SM channels, the gamma-ray spectra become
 774 harder than spectra without EW corrections. Tables from the PPPC were reformatted into Python
 775 NumPy dictionaries for collaboration-wide use. A class in astromodels was developed to include
 776 the EW correction from the PPPC and is aptly named `PPPCSpectra` within `DM_models.py`.

777 **5.3.2 J - Astrophysical Component**

778 The J-factor profiles for each source are imported from Geringer-Sameth (referred to with \mathcal{GS})
 779 [45]. These were pulled from the publication as $J(\theta)$, where θ is the angular separation from the
 780 center of the source. HAWC requires maps in terms of $\frac{dJ}{d\Omega}$, so the conversion from the maps was
 781 done in the following way...

782 First, convert the angular distances to solid angles

$$\Omega = 2 \cdot \pi(1 - \cos(\theta)) \quad (5.3)$$

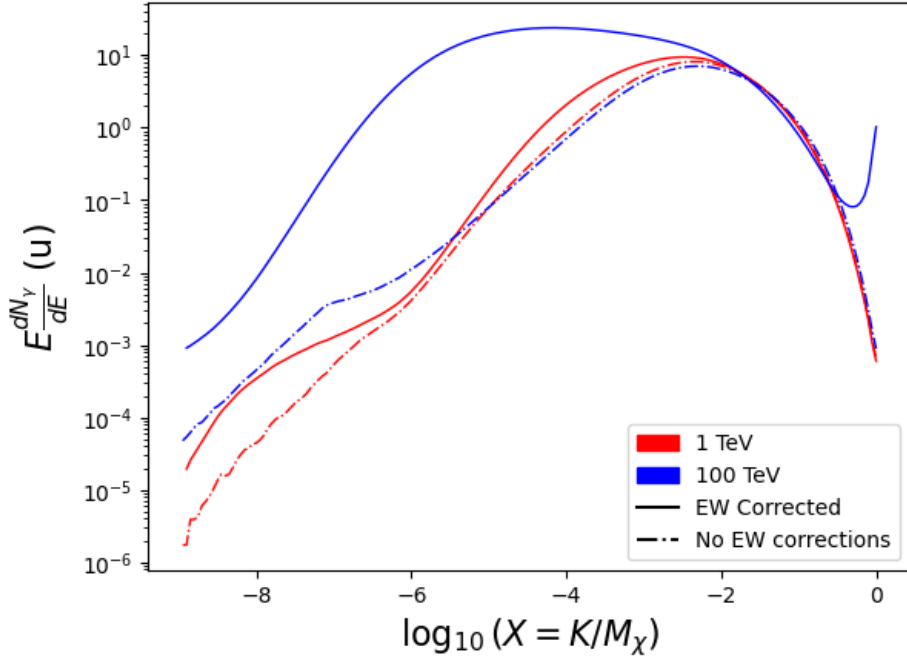


Figure 5.2 Effect of Electroweak (EW) corrections on expected DM annihilation spectrum for $\chi\chi \rightarrow W^-W^+$. Solid lines are spectral models that consider EW corrections. Dash-dot lines are spectral models without EW corrections. Red lines are models for $M_\chi = 1$ TeV. Blue lines represent models for $M_\chi = 100$ TeV. All models are sourced from the PPPC4DMID [44].

783 which reduces with a small angle approximation to $\pi\theta^2$. Next, the central difference for both the
 784 ΔJ and $\Delta\Omega$ value were calculated from the discretized $J(\theta)$ with the central difference stencil:

$$\Delta\phi_i = \phi_{i+1} - \phi_{i-1} \quad (5.4)$$

785 Where ϕ is either Ω or J . These were done separately in case the grid spacing in θ was not uniform.
 786 Finally, these lists are divided so that we are left with an approximation of the $dJ/d\Omega$ profile that
 787 is a function of θ . Admittedly, this is an approximation method for the map which introduces small
 788 errors compared to the true profile estimate. This was checked as a systematic against the author's
 789 profiling of the spatial distribution and is documented in Section 5.8.1.

790 With $\frac{dJ}{d\Omega}(\theta)$, a map is generated, first by filling in the north-east quadrant of the map. This
 791 quadrant is then reflected twice, vertically then horizontally, to fill the full map. Maps are then
 792 normalized by dividing the discrete 2D integral of the map. The 2D integral was a simple height

793 of bins, Newton's integral:

$$p^2 \cdot \sum_{i,j=0}^{N,M} \frac{dJ}{d\Omega}(\theta_{i,j}, \phi_{i,j}) \quad (5.5)$$

794 These maps are HEALpix maps with NSIDE 16384 and saved in the `.fits` format.

795 Another DM spatial distribution model from Bonnivard (\mathcal{B}) [47] was used for the Glory Duck
796 study. However, to save computational time, limits from \mathcal{GS} were scaled to \mathcal{B} instead of each
797 experiment performing a full study a second time. How these models compare is demonstrated
798 for each dSph in Figure 5.16 and Figure 5.17 Plots of these maps are provided for each source
799 in chapter A Examples of the two most impactful dSphs derived from \mathcal{GS} , Segue1 and Coma
800 Berenices are featured in Figure 5.3

801 5.3.3 Source Selection and Annihilation Channels

802 We use many of the dSphs presented in HAWC's previous dSph DM search [46]. HAWC's
803 sources for Glory Duck include Boötes I, Coma Berenices, Canes Venatici I + II, Draco, Hercules,
804 Leo I, II, + IV, Segue 1, Sextans, and Ursa Major I + II. A full description of all sources used
805 in Glory Duck is found in Table 5.1. Triangulum II was excluded from the Glory Duck analysis
806 because of large uncertainties in its J factor. Ursa Minor was excluded from HAWC's contribution
807 to the combination because the source extension model extended Ursa Minor beyond HAWC's field
808 of view. Ursa Minor was not expected to contribute significantly to the combined limit, so work
809 was not invested in a solution to include Ursa Minor.

810 This analysis improves on the previous HAWC dSph paper [46] in the following ways. Pre-
811 viously, the dSphs were treated and implemented as point sources. For this analysis, dSphs are
812 modeled and treated as extended source. The impact of this change with respect to the upper limit
813 is source dependent and is explored in Section 5.7.2. Previously, the particle physics model used for
814 gamma-ray spectra from DM annihilation did not have EW corrections where the PPPC includes
815 them. Finally, the gamma-ray ray dataset is much larger. The study performed here analyzes over
816 1000 days of data compared to 507.

817 The SM annihilation channels probed for the Glory Duck combination include $b\bar{b}$, $e\bar{e}$, $\mu\bar{\mu}$, $\tau\bar{\tau}$,
818 $t\bar{t}$, W^+W^- , and ZZ . A summary of all sources, with a description of each experiments' sensitivity

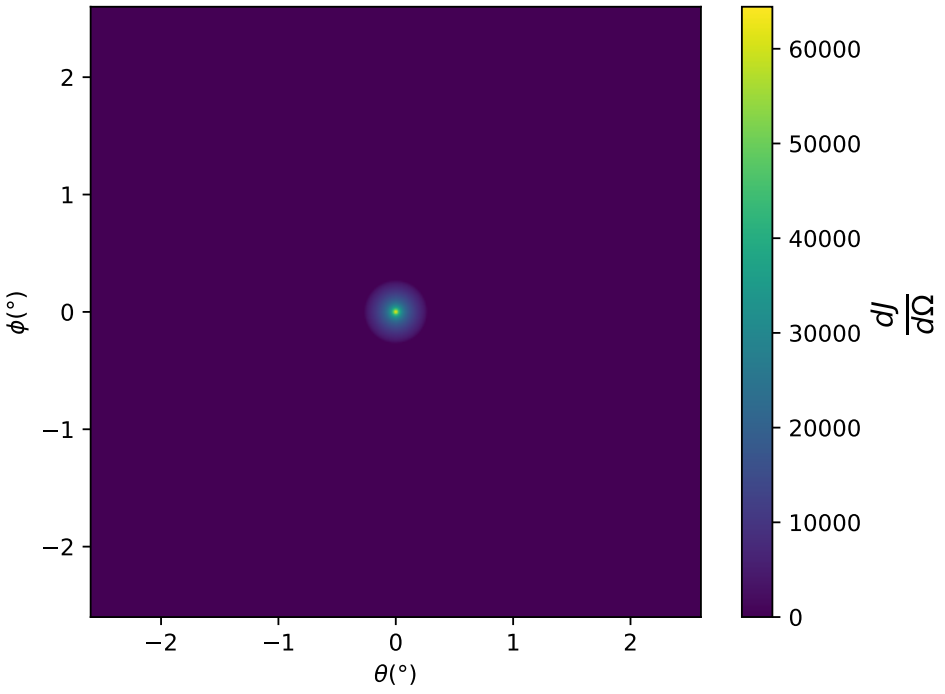
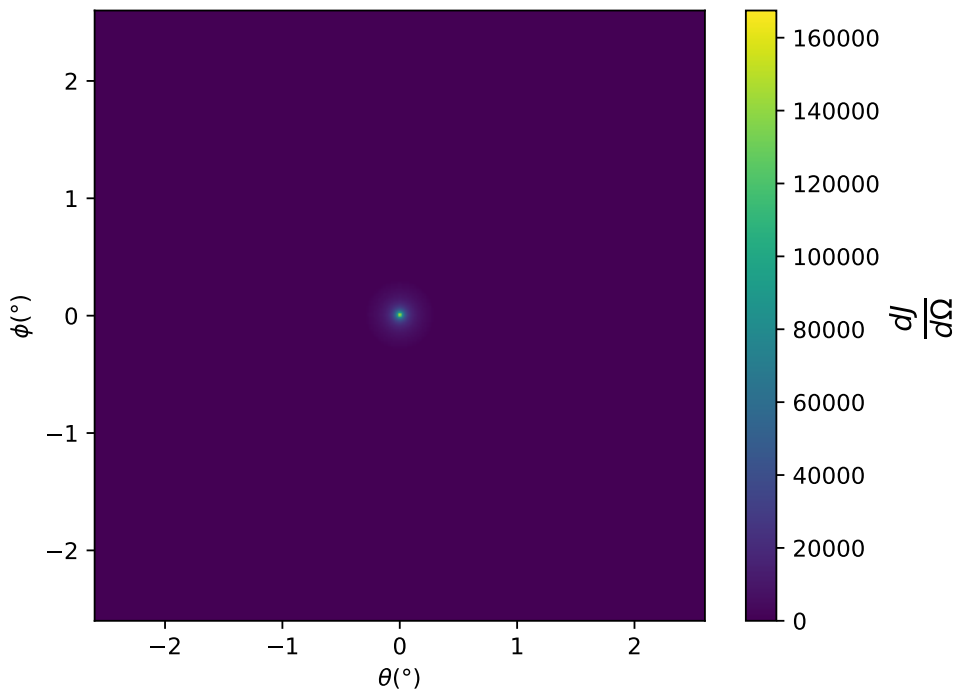


Figure 5.3 $\frac{dJ}{d\Omega}$ maps for Segue1 (top) and Coma Berenices (bottom). Origin is centered on the specific dwarf spheroidal galaxies (dSph). X and Y axes are the angular separation from the center of the dwarf. Plots of the remaining 11 dSph HAWC studied are linked in Fig. A.1.

Table 5.1 Summary of the relevant properties of the dSphs used in the present work. Column 1 lists the dSphs. Columns 2 and 3 present their heliocentric distance and galactic coordinates, respectively. Columns 4 and 5 report the J -factors of each source given from the \mathcal{GS} and \mathcal{B} independent studies and their estimated $\pm 1\sigma$ uncertainties. The values $\log_{10} J$ (\mathcal{GS} set) [45] correspond to the mean J -factor values for a source extension truncated at the outermost observed star. The values $\log_{10} J$ (\mathcal{B} set) [47] are provided for a source extension at the tidal radius of each dSph. **Bolded sources are within HAWC's field of view and provided to the Glory Duck analysis.**

Name	Distance (kpc)	l, b ($^{\circ}$)	$\log_{10} J$ (\mathcal{GS} set) $\log_{10}(\text{GeV}^2 \text{cm}^{-5} \text{sr})$	$\log_{10} J$ (\mathcal{B} set) $\log_{10}(\text{GeV}^2 \text{cm}^{-5} \text{sr})$
Boötes I	66	358.08, 69.62	$18.24^{+0.40}_{-0.37}$	$18.85^{+1.10}_{-0.61}$
Canes Venatici I	218	74.31, 79.82	$17.44^{+0.37}_{-0.28}$	$17.63^{+0.50}_{-0.20}$
Canes Venatici II	160	113.58, 82.70	$17.65^{+0.45}_{-0.43}$	$18.67^{+1.54}_{-0.97}$
Carina	105	260.11, -22.22	$17.92^{+0.19}_{-0.11}$	$18.02^{+0.36}_{-0.15}$
Coma Berenices	44	241.89, 83.61	$19.02^{+0.37}_{-0.41}$	$20.13^{+1.56}_{-1.08}$
Draco	76	86.37, 34.72	$19.05^{+0.22}_{-0.21}$	$19.42^{+0.92}_{-0.47}$
Fornax	147	237.10, -65.65	$17.84^{+0.11}_{-0.06}$	$17.85^{+0.11}_{-0.08}$
Hercules	132	28.73, 36.87	$16.86^{+0.74}_{-0.68}$	$17.70^{+1.08}_{-0.73}$
Leo I	254	225.99, 49.11	$17.84^{+0.20}_{-0.16}$	$17.93^{+0.65}_{-0.25}$
Leo II	233	220.17, 67.23	$17.97^{+0.20}_{-0.18}$	$18.11^{+0.71}_{-0.25}$
Leo IV	154	265.44, 56.51	$16.32^{+1.06}_{-1.70}$	$16.36^{+1.44}_{-1.65}$
Leo V	178	261.86, 58.54	$16.37^{+0.94}_{-0.87}$	$16.30^{+1.33}_{-1.16}$
Leo T	417	214.85, 43.66	$17.11^{+0.44}_{-0.39}$	$17.67^{+1.01}_{-0.56}$
Sculptor	86	287.53, -83.16	$18.57^{+0.07}_{-0.05}$	$18.63^{+0.14}_{-0.08}$
Segue I	23	220.48, 50.43	$19.36^{+0.32}_{-0.35}$	$17.52^{+2.54}_{-2.65}$
Segue II	35	149.43, -38.14	$16.21^{+1.06}_{-0.98}$	$19.50^{+1.82}_{-1.48}$
Sextans	86	243.50, 42.27	$17.92^{+0.35}_{-0.29}$	$18.04^{+0.50}_{-0.28}$
Ursa Major I	97	159.43, 54.41	$17.87^{+0.56}_{-0.33}$	$18.84^{+0.97}_{-0.43}$
Ursa Major II	32	152.46, 37.44	$19.42^{+0.44}_{-0.42}$	$20.60^{+1.46}_{-0.95}$
Ursa Minor	76	104.97, 44.80	$18.95^{+0.26}_{-0.18}$	$19.08^{+0.21}_{-0.13}$

819 to the source, is provided in Table 5.2.

820 5.4 Likelihood Methods

821 5.4.1 HAWC Likelihoods

822 For every analysis bin in energy, f_{hit} bins (1-9), and location, we can expect N signal events and
823 B background events. The expected number of excess signal events from dark matter annihilation,

Table 5.2 Summary of dSph observations by each experiment used in this work. A ‘-’ indicates the experiment did not observe the dSph for this study. For Fermi-LAT, the exposure at 1 GeV is given. For HAWC, $|\Delta\theta|$ is the absolute difference between the source declination and HAWC latitude. HAWC is more sensitive to sources with smaller $|\Delta\theta|$. For IACTs, we show the zenith angle range, the total exposure, the energy range, the angular radius θ of the signal or ON region, the ratio of exposures between the background-control (OFF) and signal (ON) regions (τ), and the significance of gamma-ray excess in standard deviations, σ .

Source name	Fermi-LAT	HAWC	H.E.S.S, MAGIC, VERITAS						
	Exposure (10^{11} s m 2)	$ \Delta\theta $ (°)	IACT	Zenith (°)	Exposure (h)	Energy range (GeV)	θ (°)	τ	S (σ)
Boötes I	2.6	4.5	VERITAS	15 – 30	14.0	100–41000	0.10	8.6	-1.0
Canes Venatici I	2.9	14.6	–	–	–	–	–	–	–
Canes Venatici II	2.9	15.3	–	–	–	–	–	–	–
Carina	3.1	–	H.E.S.S.	27 – 46	23.7	310 – 70000	0.10	18.0	-0.3
Coma Berenices	2.7	4.9	H.E.S.S.	47 – 49	11.4	550 – 70000	0.10	14.4	-0.4
			MAGIC	5 – 37	49.5	60 – 10000	0.17	1.0	–
			MAGIC	29 – 45	52.1	70 – 10000	0.22	1.0	–
Draco	3.8	38.1	VERITAS	25 – 40	49.8	120 – 70000	0.10	9.0	-1.0
Fornax	2.7	–	H.E.S.S.	11 – 25	6.8	230 – 70000	0.10	45.5	-1.5
Hercules	2.8	6.3	–	–	–	–	–	–	–
Leo I	2.5	6.7	–	–	–	–	–	–	–
Leo II	2.6	3.1	–	–	–	–	–	–	–
Leo IV	2.4	19.5	–	–	–	–	–	–	–
Leo V	2.4	–	–	–	–	–	–	–	–
Leo T	2.6	–	–	–	–	–	–	–	–
Sculptor	2.7	–	H.E.S.S.	10 – 46	11.8	200 – 70000	0.10	19.8	-2.2
Segue I	2.5	2.9	MAGIC	13 – 37	158.0	60 – 10000	0.12	1.0	-0.5
			VERITAS	15 – 35	92.0	80 – 50000	0.10	7.6	0.7
Segue II	2.7	–	–	–	–	–	–	–	–
Sextans	2.4	20.6	–	–	–	–	–	–	–
Ursa Major I	3.4	32.9	–	–	–	–	–	–	–
Ursa Major II	4.0	44.1	MAGIC	35 – 45	94.8	120 – 10000	0.30	1.0	-2.1
Ursa Minor	4.1	–	VERITAS	35 – 45	60.4	160 – 93000	0.10	8.4	-0.1

824 S , is estimated by convolving Equation (7.1) with HAWC's energy response and pixel point spread
 826 functions. I then compute the test statistic (TS) with the log-likelihood ratio test,

$$\text{TS} = -2 \ln \left(\frac{\mathcal{L}_0}{\mathcal{L}^{\max}} \right) \quad (5.6)$$

827 where \mathcal{L}_0 is the null hypothesis, or no DM emission, likelihood. \mathcal{L}^{\max} is the best fit signal
 828 hypothesis where $\langle \sigma v \rangle$ maximizes the likelihood. We calculate the likelihood of each source and
 829 model, assuming events are Poisson distributed, with

$$\mathcal{L} = \prod_i \frac{(B_i + S_i)^{N_i} e^{-(B_i + S_i)}}{N_i!} \quad (5.7)$$

830 where S_i is the sum of expected number of signal counts. B_i is the number of background counts
 831 observed. N_i is the total number of counts.

832 I also calculate an upper limit on $\langle \sigma v \rangle$ by calculating the 95% confidence level (CL). For the
 833 CL, we define a parameter, TS_{95} , as

$$\text{TS}_{95} \equiv \sum_{\text{bins}} \left[2N \ln \left(1 + \frac{\epsilon S_{\text{ref}}}{B} \right) - 2\epsilon S_{\text{ref}} \right] \quad (5.8)$$

834 where the expected signal counts from a dSph is scaled by ϵ . S_{ref} is the expected number of excess
 835 counts in a bin from DM emission from a dSph with a corresponding annihilation cross-section,
 836 $\langle \sigma v \rangle$. We scan ϵ such that

$$2.71 = \text{TS}_{\max} - \text{TS}_{95} \quad (5.9)$$

837 5.4.2 Glory Duck Joint Likelihood

838 The joint likelihood for the 5-experiment combination was done similarly as Section 5.4.1. We
 839 calculate upper limits on $\langle \sigma v \rangle$ from the TS, Eq. (5.6), and define the likelihood ratio more generally

$$\lambda(\langle \sigma v \rangle | \mathcal{D}_{\text{dSphs}}) = \frac{\mathcal{L}(\langle \sigma v \rangle; \hat{\nu} | \mathcal{D}_{\text{dSphs}})}{\mathcal{L}(\widehat{\langle \sigma v \rangle}; \hat{\nu} | \mathcal{D}_{\text{dSphs}})} \quad (5.10)$$

840 $\mathcal{D}_{\text{dSphs}}$ is the totality of observations across experiments and dSphs. ν are the nuisance parameters
 841 which are the J factors in this study. $\widehat{\langle \sigma v \rangle}$ and $\hat{\nu}$ are the respective estimate that maximize \mathcal{L}
 842 globally. Finally, $\hat{\nu}$ is the set of nuisance parameters that maximize \mathcal{L} for a fixed value of $\langle \sigma v \rangle$.

843 The *complete* joint likelihood, \mathcal{L} that encompasses all observations from all instruments and
 844 dSphs can be factorized into *partial* functions for each dSph l (with $\mathcal{L}_{\text{dSph},l}$) and its J factor (\mathcal{J}_l):

$$\mathcal{L}(\langle \sigma v \rangle; \nu | \mathcal{D}_{\text{dSphs}}) = \prod_{l=1}^{N_{\text{dSphs}}} \mathcal{L}_{\text{dSph},l}(\langle \sigma v \rangle; J_l, \nu_l | \mathcal{D}_l) \times \mathcal{J}_l(J_l | J_{l,\text{obs}}, \sigma_{\log J_l}). \quad (5.11)$$

845 For this study, $N_{\text{dSphs}} = 20$ is the number of dSphs studied. \mathcal{D}_l are the gamma-ray observations
 846 of dSph, l . ν_l are the nuisance parameters modifying the gamma-ray observations of dSph, l ,
 847 but excludes \mathcal{J}_l . \mathcal{J}_l is the J factor for dSph, l , as defined in Equation (5.2), and it is a nuisance
 848 parameter whose value is unknown. $\log_{10} J_{l,\text{obs}}$ and $\sigma_{\log J_l}$ are obtained from fitting a log-normal
 849 function of $J_{l,\text{obs}}$ to the posterior distribution of J_l [48]. $\log_{10} J_{l,\text{obs}}$ and $\sigma_{\log J_l}$ values are provided
 850 in Table 5.1. The term \mathcal{J}_l constraining J_l is written as:

$$\mathcal{J}_l(J_l | J_{l,\text{obs}}, \sigma_{\log J_l}) = \frac{1}{\ln(10)J_{l,\text{obs}}\sqrt{2\pi}\sigma_{\log J_l}} \exp\left(-\frac{(\log_{10} J_l - \log_{10} J_{l,\text{obs}})^2}{2\sigma_{\log J_l}^2}\right). \quad (5.12)$$

851 Both the \mathcal{GS} and \mathcal{B} , displayed in Table 5.1, sets of J factors are used in this analysis. Equation (5.12)
 852 is also normalized, so it can also be interpreted as a probability density function (PDF) for $J_{l,\text{obs}}$.
 853 From Equation (7.1), we can also see that $\langle \sigma v \rangle$ and J_l are degenerate when computing $\mathcal{L}_{\text{dSph},l}$.
 854 Therefore, as noted in [49], it is sufficient to compute $\mathcal{L}_{\text{dSph},l}$ versus $\langle \sigma v \rangle$ for a fixed value of J_l .
 855 We used $J_{l,\text{obs}}(\mathcal{GS})$ reported in Tab. 5.1, in order to perform the profile of \mathcal{L} with respect to J_l .
 856 The degeneracy implies that for any $J'_l \neq J_{l,\text{obs}}$ (in practice in our case we used $J'_l = J_{l,\text{obs}}(\mathcal{B})$ to
 857 compute results from a different set of J factors):

$$\mathcal{L}_{\text{dSph},l}(\langle \sigma v \rangle; J'_l, \nu_l | \mathcal{D}_l) = \mathcal{L}_{\text{dSph},l}\left(\frac{J'_l}{J_{l,\text{obs}}} \langle \sigma v \rangle; J_{l,\text{obs}}, \nu_l | \mathcal{D}_l\right), \quad (5.13)$$

858 which is a straightforward rescaling operation that reduces the computational needs of the profiling
 859 operation since:

$$\mathcal{L}(\langle \sigma v \rangle; \hat{\nu} | \mathcal{D}_{\text{dSphs}}) = \prod_{l=1}^{N_{\text{dSphs}}} \max_{J_l} \left[\mathcal{L}_{\text{dSph},l}(\langle \sigma v \rangle; J_l, \hat{\nu}_l | \mathcal{D}_l) \times \mathcal{J}_l(J_l | J_{l,\text{obs}}, \sigma_{\log J_l}) \right]. \quad (5.14)$$

860 In addition, Eq. (5.13) enables the combination of data from different gamma-ray instruments and
 861 observed dSphs via tabulated values of $\mathcal{L}_{\text{dSph},l}$, or equivalently of λ from Eq. (5.10) as was done in

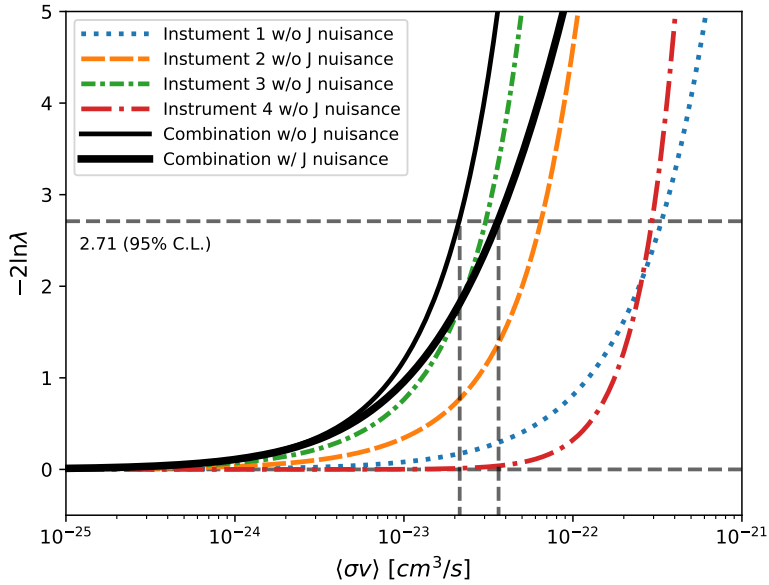


Figure 5.4 Illustration of the combination technique showing a comparison between $-2 \ln \lambda$ provided by four instruments (colored lines) from the observation of the same dSph without any J nuisance and their sum, *i.e.* the resulting combined likelihood (thin black line). According to the test statistics of Equation (5.6), the intersection of the likelihood profiles with the line $-2 \ln \lambda = 2.71$ indicates the 95% C.L. upper limit on $\langle \sigma v \rangle$. The combined likelihood (thin black line) shows a smaller value of upper limit on $\langle \sigma v \rangle$ than those derived by individual instruments. We also show how the uncertainties on the J factor effects the combined likelihood and degrade the upper limit on $\langle \sigma v \rangle$ (thick black line). All likelihood profiles are normalized so that the global minimum $\widehat{\langle \sigma v \rangle}$ is 0. We note that each profile depends on the observational conditions in which a target object was observed. The sensitivity of a given instrument can be degraded and the upper limits less constraining if the observations are performed in non-optimal conditions such as a high zenith angle or a short exposure time.

862 this work, versus $\langle \sigma v \rangle$. $\mathcal{L}_{\text{dSph},l}$ is computed for a fixed value of J_l and profiled with respect to all
 863 instrumental nuisance parameters ν_l , these nuisance parameters are discussed in more detail below.
 864 These values are produced by each detector independently and therefore there is no need to share
 865 sensitive low-level information used to produce them, such as event lists. Figure 5.4 illustrates the
 866 multi-instrument combination technique used in this study with a comparison of the upper limit
 867 on $\langle \sigma v \rangle$ obtained from the combination of the observations of four experiments towards one dSph
 868 versus the upper limit from individual instruments. It also shows graphically the effect of the
 869 J -factor uncertainty on the combined observations.

870 The *partial* joint likelihood function for gamma-ray observations of each dSph ($\mathcal{L}_{\text{dSph},l}$) is

written as the product of the likelihood terms describing the $N_{\text{exp},l}$ observations performed with any of our observatories:

$$\mathcal{L}_{\text{dSph},l} (\langle \sigma v \rangle; J_l, \nu_l | \mathcal{D}_l) = \prod_{k=1}^{N_{\text{exp},l}} \mathcal{L}_{lk} (\langle \sigma v \rangle; J_l, \nu_{lk} | \mathcal{D}_{lk}), \quad (5.15)$$

where each \mathcal{L}_{lk} term refers to an observation of the l -th dSph with associated k -th instrument responses. $N_{\text{exp},l}$ varies from dSph to dSph and can be inferred from Table 5.2.

Each collaboration separately analyzes their data for \mathcal{D}_{lk} corresponding to dSph l and gamma-ray detector k , using as many common assumptions as possible in the analysis. HAWC's treatment was described earlier in Section 5.4.1 whereas the specifics of the remaining experiments is left to the publication. We compute the values for the likelihood functions \mathcal{L}_{lk} (see Eq. (5.15)) for a fixed value of J_l and profile over the rest of the nuisance parameters ν_{lk} . Then, values of λ from Eq. (5.10) are computed as a function of $\langle \sigma v \rangle$, and shared using a common format. Results are computed for seven annihilation channels, W^+W^- , ZZ , $b\bar{b}$, $t\bar{t}$, e^+e^- , $\mu^+\mu^-$, and $\tau^+\tau^-$ over 62 m_χ values between 5 GeV and 100 TeV provided in [44]. The $\langle \sigma v \rangle$ range is defined between 10^{-28} and $10^{-18} \text{ cm}^3 \cdot \text{s}^{-1}$, with 1001 logarithmically spaced values. The likelihood combination, i.e. Equation (5.11), and profile over the J -factor to compute the profile likelihood ratio λ , Equation (5.10), are carried out with two different public analysis software packages, namely `gLike` [50] and `LklCom` [51], that provide the same results [52].

As mentioned previously, each experiment computes the \mathcal{L}_{lk} from Equation (5.10) differently. The remainder of this section highlights the differences in this calculation across the experiments. Four experiments, namely *Fermi*-LAT, H.E.S.S., HAWC and MAGIC, use a binned likelihood to compute the \mathcal{L}_{lk} . For these experiments, for each observation \mathcal{D}_{lk} of a given dSph l carried out using a given gamma-ray detector k , the binned likelihood function is:

$$\mathcal{L}_{lk} (\langle \sigma v \rangle; J_l, \nu_{lk} | \mathcal{D}_{lk}) = \prod_{i=1}^{N_E} \prod_{j=1}^{N_P} \left[\mathcal{P}(s_{lk,ij}(\langle \sigma v \rangle, J_l, \nu_{lk}) + b_{lk,ij}(\nu_{lk}) | N_{lk,ij}) \right] \times \mathcal{L}_{lk,\nu} (\nu_{lk} | \mathcal{D}_{\nu_{lk}}) \quad (5.16)$$

where N_E and N_P are the number of considered bins in reconstructed energy and arrival direction, respectively; \mathcal{P} represents a Poisson PDF for the number of gamma-ray candidate events $N_{lk,ij}$

894 observed in the i -th bin in energy and j -th bin in arrival direction, when the expected number is
 895 the sum of the expected mean number of signal events s_{ij} (produced by DM annihilation) and of
 896 background events b_{ij} ; $\mathcal{L}_{lk,\nu}$ is the likelihood term for the extra ν_{lk} nuisance parameters that vary
 897 from one instrument k to another. The expected counts for signal events s_{ij} for a given dSph l and
 898 detector k is given by:

$$s_{ij}(\langle\sigma\nu\rangle, J) = \int_{E'_{\min,i}}^{E'_{\max,i}} dE' \int_{P'_{\min,j}}^{P'_{\max,j}} d\Omega' \int_0^\infty dE \int_{\Delta\Omega_{tot}} d\Omega \int_0^{T_{\text{obs}}} dt \frac{d^2\Phi(\langle\sigma\nu\rangle, J)}{dEd\Omega} \text{IRF}(E', P' | E, P, t) \quad (5.17)$$

899 where E' and E are the reconstructed and true energies, P' and P the reconstructed and true
 900 arrival directions; $E'_{\min,i}$, $P'_{\min,j}$, $E'_{\max,i}$, and $P'_{\max,j}$ are their lower and upper limits of the i -th
 901 energy bin and the j -th arrival direction bin; T_{obs} is the (dead-time corrected) total observation
 902 time; t is the time along the observations; $d^2\Phi/dEd\Omega$ is the DM flux in the source region (see
 903 Equation (7.1)); and $\text{IRF}(E', P' | E, P, t)$ is the IRF, which can be factorized as the product of the
 904 effective collection area of the detector $A_{\text{eff}}(E, P, t)$, the PDFs for the energy estimator $f_E(E' | E, t)$,
 905 and arrival direction $f_P(P' | E, P, t)$ estimators. Note that for Fermi-LAT, HAWC, MAGIC, and
 906 VERITAS the effect of the finite angular resolution is taken into account through the convolution
 907 of $d\Phi/dEd\Omega$ with f_P in Equation (5.17), whereas in the cases of H.E.S.S. f_P is approximated by a
 908 delta function. This approximation has been made in order to maintain compatibility of the result
 909 with what has been previously published. The difference introduced by this approximation is $< 5\%$
 910 for all considered dSphs. A more comprehensive review of the differences between the analyses of
 911 different instruments can be found in [25].

912 5.5 HAWC Results

913 13 of the 20 dSphs considered for the Glory Duck analysis are within HAWC's field of view.
 914 These dSph are analyzed for emission from DM annihilation according to the likelihood method
 915 described in Section 5.4. The 13 likelihood profiles are then stacked to synthesize a combined
 916 limit on the dark matter cross-section, $\langle\sigma\nu\rangle$. This combination is done for the 7 SM annihilation
 917 channels used in the Glory Duck analysis. Figure 5.5 shows the combined limit for all annihilation
 918 channels with HAWC only observations. We also perform 300 studies of Poisson trials on the

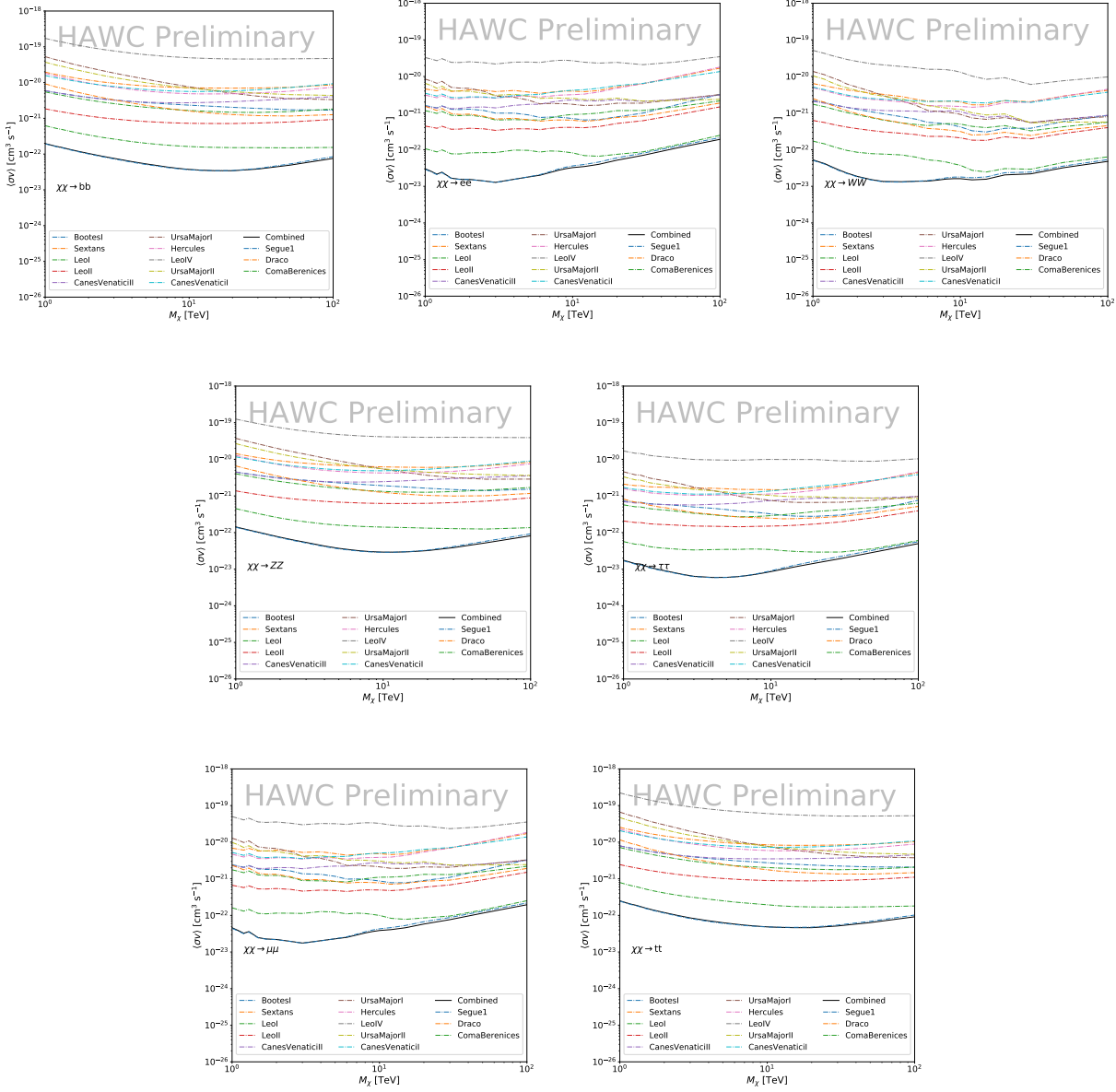


Figure 5.5

background. These trials are used to produce HAWC Brazil bands which were shared with the other collaborators for combined Brazil Bands. The results on fitting to HAWC's Poisson trials of the DM hypothesis is shown in Figure 5.7 for all the DM annihilation channels studied for Glory Duck.

No DM was found in HAWC observations. HAWC's limits are dominated by the dSphs Segue1 and Coma Berenices. The remaining 11 dSphs do not contribute significantly to the limit because

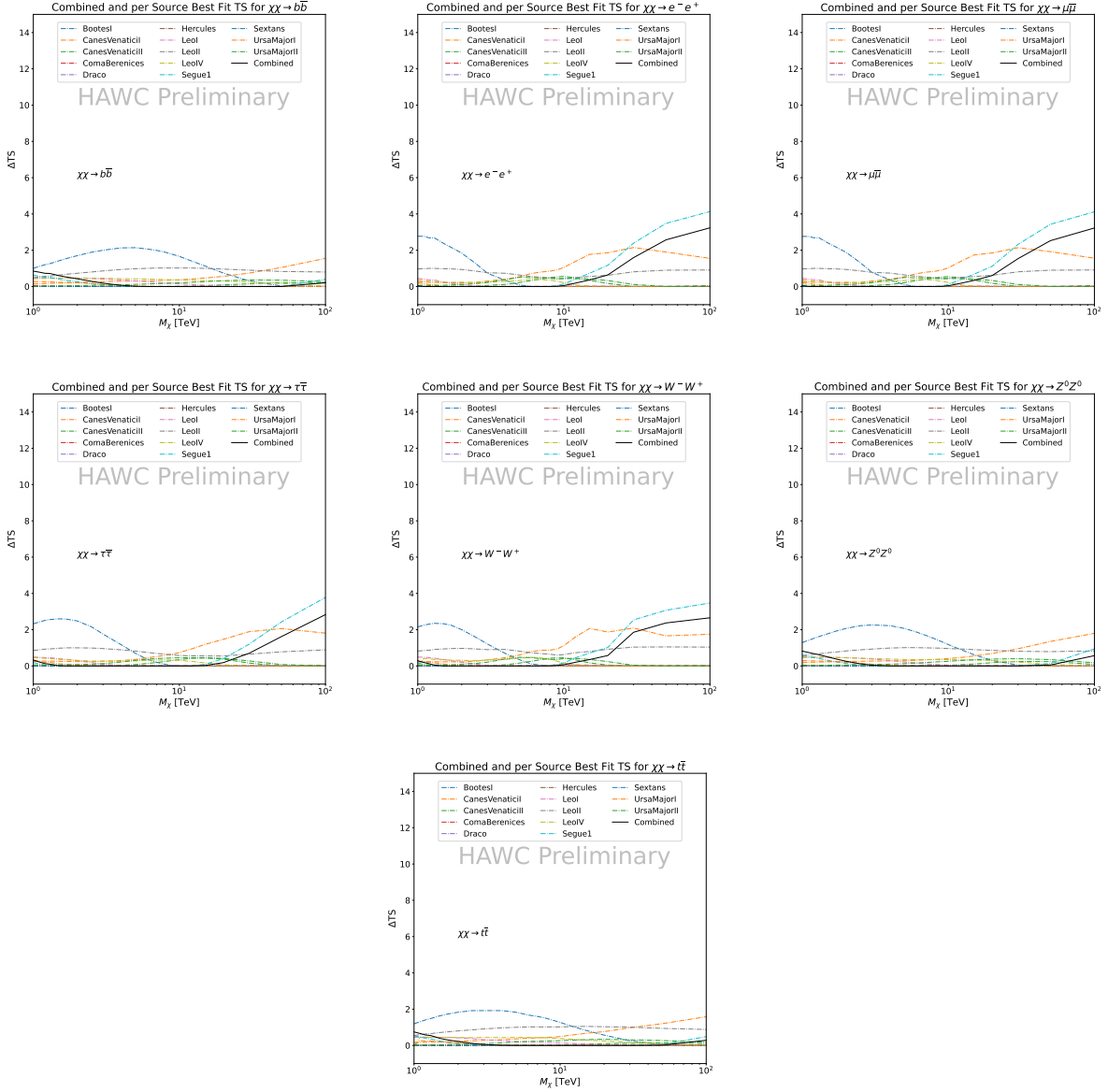


Figure 5.6 HAWC TS values for best fit $\langle \sigma v \rangle$ versus m_χ for seven SM annihilation channels with J factors from \mathcal{GS} . The solid black line shows the combined best fit TS values. The colored, dashed lines are the TS values for each of the 13 sources HAWC studied.

925 they are at high zenith and/or have much smaller J factors. Even though some remaining dSphs
 926 have large J factors, they are towards the edge of HAWC's field of view where HAWC analysis is
 927 less sensitive.

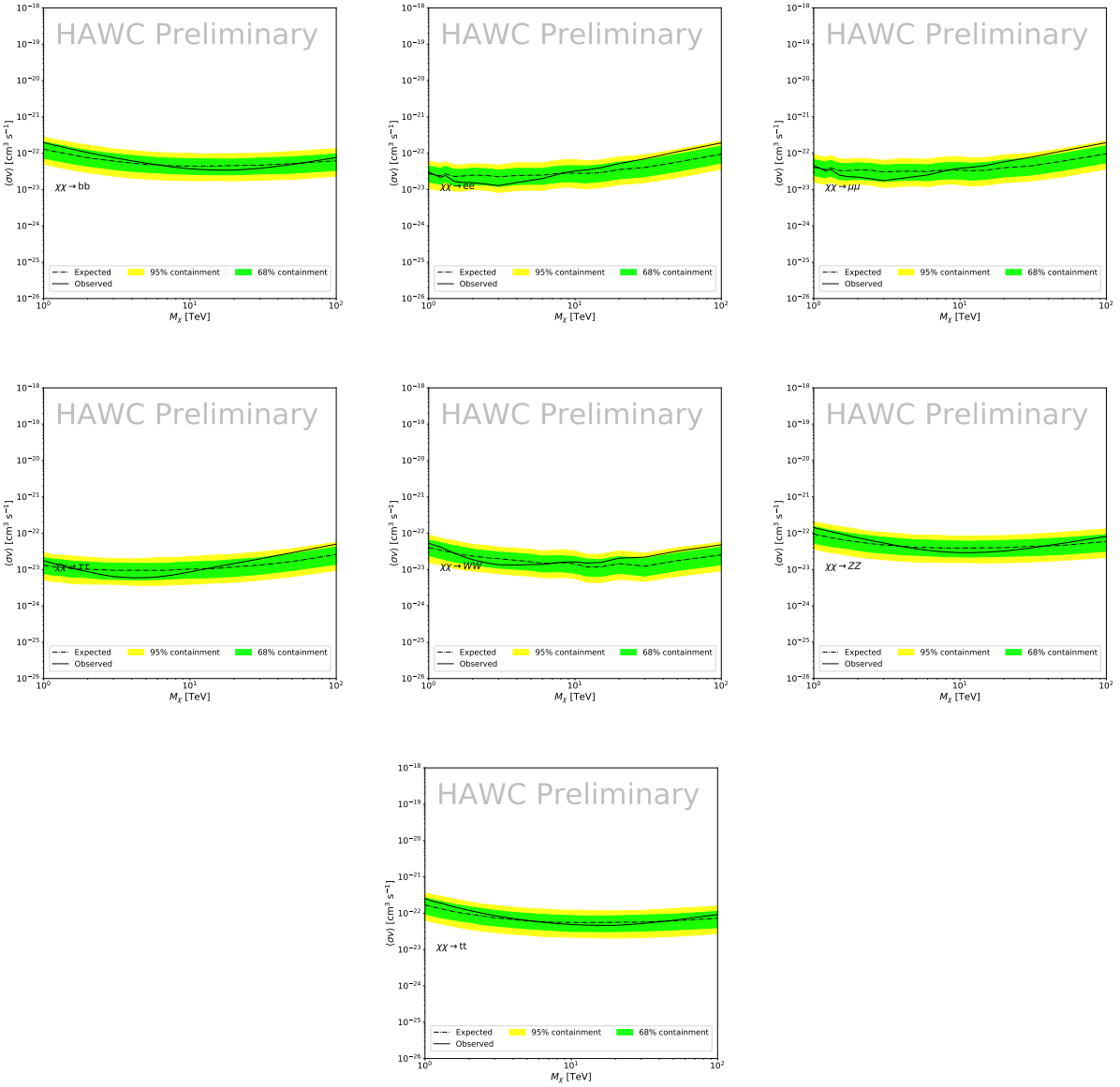


Figure 5.7 HAWC Brazil bands at 95% confidence level on $\langle\sigma v\rangle$ versus DM mass for seven annihilation channels with J -factors from \mathcal{GS} [53]. The solid line represents the combined limit from 13 dSphs. The dashed line is the expected limit. The green band is the 68% containment. The yellow band is the 95% containment.

928 5.6 Glory Duck Combined Results

929 The crux of this analysis is that HAWC's results are combined with 4 other gamma-ray observa-
 930 tories: Fermi-LAT, H.E.S.S., MAGIC, and VERITAS. No significant DM emission was observed
 931 by any of the five instruments. We present the upper limits on $\langle\sigma v\rangle$ assuming seven independent
 932 DM self annihilation channels, namely W^+W^- , Z^+Z^- , $b\bar{b}$, $t\bar{t}$, e^+e^- , $\mu^+\mu^-$, and $\tau^+\tau^-$. The 68%

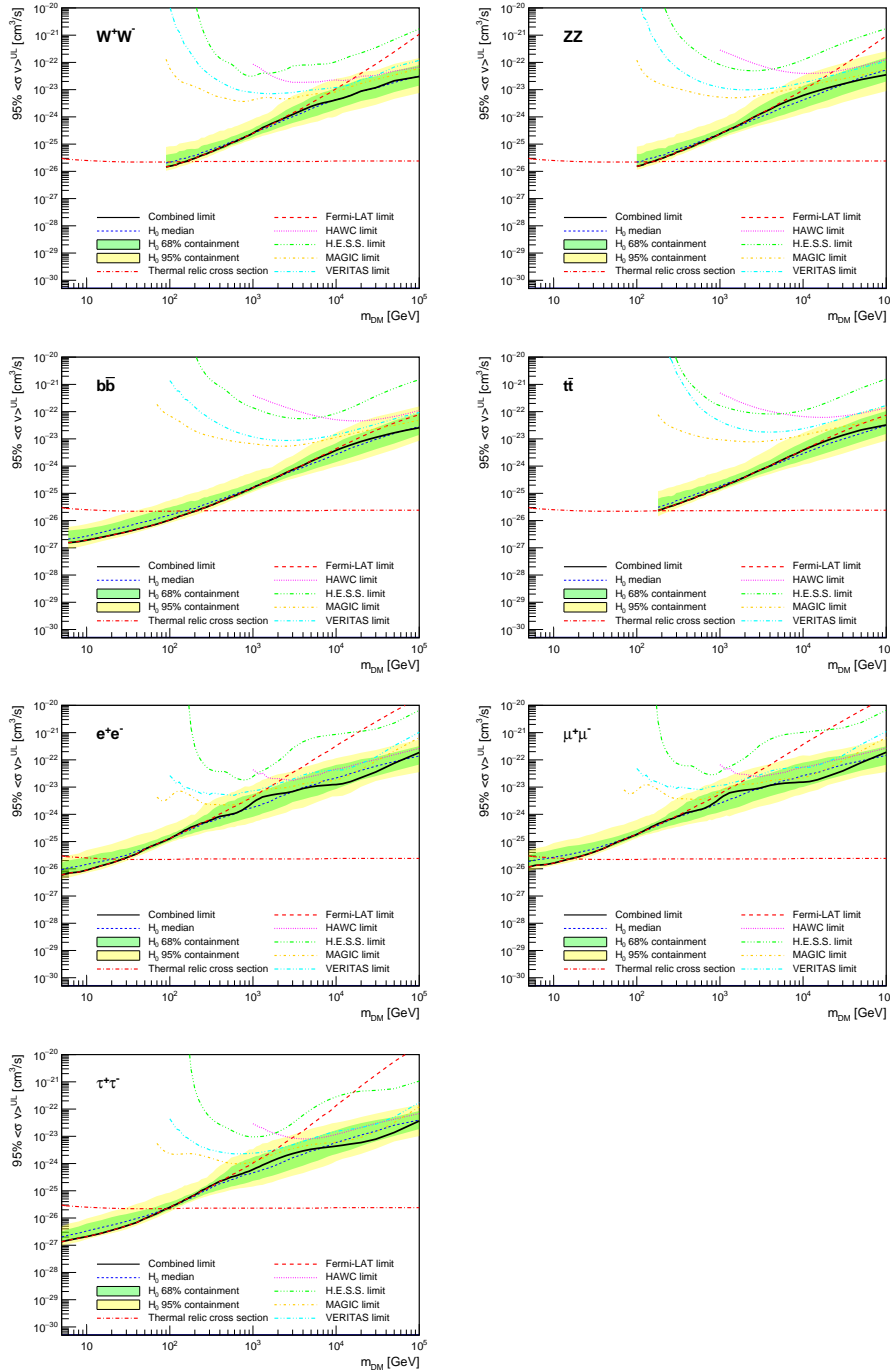


Figure 5.8 Upper limits at 95% confidence level on $\langle\sigma v\rangle$ in function of the DM mass for eight annihilation channels, using the set of J factors from Ref. [53] (\mathcal{GS} set in Table 5.1). The black solid line represents the observed combined limit, the black dashed line is the median of the null hypothesis corresponding to the expected limit, while the green and yellow bands show the 68% and 95% containment bands. Combined upper limits for each individual detector are also indicated as solid, colored lines. The value of the thermal relic cross-section in function of the DM mass is given as the red dotted-dashed line [54].

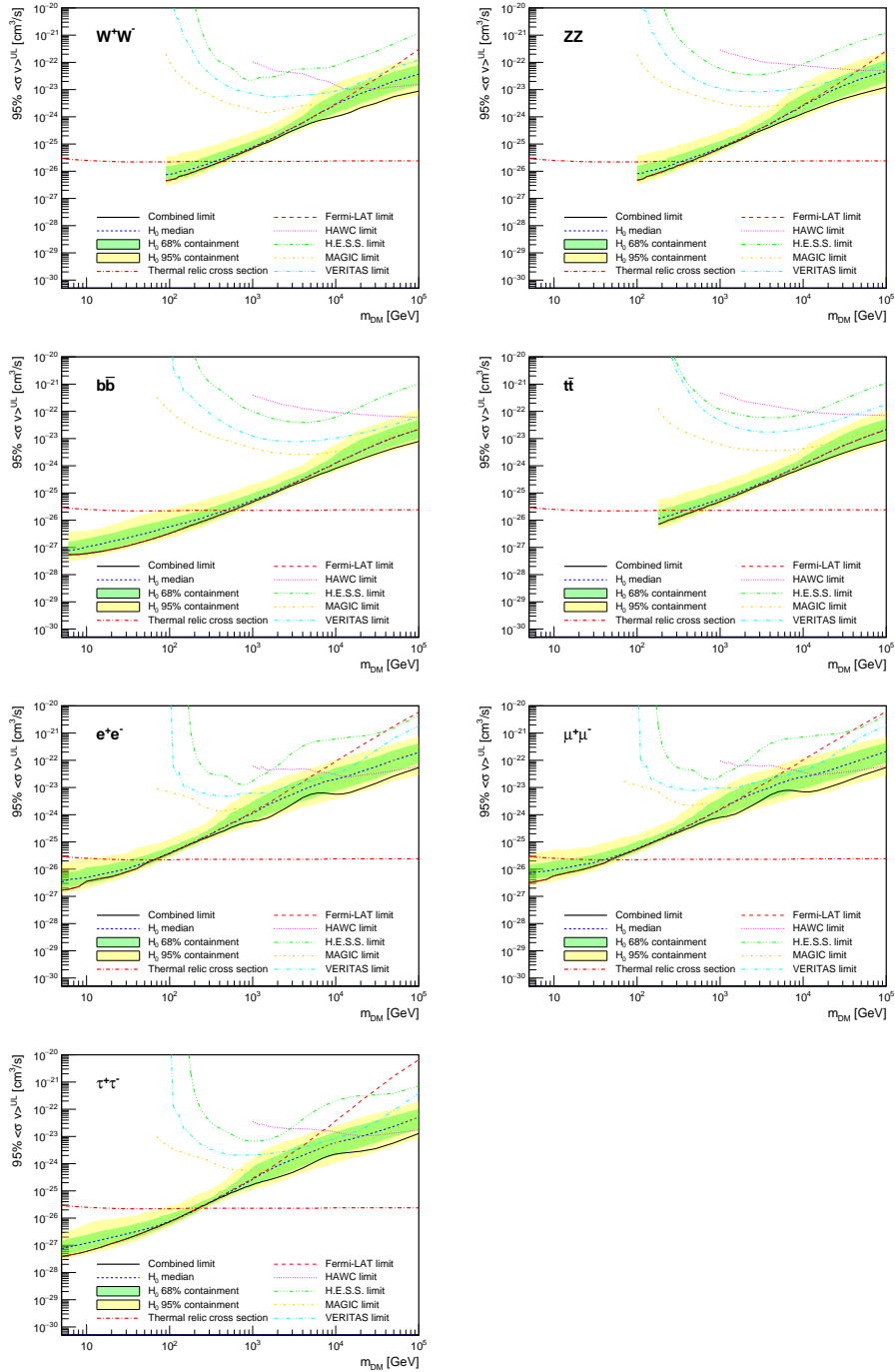


Figure 5.9 Same as Fig. 5.8, using the set of J factors from Ref. [47, 55] (\mathcal{B} set in Table 5.1).

and 95% containment bands are produced from 300 Poisson realizations of the null hypothesis corresponding to each of the combined datasets. These 300 realizations are combined identically to dSph observations. The containment bands and the median are extracted from the distribution of resulting limits on the null hypothesis. These 300 realizations are obtained either by fast simu-

937 lations of the OFF observations, for H.E.S.S., MAGIC, VERITAS, and HAWC, or taken from real
938 observations of empty fields of view in the case of Fermi-LAT [48, 56, 57].

939 The obtained limits are shown in Figure 5.8 for the $\mathcal{G}\mathcal{S}$ set of J -factors [53] and in Figure 5.9
940 for the \mathcal{B} set of J -factors [47, 55]. The combined limits are presented with their 68% and 95%
941 containment bands, and are expected to be close to the median limit when no signal is present.
942 We observe agreement with the null hypothesis for all channels, within 2σ standard deviations,
943 between the observed limits and the expectations given by the median limits. Limits obtained from
944 each detector are also indicated in the figures, where limits for all dSphs observed by the specific
945 instrument have been combined.

946 Below ~ 300 GeV, the *Fermi*-LAT dominates the DM limits for all annihilation channels. From
947 ~ 300 GeV to ~ 2 TeV, *Fermi*-LAT continues to dominate for the hadronic and bosonic DM channels,
948 yet the IACTs (H.E.S.S., MAGIC, and VERITAS) and *Fermi*-LAT all contribute to the limit for
949 leptonic DM channels. For DM masses between ~ 2 TeV to ~ 10 TeV, the IACTs dominate leptonic
950 DM annihilation channels, whereas both the *Fermi*-LAT and the IACTs dominate bosonic and
951 hadronic DM annihilation channels. From ~ 10 TeV to ~ 100 TeV, both the IACTs and HAWC
952 contribute significantly to the leptonic DM limit. For hadronic and bosonic DM, the IACTs and
953 *Fermi*-LAT both contribute strongly.

954 We notice that the limits computed using the \mathcal{B} set of J -factor are always better compared to the
955 ones calculated with the $\mathcal{G}\mathcal{S}$ set. For the W^+W^- , Z^+Z^- , $b\bar{b}$, and $t\bar{t}$ channels, the ratio between the
956 limits computed with the two sets of J -factor is varying between a factor of ~ 3 and ~ 5 depending
957 on the energy, with the largest ratio around 10 TeV. For the channels e^+e^- , $\mu^+\mu^-$, and $\tau^+\tau^-$, the
958 ratio lies between ~ 2 to ~ 6 , being maximum around 1 TeV. Examining Figure 5.16 and Figure 5.17
959 in Section 5.8, these differences are explained by the fact that the \mathcal{B} set provides higher J -factors
960 for the majority of the studied dSphs, with the notable exception of Segue I. The variation on the
961 ratio of the limits for the two sets is due to different dSph dominating the limits depending on the
962 energy. This pushes the range of thermal cross-section which can be excluded to higher mass. This
963 comparison demonstrates the magnitude of systematic uncertainties associated with the choice of

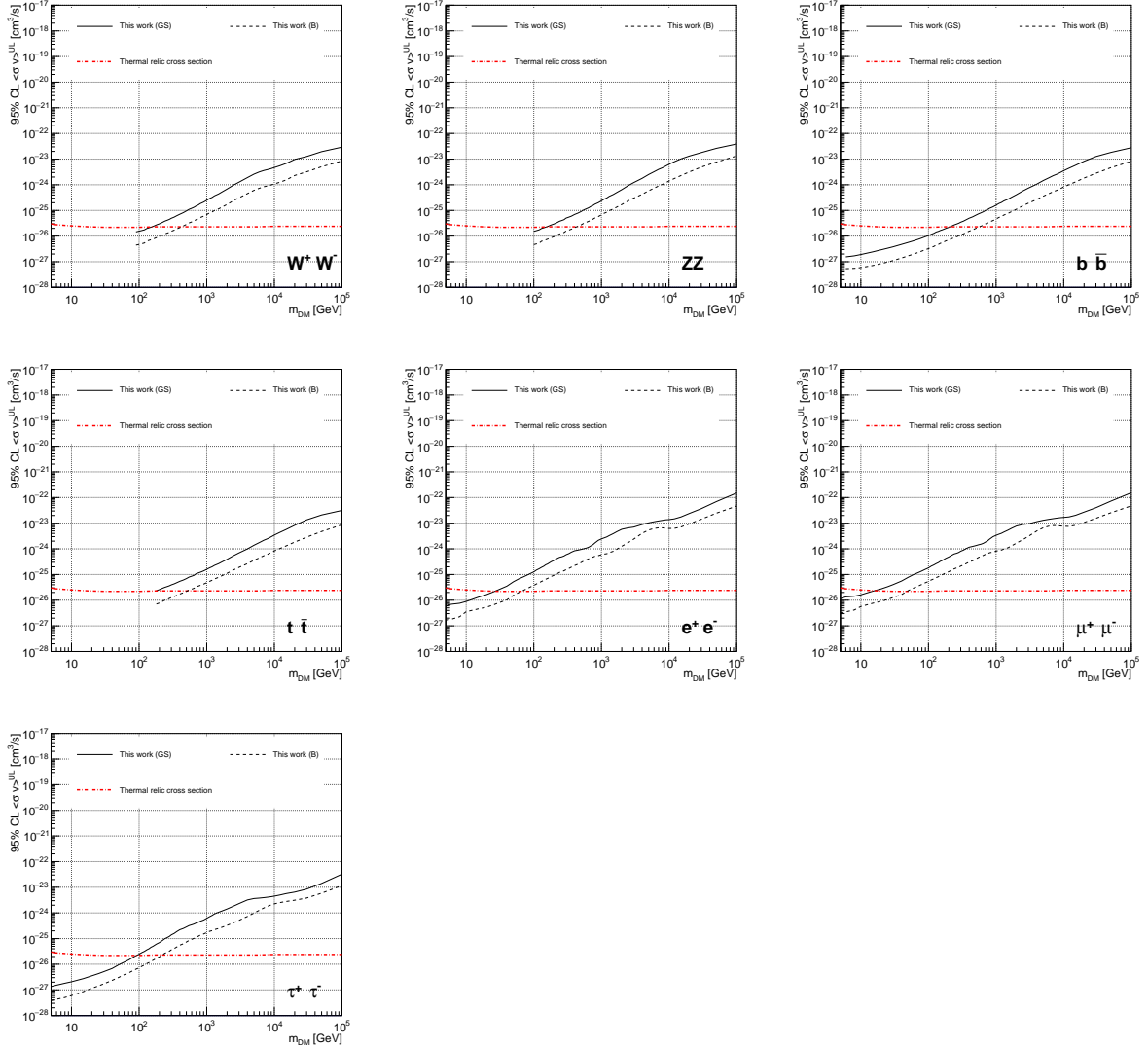


Figure 5.10 Comparisons of the combined limits at 95% confidence level for each of the eight annihilation channels when using the J factors from Ref. [53] (\mathcal{GS} set in Table 5.1), plain lines, and the J factor from Ref. [47, 55] (\mathcal{B} set in Table 5.1), dashed lines. The cross-section given by the thermal relic is also indicated [54].

964 the J -factor

965 This comparison demonstrates the magnitude of systematic uncertainties associated with the
966 choice of the J -factor calculation. The \mathcal{GS} and \mathcal{B} sets present a difference in the limits for all
967 channels of about This difference is explained, see Figure 5.16 and Figure 5.17 in Appendix, by the
968 fact that the \mathcal{B} set provides higher J factors for all dSph except for Segue I. This pushes the range
969 of thermal cross-section which can be excluded to higher mass.

970 **5.7 HAWC Systematics**

971 **5.7.1 Inverse Compton Scattering**

972 The DM-DM annihilation channels produce many high energy electrons regardless of the
973 primary annihilation channel. These high energy electrons can produce high energy gamma-rays
974 through Inverse Compton Scattering (ICS). If this effect is strong, it would change the morphology
975 of the source and increase the total expected gamma-ray counts from any source. The PPPC [44]
976 provides tools in Mathematica for calculating the impact of ICS for an arbitrary location in the
977 sky for a specified annihilation channel. We calculated the change in gamma-ray counts for DM
978 annihilation to primary $e\bar{e}$ for RA and Dec corresponding to Segue1 and Coma Berenices. These
979 dSphs were chosen because they are the strongest contributors to the limit. $e\bar{e}$ was selected because
980 it would have the largest number of high energy electrons. The effect was found to be on the order
981 of 10^{-7} on the gamma-ray spectrum. As a result, this systematic is not considered in our analysis.

982 **5.7.2 Point Source Versus Extended Source Limits**

983 The previous DM search toward dSph approximated the dSphs as point sources [46]. In
984 this analysis, the dSphs are implemented as extended with J-factor distributions following those
985 produced by [53]. The resolution of the cited map is much finer than HAWC's angular resolution.
986 The vast majority of the J-factor distribution is represented on the central HAWC pixel of the dSph
987 spatial map. However, the neighboring 8 pixels are not negligible and contribute to our limit.

988 Figure 5.11 shows a substantial improvement to the limit for Segue1. Fig. 5.12 however showed
989 identical limits. These disparities are best explained by the relative difference in their J-Factors.
990 Both dSphs pass almost overhead the HAWC detector, however Segue1 has the larger J-Factor
991 between the two. Adjacent pixels to the central pixel will therefore contribute to the limits. This is
992 the case for other dSph that are closer to overhead the HAWC detector.

993 Comparison plots for all sources and the combined limit can be found in the sandbox for the
994 Glory Duck project.

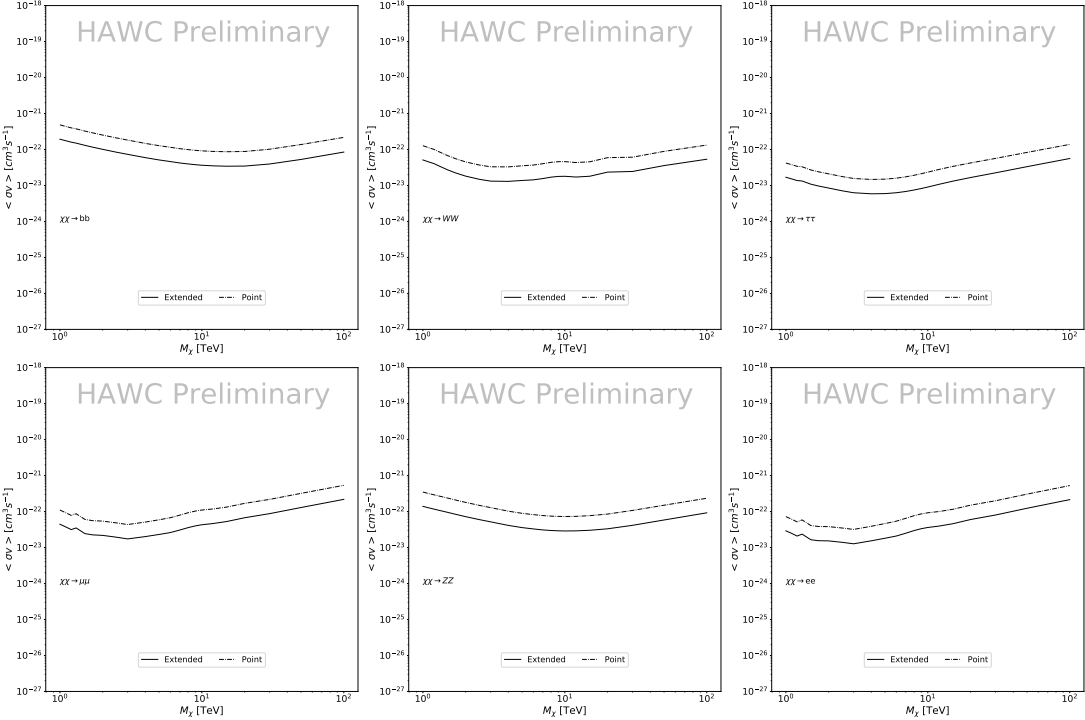


Figure 5.11 Comparisons of the combined limits at 95% confidence level for a point source analysis and extended source using [53] \mathcal{GS} J-factor distributions and PPPC [44] annihilation spectra. Shown are the limits for Segue1 which will have the most significant impact on the combined limit. 6 of the 7 DM annihilation channels are shown. Solid lines are extended source studies. Dashed lines are point source studies. Overall, the extended source analysis improves the limit by a factor of 2.

5.7.3 Impact of Pointing Systematic

During the analysis it was discovered that reconstruction of gamma-rays. Slides describing this systematic can be found [here](#). Shown on the presentation is dependence on the pointing systematic on declination. New spatial profiles were generated for every dSph and limits were computed for the adjusted declination.

Section 5.7.3 demonstrates the impact of this systematic for all DM annihilation channels studied by HAWC. The impact is a tiny improvement, yet mostly identical, to the combined limits.

5.8 J-factor distributions

5.8.1 Numerical integration of \mathcal{GS} maps

It was discovered well after the HAWC analysis was completed that the published tables from \mathcal{GS} [45] quoted median J-factors were computed in a non-trivial manner. The assumption myself

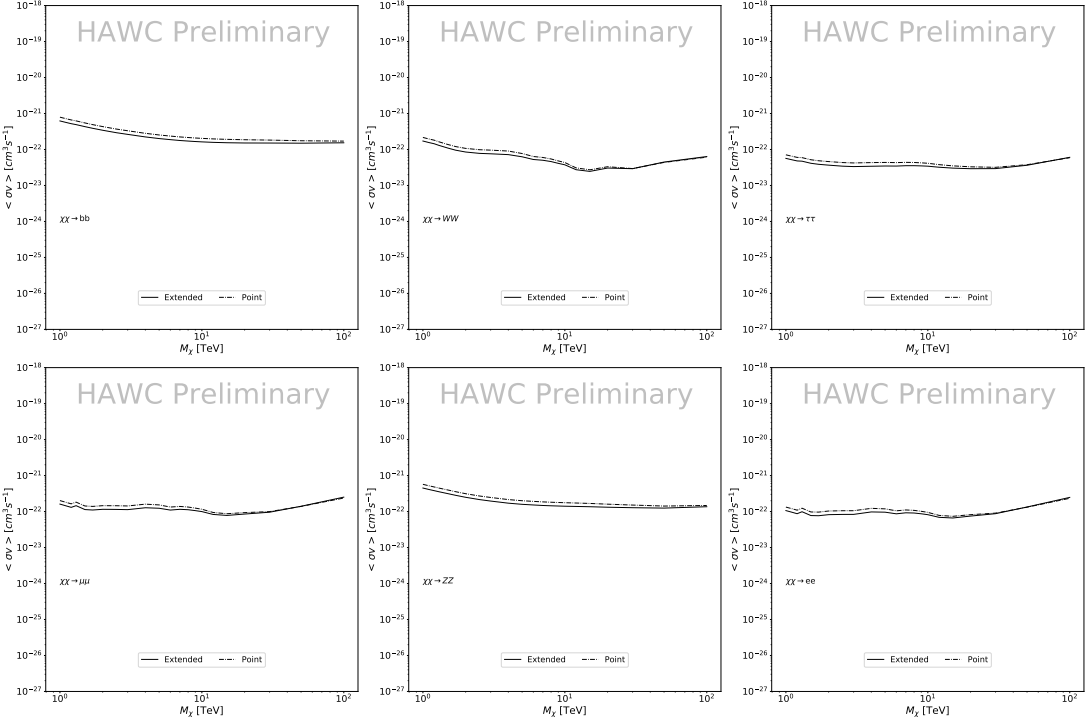


Figure 5.12 Same as Fig. 5.11 on Coma Berenices. This dSph also contributes significantly to the limit. The limits are identical in this case.

and collaborators had been that the published tables represented the J -factor as a function of θ for the best global fit model on a per-source basis. However, this is not the case. Instead, what is published are the best fit model for each dwarf that only considers stars up to the angular separation θ . Therefore, the model is changing for each value of θ for each dwarf. Yet, the introduced features from unique models at each θ are much smaller than the angular resolution of HAWC. It is not expected for these effects to impact the limits and TS greatly as a result.

Median J -factor model profiles were provided by the authors. New maps were generated and analyzed for Segue1 and Coma Berenices. Figure 5.14 shows the differential between maps generated with the method from Section 5.8.1 and from the authors of [45]. These maps were reanalyzed for all SM DM annihilation channels. Upper limits for these channels are shown in Figure 5.15

From Figure 5.15, we can see that the impact of these model difference was no substantial. The observed impact was a fractional effect which is much smaller than the impact from selecting another DM spatial distribution model as was shown in Figure 5.10.

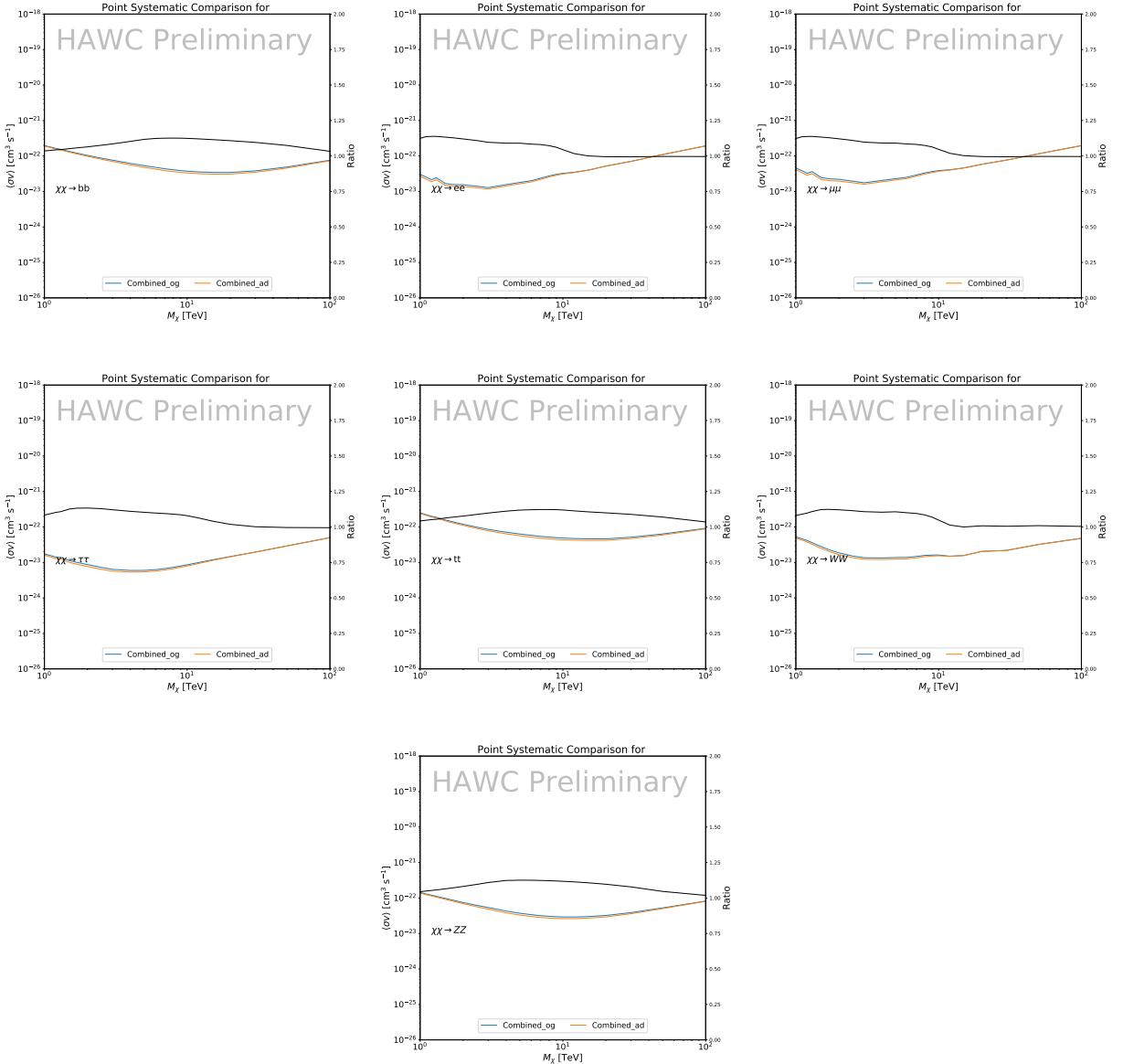


Figure 5.13 Comparison of combined limits when correcting for HAWC's pointing systematic. All DM annihilation channels are shown. The solid black line is the ratio between published limit to the declination corrected limit. The blue solid line or "Combined_og" represented the limits computed for Glory Duck. The solid orange line or "Combined_ad" represented the limits computed after correcting for the pointing systematic.

1020 5.8.2 $\mathcal{G}\mathcal{S}$ Versus \mathcal{B} spatial models

1021 We show in this appendix a comparison between the J -factors computed by Geringer-Sameth
 1022 *et al.* [53] (the $\mathcal{G}\mathcal{S}$ set) and the ones computed by Bonnivard *et al.* [47, 55] (the \mathcal{B} set). The
 1023 $\mathcal{G}\mathcal{S}$ J -factors are computed through a Jeans analysis of the kinematic stellar data of the selected

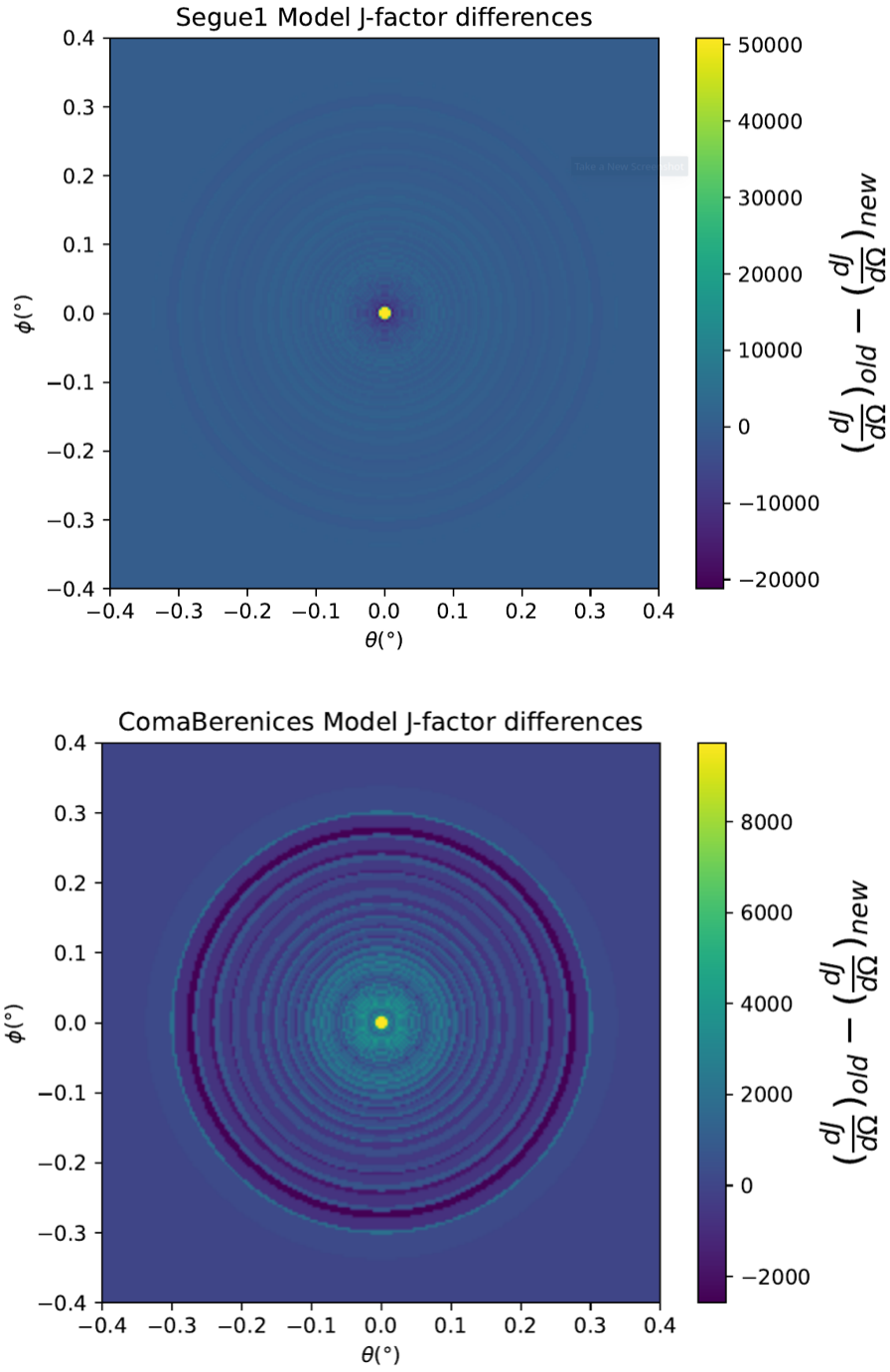


Figure 5.14 Differential map of dJ/Ω from model built in Section 5.8.1 and profiles provided directly from authors. (Top) Differential from Segue1. (bottom) Differential from Coma Berenices. Note that their scales are not the same. Segue1 shows the deepest discrepancies which is congruent with its large uncertainties. Both models show anuli where unique models become apparent.

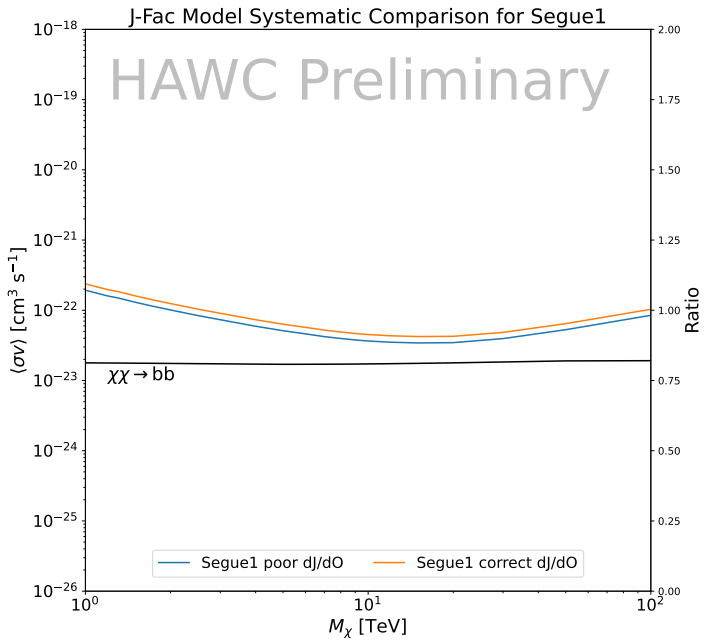
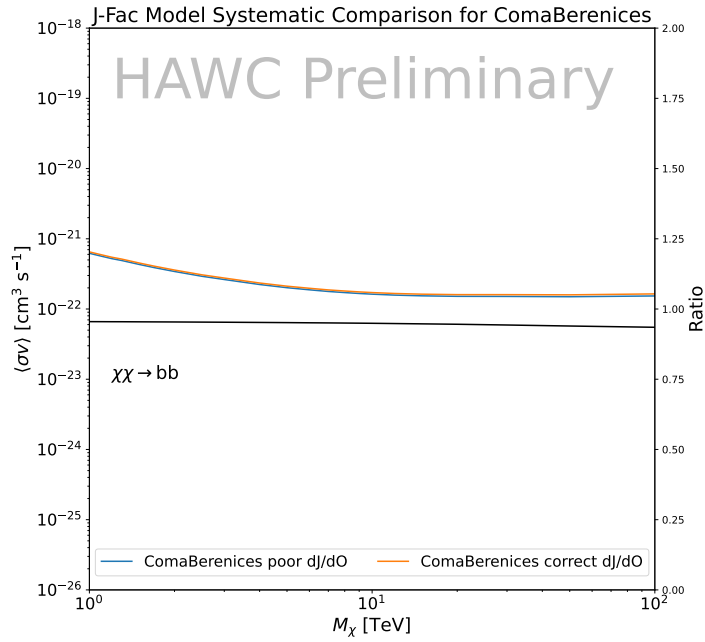


Figure 5.15 HAWC limits for Coma Berenices (top) and Segue1 (bottom) for two different map sets. Blue lines are limits calculated on maps with poor model representation. Orange lines are limits calculated on spatial profiles provided by the authors of [45]. Black line is the ratio of the poor spatial model limits to the corrected spatial models. The left y-axis measures $\langle \sigma v \rangle$ for the blue and orange lines. The right y-axis measures the ratio and is unitless.

1024 dSphs, assuming a dynamic equilibrium and a spherical symmetry for the dSphs. They adopted
1025 the generalized DM density distribution, known as Zhao-Hernquist, introduced by [58], carrying
1026 three additional index parameters to describe the inner and outer slopes, and the break of the
1027 density profile. Such a profile parametrization allows the reduction of the theoretical bias from
1028 the choice of a specific radial dependency on the kinematic data. In other words, the increase of
1029 free parameters with the use of the Zhao-Hernquist profile allows a better description of the mass
1030 density distribution of dark matter.

1031 In addition, a constant velocity anisotropy profile and a Plummer light profile [59] for the stellar
1032 distribution were assumed. The velocity anisotropy profile depends on the radial and tangential
1033 velocity dispersion. However, its determination remains challenging since only the line-of-sight
1034 velocity dispersion can be derived from velocity measurements. Therefore, the parametrization of
1035 the anisotropy profile is obtained from simulated halos (see [60] for more details). They provide the
1036 values of the J -factors of regions extending to various angular radius up to the outermost member
1037 star.

1038 The \mathcal{B} J -factors were computed through a Jeans analysis taking into account the systematic
1039 uncertainties induced by the DM profile parametrization, the radial velocity anisotropy profile, and
1040 the triaxiality of the halo of the dwarf galaxies. They performed a more complete study of the dSph
1041 kinematics and dynamics than \mathcal{GS} for the determination of the J -factor. Conservative values of the
1042 J -factors where obtained using an Einasto DM density profile [61], a realistic anisotropy profile
1043 known as the Baes & Van Hese profile [62] which takes into account that the inner regions can be
1044 significantly non-isotropic, and a Zhao-Hernquist light profile [58].

1045 For both sets, J -factor values are provided for all dSphs as a function of the radius of the
1046 integration region [53, 47, 55]. Table 5.1 shows the heliocentric distance and Galactic coordinates
1047 of the twenty dSphs, together with the two sets of J -factor values integrated up to the outermost
1048 observed star for \mathcal{GS} and the tidal radius for \mathcal{B} . Both J -factor sets were derived through a Jeans
1049 analysis based on the same kinematic data, except for Draco where the measurements of [63] have
1050 been adopted in the computation of the \mathcal{B} value. The computations for producing the \mathcal{GS} and \mathcal{B}

1051 samples differ in the choice of the DM density, velocity anisotropy, and light profiles, for which the
1052 set \mathcal{B} takes into account some sources of systematic uncertainties.

1053 Figure 5.16 and Figure 5.17 show the comparisons for the J -factor versus the angular radius
1054 for each of the 20 dSphs used in this study. The uncertainties provided by the authors are also
1055 indicated in the figures. For the \mathcal{GS} set, the computation stops at the angular radius corresponding
1056 to the outermost observed star, while for the \mathcal{B} set, the computation stops at the angular radius
1057 corresponding to the tidal radius.

1058 5.9 Discussion and Conclusions

1059 In this multi-instrument analysis, we have used observations of 20 dSphs from the gamma-ray
1060 telescopes Fermi-LAT, H.E.S.S., MAGIC, VERITAS, and HAWC to perform a collective DM
1061 search annihilation signals. The data were combined across sources and detectors to significantly
1062 increase the sensitivity of the search. We have observed no significant deviation from the null, no
1063 DM hypothesis, and so present our results in terms of upper limits on the annihilation cross-section
1064 for seven potential DM annihilation channels.

1065 Fermi-LAT brings the most stringent constraints for continuum channels below approximately
1066 1 TeV. The remaining detectors dominate at higher energies. Overall, for multi-TeV DM mass,
1067 the combined DM constraints from all five telescopes are 2-3 times stronger than any individual
1068 telescope for multi-TeV DM.

1069 Derived from observations of many dSphs, our results produce robust limits given the DM
1070 content of the dSphs is relatively well constrained. The obtained limits span the largest mass
1071 range of any WIMP DM search. Our combined analysis improves the sensitivity over previously
1072 published results from each detector which produces the most stringent limits on DM annihilation
1073 from dSphs. These results are based on deep exposures of the most promising known dSphs with
1074 the currently most sensitive gamma-ray instruments. Therefore, our results constitute a legacy of
1075 a generation of gamma-ray instruments on WIMP DM searches towards dSphs. Our results will
1076 remain the reference in the field until a new generation of more sensitive gamma-ray instruments
1077 begin operations, or until new dSphs with higher J -factors are discovered.

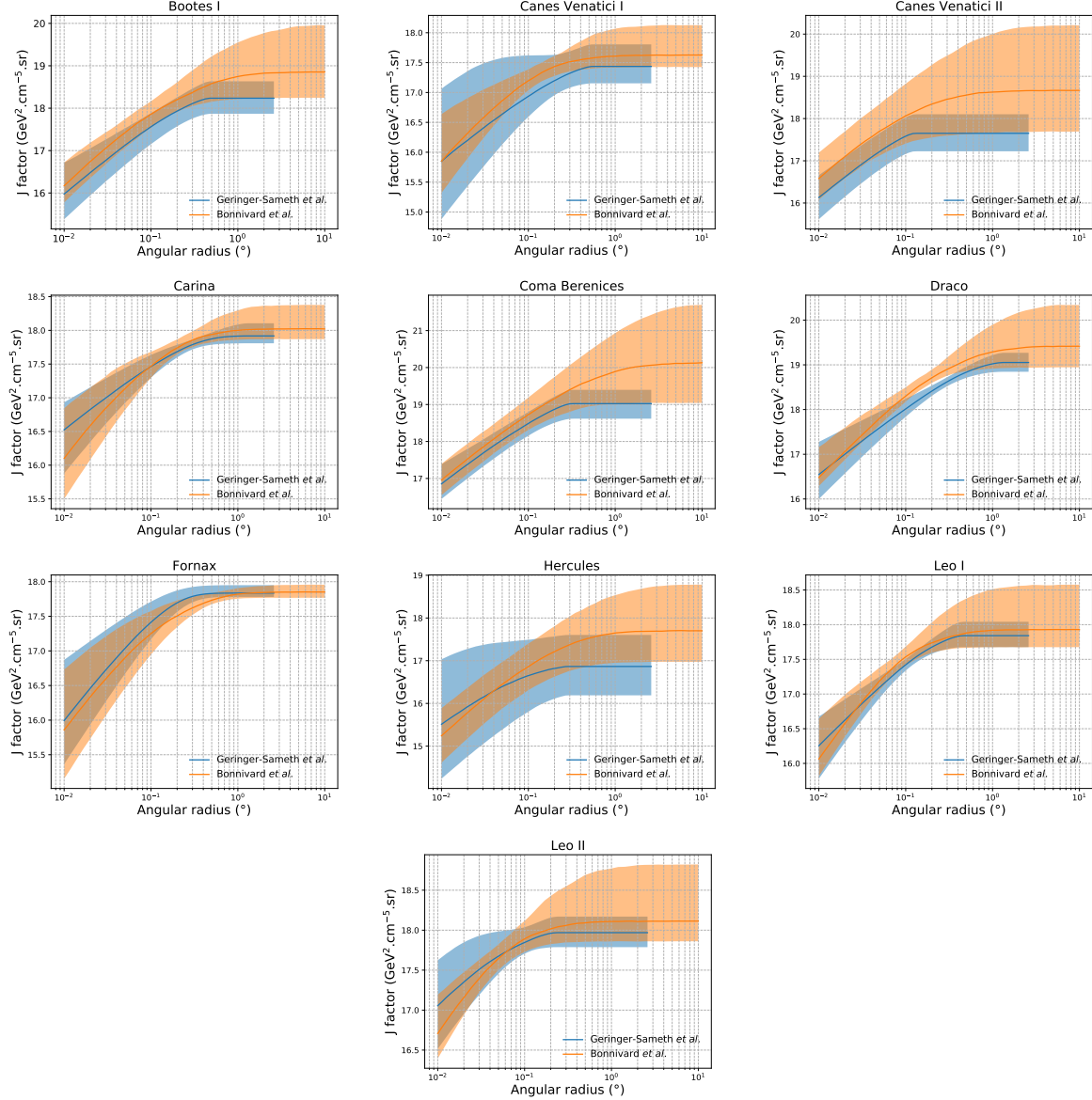


Figure 5.16 Comparisons between the J -factors versus the angular radius for the computation of J factors from Ref. [53] (\mathcal{GS} set in Table 5.1) in blue and for the computation from Ref. [47, 55] (\mathcal{B} set in Tab. 5.1) in orange. The solid lines represent the central value of the J -factors while the shaded regions correspond to the 1σ standard deviation.

This analysis serves as a proof of concept for future multi-instrument and multi-messenger combination analyses. With this collaborative effort, we have managed to sample over four orders in magnitude in gamma-ray energies with distinct observational techniques. Determining the nature of DM continues to be an elusive and difficult problem. Larger datasets with diverse measurement techniques could be essential to tackling the DM problem. A future collaboration using similar

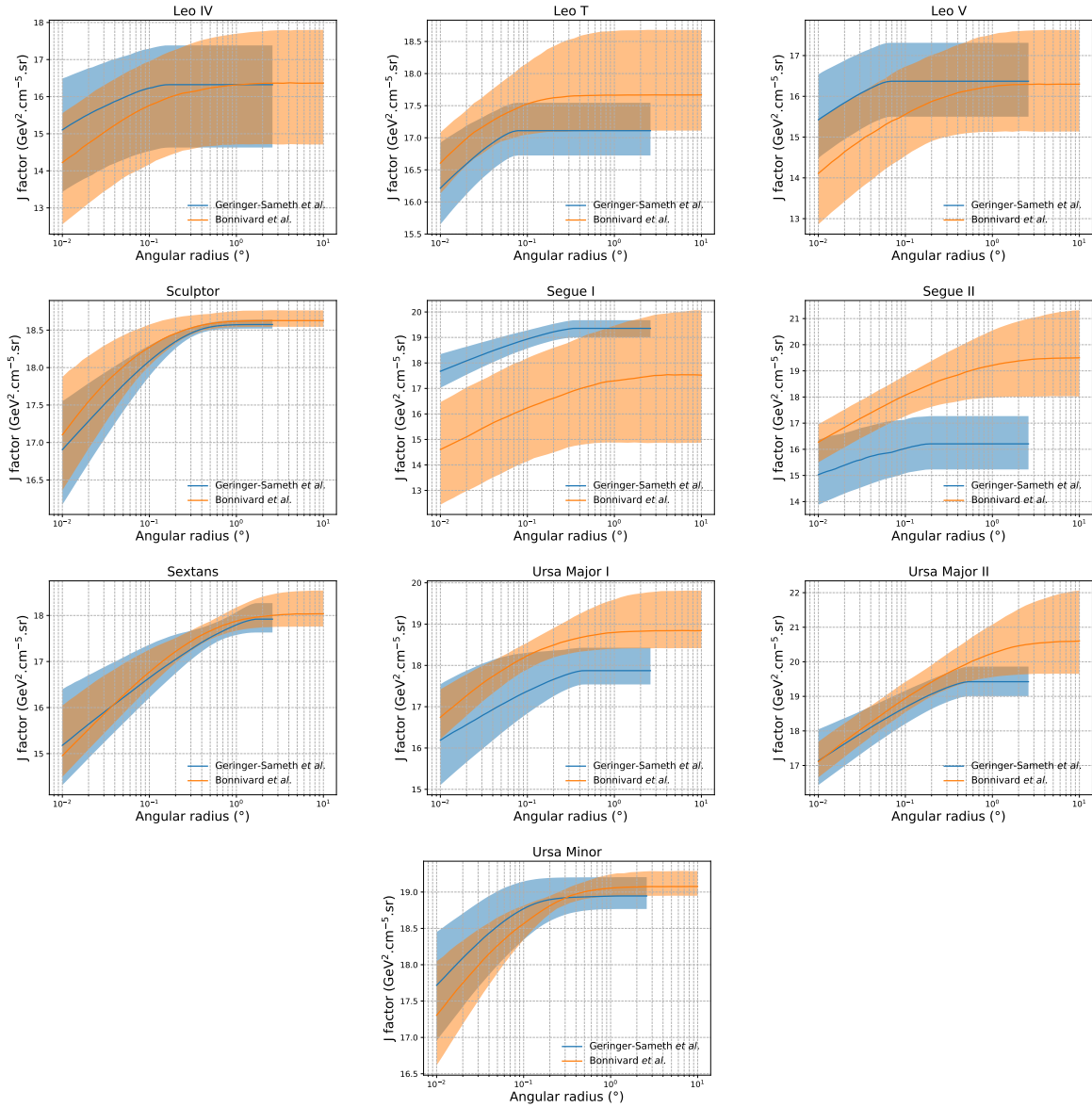


Figure 5.17 Comparisons between the J -factors versus the angular radius for the computation of J factors from Ref. [53] (\mathcal{GS} set in Tab. 5.1) in blue and for the computation from Ref. [47, 55] (\mathcal{B} set in Tab. 5.1) in orange. The solid lines represent the central value of the J -factors while the shaded regions correspond to the 1σ standard deviation.

1083 techniques as the ones described in this paper could grow even beyond gamma rays. The models we
 1084 used for this study include annihilation channels with neutrinos in the final state. Advanced studies
 1085 could aim to merge our results with those from neutrino observatories with large data sets. Efforts
 1086 are already underway to add data from the IceCube, ANTARES, and KM3NeT observatories to
 1087 these gamma-ray results.

1088 From this work, a selection of the best candidates for observations, according to the latest
1089 knowledge on stellar dynamics and modelling techniques for the derivation of the J -factors on
1090 the potential dSphs targets, is highly desirable at the time that new experiments are starting their
1091 dark matter programs using dSphs. Given the systematic uncertainty inherent to the derivation of
1092 the J -factors, an informed observational strategy would be to select both objects with the highest
1093 J -factors that could lead to DM signal detection, and objects with robust J -factor predictions, i.e.
1094 with kinematic measurements on many bright stars, which would strengthen the DM interpretation
1095 reliability of the observation outcome.

1096 This analysis combines data from multiple telescopes to produce strong constraints on astro-
1097 physical objects. From this perspective, these methods can be applied beyond just DM searches.
1098 Almost every astrophysical study can benefit from multi-telescope, multi-wavelength gamma-ray
1099 studies. We have enabled these telescopes to study the cosmos with greater precision and detail.
1100 Many astrophysical searches can benefit from multi-instrument gamma-ray studies, for which our
1101 analysis lays the foundation.

CHAPTER 6

MULTITHREADING HAWC ANALYSES FOR DARK MATTER SEARCHES

6.1 Introduction

HAWC's current software suite, plugins to 3ML, does not fully utilize computational advancements of recent decades. Said advancements include the proliferation of Graphical Processing Units (GPUs), and multithreading on multicore processors. The analysis described in chapter 5 took up to 3 months of human time waiting for the full gambit of data analysis and simulation of background to run. Additionally, with the addition of a 2D binning scheme, f_{hit} and NN, the time needed to compute expected to grow. Although excessive computing time was, in part, from an intense use of a shared computing cluster, it was evident that there was room for improvement.

In HAWC's next generation dSph DM search, I decided to develop codes that would utilize the multicore processors on modern high performance computing clusters. The results of this work are featured in this chapter and brought a human timing improvement to computation that scales as

$1/N$ where N is the number of threads.

6.2 Dataset and Background

This section enumerates the data and background methods used for HAWC's multithreaded study of dSphs. Section 6.2.1 and Section 6.2.2 are most useful for fellow HAWC collaborators looking to replicate a multithreaded dSph DM search.

6.2.1 Itemized HAWC files

- Detector Resolution: `refit-Pass5-Final-NN-detRes-zenith-dependent.root`
- Data Map: `Pass5-Final-NN-maptree-ch103-ch1349-zenith-dependent.root`
- Spectral Dictionary: `HDMspectra_dict_gamma.npy`

6.2.2 Software Tools and Development

This analysis was performed using HAL and 3ML [42, 43] in Python version 3. I built software in collaboration with Michael Martin and Letrell Harris to implement the *Dark Matter Spectra from*

1126 *the Electroweak to the Planck Scale* (HDM) [64] and dSphs spatial model from [65] for HAWC
1127 analysis. A NumPy dictionary of HDM was made for Py3. The corresponding Python3 file is
1128 `HDMspectra_dict_gamma.npy`. These files can also be used for decay channels and tools are
1129 provided in HDM’s [git repository](#) [64]. The analysis was performed using the Neural Network
1130 energy estimator for Pass 5.F. A description of this estimator was provided in chapter 3. **TODO:**
1131 **Define a subsection when it’s written**, and its key improvements are an improved energy estimation
1132 and improved sensitivities at higher zenith angles. All other software used for data analysis, DM
1133 profile generation, and job submission to SLURM are also kept in my sandbox in the [Dark Matter](#)
1134 [HAWC](#) project. The above repository also incorporates the model inputs used previously in Glory
1135 Duck, described in chapter 5

1136 **6.2.3 Data Set and Background Description**

1137 The HAWC data maps used for this analysis contain 2565 days of data between runs 2104 (**TODO: Day start**) and 7476 (**TODO: Day end**). They were generated from pass 5.f reconstruction.
1139 The analysis is performed using the NN energy estimator with bin list:

1140 B1C0Ea, B1C0Eb, B1C0Ec, B1C0Ed, B1C0Ee, B2C0Ea, B2C0Eb, B2C0Ec, B2C0Ed, B2C0Ee,
1141 B3C0Ea, B3C0Eb, B3C0Ec, B3C0Ed, B3C0Ee, B3C0Ef, B4C0Eb, B4C0Ec, B4C0Ed, B4C0Ee,
1142 B4C0Ef, B5C0Ec, B5C0Ed, B5C0Ee, B5C0Ef, B5C0Eg, B6C0Ed, B6C0Ee, B6C0Ef, B6C0Eg,
1143 B6C0Eh, B7C0Ee, B7C0Ef, B7C0Eg, B7C0Eh, B7C0Ei, B8C0Ee, B8C0Ef, B8C0Eg, B8C0Eh,
1144 B8C0Ei, B8C0Ej, B9C0Ef, B9C0Eg, B9C0Eh, B9C0Ei, B9C0Ej, B10C0Eg, B10C0Eh,
1145 B10C0Ei, B10C0Ej, B10C0Ek, B10C0El

1146 Bin 0 was excluded as it has substantial hadronic contamination and poor angular resolution.

1147 Background considerations and source selection was identical to Section 5.2, and no additional
1148 arguments are provided here. Many of the HAWC systematics explored in Section 5.7 also apply
1149 for this DM search and are not added upon here.

1150 **6.3 Analysis**

1151 The analysis and its systematics are almost identical to Section 5.3. Importantly, we use the
1152 same Equation (7.1) and Equation (5.2) for estimating the gamma-ray flux at HAWC from our
1153 sources. We add on to the previous study with a search for DM decay. The flux equations for DM
1154 decay are

$$\frac{d\Phi_\gamma}{dE_\gamma} = \frac{1}{4\pi\tau m_\chi} \frac{dN_\gamma}{dE_\gamma} \times \int_{\text{source}} d\Omega \int_{l.o.s} \rho_\chi dl(r, \theta') \quad (6.1)$$

1155 with a new quantity, the D factor, defined as

$$D = \int d\Omega \int_{l.o.s} dl \rho_\chi(r, \theta') \quad (6.2)$$

1156 Software was written to accommodate DM decay from dSphs, however decay profiles were not
1157 received from $\mathcal{L}\mathcal{S}$ by the time of writing this thesis.

1158 **6.3.1 $\frac{dN_\gamma}{dE_\gamma}$ - Particle Physics Component**

1159 For these spectra, we import HDM with Electroweak (EW) corrections and additional correc-
1160 tions for neutrinos above the EW scale [64]. The spectrum is implemented as a model script in
1161 astromodels for 3ML. A comprehensive description of EW corrections and neutrino considerations
1162 are provided later in [TODO: refeance MM nu duck](#).

1163 Figure 6.1 demonstrates the impact of changes from HDM on DM annihilation to W bosons.
1164 A class in astromodels was developed to include HDM and is aptly named `HDMspectra` within
1165 `DM_models.py`. The SM DM annihilation channels studied here are $\chi\chi \rightarrow:$

1166 e^+e^- , $\mu^+\mu^-$, $\tau^+\tau^-$, $b\bar{b}$, $t\bar{t}$, gg , W^+W^- , ZZ , $c\bar{c}$, $u\bar{u}$, $d\bar{d}$, $s\bar{s}$, $\nu_e\bar{\nu}_e$, $\nu_\mu\bar{\nu}_\mu$, $\nu_\tau\bar{\nu}_\tau$, $\gamma\gamma$, hh .

1167 For $\gamma\gamma$ and ZZ , a substantial fraction of the signal photons are expected to have total energy equal
1168 to m_χ [64]. This introduces a δ -function that is much narrower than the energy resolution of the
1169 HAWC detector. To ensure that this feature is not lost in the likelihood fits, the 'line' feature is
1170 convolved with a Gaussian kernel with a 1σ width of $0.05 \cdot m_\chi$ and total kernel window of $\pm 4\sigma$.
1171 This differs from HAWC's previous line study where 30% of HAWC's energy resolution was used
1172 for the kernel [66]. The NN energy estimator's strength compared to f_{hit} at low gamma-ray energy

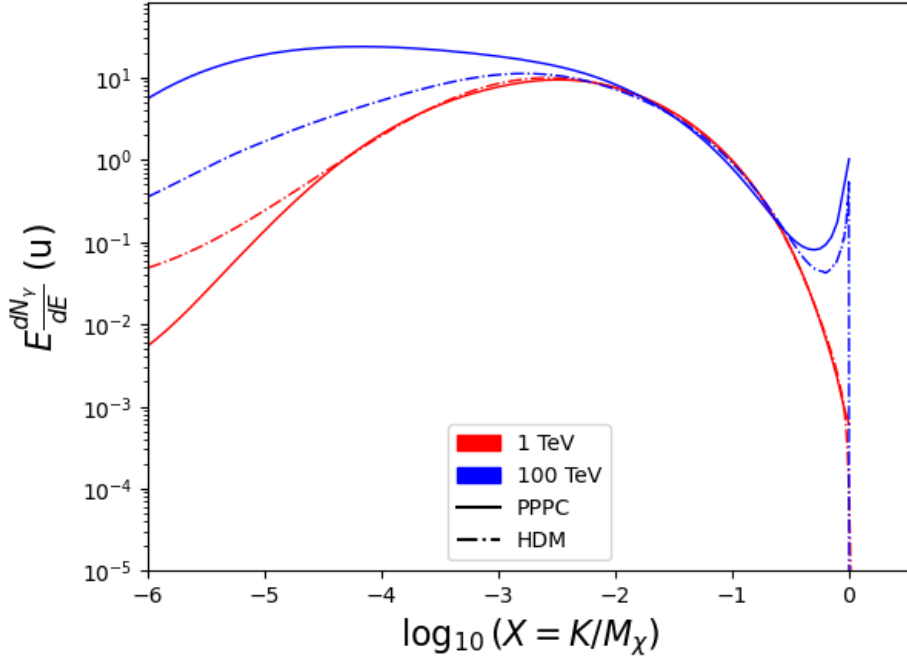


Figure 6.1 Difference between spectral hypotheses from PPPC [44] and HDM [64]. Shown is the expected DM annihilation spectrum for $\chi\chi \rightarrow W^-W^+$. Solid lines are spectral models with EW corrections from the PPPC. Dash-dot lines are spectral models from HDM. Red lines are models for $M_\chi = 1$ TeV. Blue lines represent models for $M_\chi = 100$ TeV.

enables smaller resolutions in addition to low energy tails in the spectral models [64]. $\chi\chi \rightarrow \gamma\gamma$ and ZZ spectral hypotheses are shown in Figure 6.2. Spectral models for the remaining annihilation channels are plotted for each m_χ in Figure B.1.

6.3.2 J and D - Astrophysical Components

The J-factor profiles for each source are imported from Louis Strigari et al. (referred to with \mathcal{LS}) [65]. Profiles in $\frac{dJ}{d\Omega}(\theta)$ up to $\theta = 0.5^\circ$ were provided directly from the authors. Map generation from these profiles were almost identical to Section 5.3.2 except that a higher order trapezoidal integral was used for the normalization of the square, uniformly-spaced map:

$$p^2 \cdot \sum_{i=0}^N \sum_{j=0}^M w_{i,j} \frac{d\mathcal{K}}{d\Omega}(\theta_{i,j}, \phi_{i,j}) \quad (6.3)$$

\mathcal{K} is either J or D for the spatial distributions of annihilation or decay respectively. p is the angular side of one pixel in the map. $w_{i,j}$ is a weight assigned the following ways:

$w_{i,j} = 1$ if $(\theta_{i,j}, \phi_{i,j})$ is fully within the region of integration

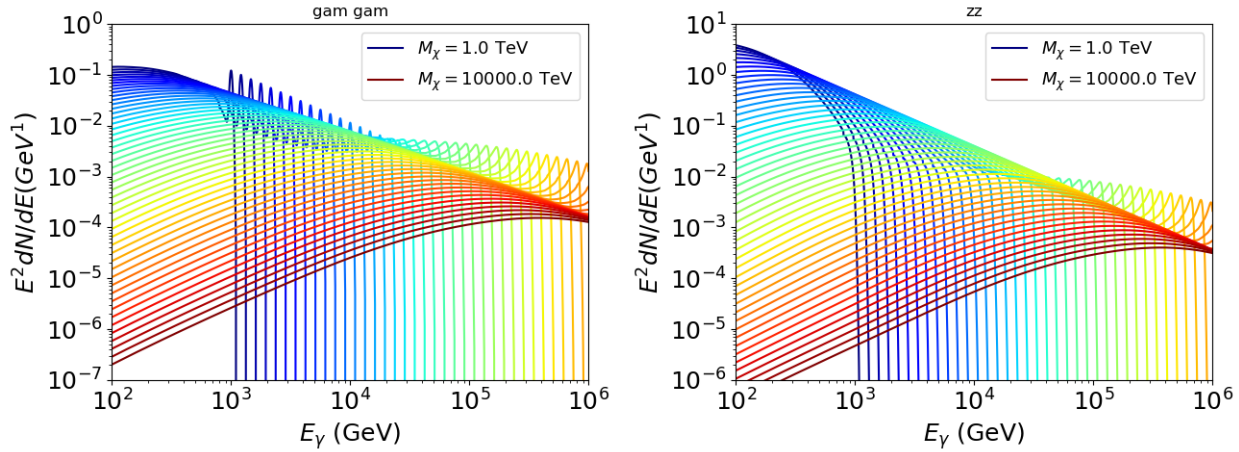


Figure 6.2 Photon spectra for $\chi\chi \rightarrow \gamma\gamma$ (left) and $\chi\chi \rightarrow ZZ$ (right) after Gaussian convolution of line features. Both spectra have δ -features at photon energies equal to the DM mass. Bluer lines are annihilation spectra with lower DM mass. Redder lines are spectra from larger DM mass. All Spectral models are sourced from the Heavy Dark Matter models [64]. Axes are drawn roughly according to the energy sensitivity of HAWC.

1184 $w_{i,j} = 1/2$ if $(\theta_{i,j}, \phi_{i,j})$ is on an edge of the region of integration

1185 $w_{i,j} = 1/4$ if $(\theta_{i,j}, \phi_{i,j})$ is on a corner of the region of integration

1186 Figure 6.3 shows the median and $\pm 1\sigma$ maps used as input for DM annihilation studied by \mathcal{LS} .

1187 **6.3.3 Source Selection and Annihilation Channels**

1188 HAWC's sources for this multithreaded analysis include Coma Berenices, Draco, Segue 1, and
 1189 Sextans \mathcal{LS} observes up to 43 sources in its publication, however only 4 of the best fit profiles were
 1190 provided at the time this thesis was written. A full description of each source used in this analysis
 1191 is found in Table 6.1.

1192 This analysis improves on chapter 5 in the following ways. Previously, the particle physics
 1193 model used for gamma-ray spectra from DM annihilation was from the PPPC [44] which missed
 1194 important considerations relevant for the neutrino sector. HDM is used to account for this shortfall
 1195 [64]. HDM also models DM to the Planck scale which permits HAWC to probe PeV scale DM.
 1196 For this study, we sample DM masses: 1 TeV - 10 PeV with 6 mass bins per decade in DM mass.
 1197 In the case of line spectra ($\chi\chi \rightarrow \gamma\gamma$, or ZZ), we double the mass binning to 12 DM mass bins
 1198 per decade in DM mass. A larger source catalog is used that uses a Navarro–Frenk–White (NFW)

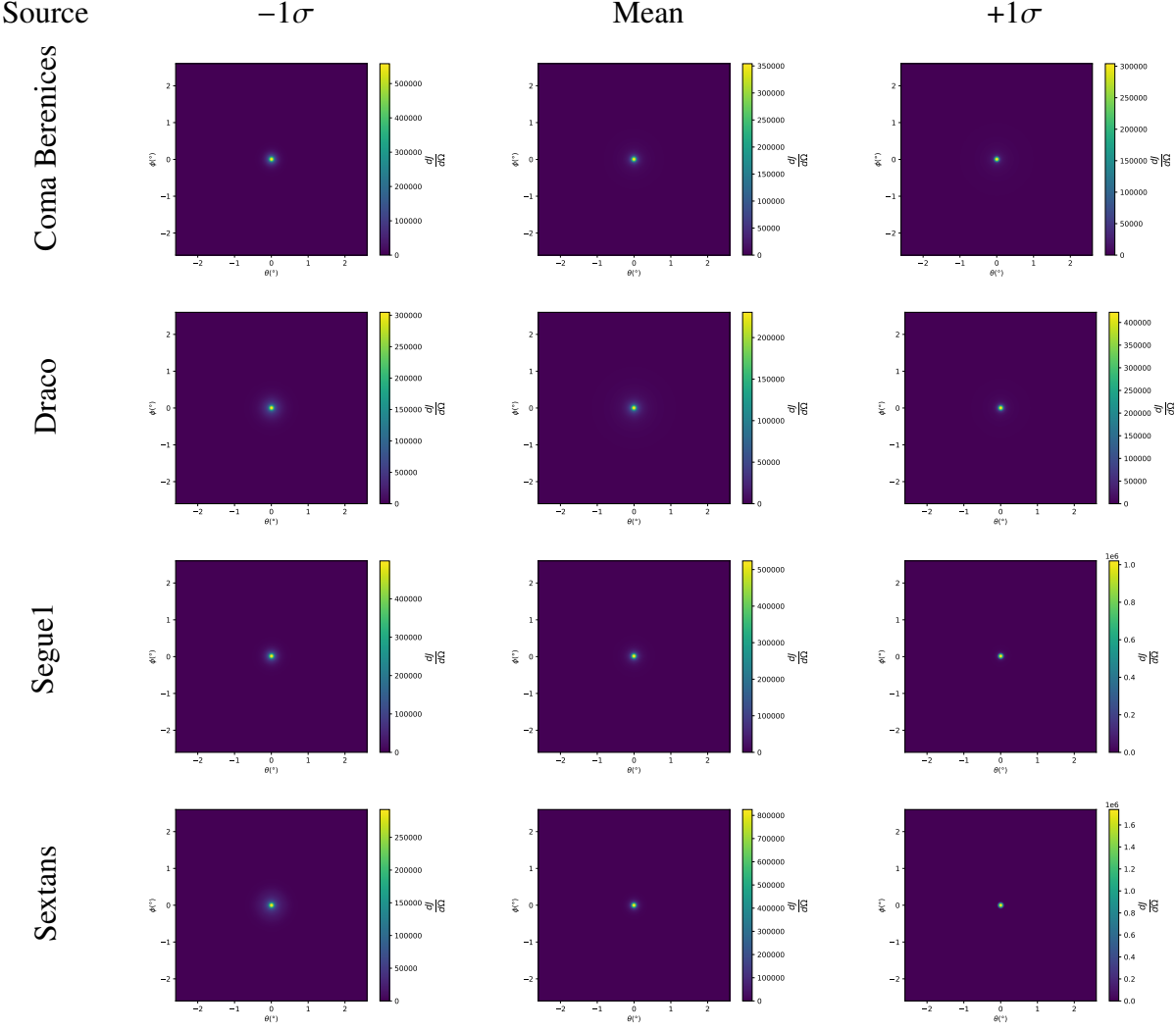


Figure 6.3 $\frac{dJ}{d\Omega}$ maps for Coma Berenices, Draco, Segue1, and Sextans. Columns are divided for the $\pm 1\sigma$ uncertainties in $dJ/d\Omega$ around the mean value from \mathcal{LS} [65]. Origin is centered on the specific dwarf spheroidal galaxies (dSph). θ and ϕ axes are the angular separation from the center of the dwarf

1199 spatial DM distribution from \mathcal{LS} [65]. Because NFW has fewer parameters than what is used
 1200 for \mathcal{GS} , \mathcal{LS} is able to fit ultra-faint dwarves, expanding the number of sources available for DM
 1201 searches. Finally, the gamma-ray ray dataset is much larger. The study performed here analyzes
 1202 2565 days of data compared to 1017 days analyzed in chapter 5.

1203 6.4 Likelihood Methods

1204 These are identical to Section 5.4.1 and no additional changes are made to the likelihood. Bins
 1205 in this analysis are expanded to include HAWC’s NN energy estimator.

1206 **6.5 Computational Methods: Multithreading**

1207 Previously, as in Section 5.3, the likelihood was minimized for one model at a time. One
 1208 model in this case representing a DM annihilation channel, DM mass, and dSph. In an effort
 1209 to conserve human and CPU time, jobs submitted for high performance computing contained a
 1210 list of DM masses to iterate over for likelihood fitting. Jobs were then trivially parallelized for
 1211 each permutation of the two lists: CHANS (SM annihilation channel) and SOURCES (dSph spatial
 1212 templates). The lists for CHANS and SOURCES are found in Section 6.3.1 and Table 6.1, respectively.
 1213 Initially, 11 DM mass bins were serially sampled for one job defined by a [SM channel, dSph] set.
 1214 Computing the likelihoods would take between 1.5 to 2 hrs, stochastically, for a job. We expect to
 1215 compute likelihoods for data and 300 Poisson background trials. The estimated CPU time based on
 1216 the above for all SM annihilation channels (17) and 25 sources (all \mathcal{LS} sources within HAWC's
 1217 field of view) amounted to 127,925 jobs. In total, 1,407,175 likelihood fits and profiles would
 1218 be computed for the 11 mass bins we wished to study. The estimated CPU time ranged between
 1219 10k CPU days - 8k CPU days. Human time is more challenging to estimate as job allocation is
 1220 stochastic and highly dependent on what other users are submitting, yet it is unlikely that all jobs
 1221 would run simultaneously. Therefore, we can expect human time to be about as long as was seen
 1222 in chapter 5 which was on the order of months to fully compute on a smaller analysis. A visual aid
 1223 to describe how jobs were organized is provided in Figure 6.4.

Name	Distance (kpc)	l, b ($^{\circ}$)	$\log_{10} J$ (\mathcal{LS} set) $\log_{10}(\text{GeV}^2 \text{cm}^{-5} \text{sr})$
Coma Berenices	44	241.89, 83.61	$19.00^{+0.36}_{-0.35}$
Draco	76	86.37, 34.72	$18.83^{+0.12}_{-0.12}$
Segue I	23	220.48, 50.43	$19.12^{+0.49}_{-0.58}$
Sextans	86	243.50, 42.27	$17.73^{+0.13}_{-0.12}$

Table 6.1 Summary of the relevant properties of the dSphs used in the present work. Column 1 lists the dSphs. Columns 2 and 3 present their heliocentric distance and galactic coordinates, respectively. Column 4 reports the J -factors of each source given from the \mathcal{LS} studies and estimated $\pm 1\sigma$ uncertainties. The values $\log_{10} J$ (\mathcal{LS} set) [65] correspond to the mean J -factor values for a source extension truncated at 0.5° .

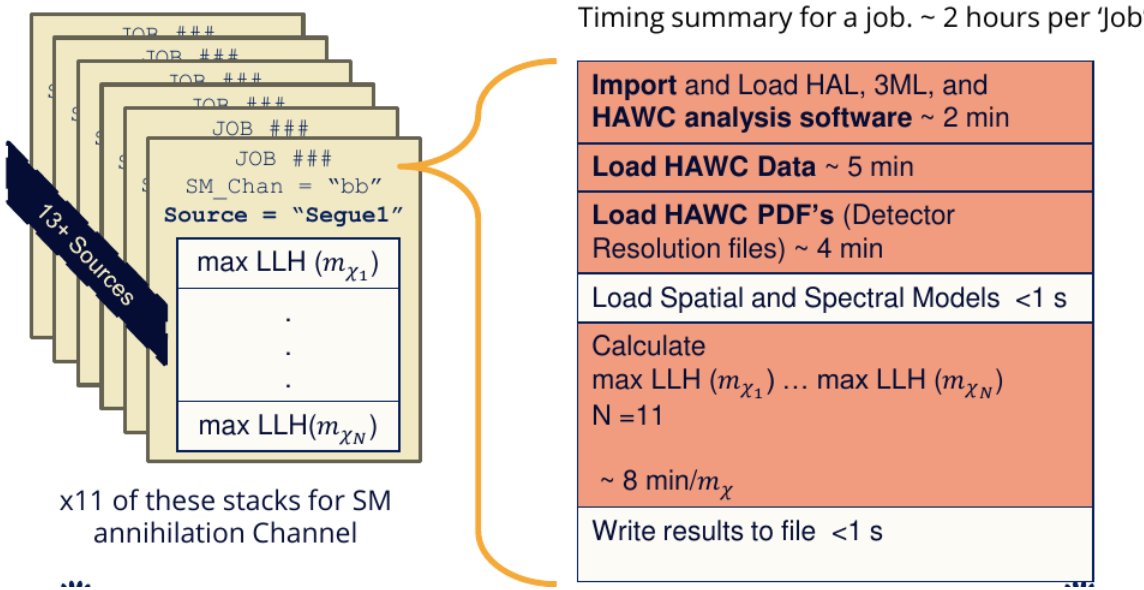


Figure 6.4 Infographic on how jobs and DM computation was organized in Section 5.3. Jobs were built for each permutation of CHANS and SOURCES shown by the left block in the figure. Each job, which took on the order 2 hrs to compute, had the following work flow: 1. Import HAWC analysis software, 2 min to run. 2. Load HAWC count maps, 5 min to run. 3. Load HAWC energy and spatial resolutions, 4 min. 5. Load DM spatial source templates and spectral models, less than 1 s. 6. Perform likelihood fit on data and model, about 8 min per DM mass. 7. Write results to file, less than 1s.

1224 The computational needs for this next generation DM analysis are extreme and is unlike other
 1225 analyses performed on HAWC. It became clear that there was a lot to gain from optimizing how
 1226 the likelihoods are computed. This section discusses how multi-threading was applied to solve and
 1227 reduce HAWC’s computing of likelihoods for large parameter spaces like in DM searches.

1228 6.5.1 Relevant Foundational Information

1229 The profiling of the likelihood for HAWC is done via gradient descent where the normalization
 1230 of Equation (7.1) (linearly correlated with $\langle \sigma v \rangle$) is rescaled in the descent. Additionally, we sample
 1231 the likelihood space for a defined list of $\langle \sigma v \rangle$ ’s described in Section 5.4.2. The time to compute
 1232 these values is not predictable or consistent because many variables can change across the full
 1233 model-space. Comprehensively, these variables are:

- 1234 • m_χ : DM rest mass
- 1235 • CHAN : DM SM annihilation channel.

1236 • SOURCE : dSph within HAWC's field of view. This involves a spatial template AND coordinate
1237 in HAWC data.

1238 • $\langle\sigma v\rangle$: Effectively the flux normalization and free parameter in the likelihood fit.

1239 Therefore, we develop an asynchronous, functional-parallel coding pattern. Asynchronous mean-
1240 ing that the instructions and computing within a function are independent and permitted to be out
1241 of sync with sibling computations. Functional-parallel meaning that instructions are the subject of
1242 parallelization rather than threading the likelihood computation. This is close to trivial parametriza-
1243 tion seen in Figure 6.4 except that we seek to consolidate the loading stages (software, data, and
1244 detector resolution loading). Reducing the total instances of loading stages and distributing access
1245 to the reduced loads across multiple asynchronous threads is expected to reduce serial processing
1246 time and the overhead implicit to each job in addition to saving human time.

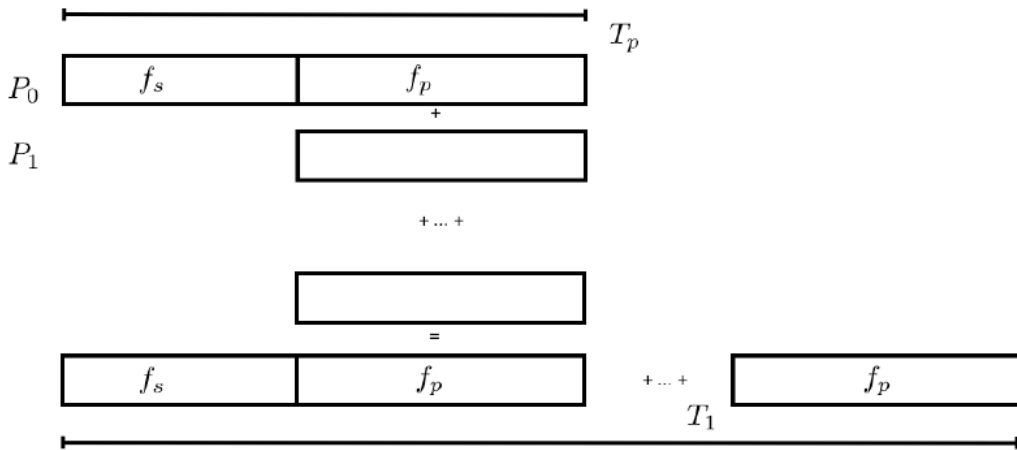


Figure 6.5 Graphic of Gustafson parallel coding pattern. f_s is the fraction of a program, in time, spent on serial computation. f_p is the fraction of computing time that is parallelizable. T_p is the total time for a parallel program to run. T_1 is the total time for a parallel program to run if only 1 processor is allocated. P_N is the N -th processor where it's row is the computation the processor performs. The Gustafson pattern is most similar to what is implemented for this analysis. Figure is pulled from [67].

1247 We need a way to measure and compare the expected speedup and efficiency gain for this
1248 asynchronous coding pattern. I pull inspiration for timing measurement from [67] and use *Amdahl's
1249 law with hybrid programming*. Hybrid programming meaning that the computation is a mix of

1250 distributed and shared memory programming. If we assume the code is fully parallelizable over p
1251 processors and c threads, the ideal speedup is simply pc and ideal run-time is $T_1/(pc)$. T_1 is the
1252 total time for a parallel program to run if only 1 processor is allocated. However, the coding pattern
1253 contains some amount of unavoidable serial computation, as shown in Figure 6.5. In our case, the
1254 run time is estimated to be

$$T_{p,c} = \frac{T_1}{pc} (1 + F_s(c - 1)). \quad (6.4)$$

1255 F_s is the fraction of CPU time dedicated to serial computation. The expected speedup is

$$S_{p,c} \equiv \frac{T_1}{T_{p,c}} = \frac{pc}{1 + F_s(c - 1)}. \quad (6.5)$$

1256 From Equation (6.5), we can see that the speed-up scales with p/F_s . We are free to minimize
1257 F_s asymptotically by enlarging the total models that are submitted to the thread pool, thereby
1258 shrinking the CPU fraction dedicated to serial operation. We are also free to define exactly how
1259 many threads and processors we utilize, yet eventually hit a hard cap at the hardware available on
1260 our computing cluster. HAWC uses Intel Xeon processors with 48 cores and 96 threads. This
1261 means when N-threads (c) are defined, $N \bmod 2$ cores (p) are needed. We see that a successful
1262 code scales well as the expected speedup is inversely correlated with F_s . As the total number of
1263 models sampled grows, the speedup will also.

1264 6.5.2 Implementation

1265 The multithreaded code was written in Python3 and is documented in the `dark_matter_hawc`
1266 [repository](#) within the script named `mpu_analysis.py`. A version of the script as of April 25
1267 **TODO: make sure to update on this date** is also provided in Section B.2 It has many dependencies
1268 including the HAWC analysis software. Figure 6.6 displays the workflow of a job with 3 threads.
1269 Within a job, SOURCE is kept fixed . CHAN(S) remains 17 elements long. More m_χ are sampled
1270 from 11 bins up to 49 (for $\gamma\gamma$ and ZZ) and 25 (for remaining CHANS) which amounts to 12 or 6
1271 mass bins per decade. The DM mass, m_χ , and SM annihilation channels, CHANS, are permuted into
1272 a 473 element list which is split evenly across N threads where N ranges between 5 - 16. Within a
1273 thread, for each m_χ -CHAN tuple, 1001 $\langle\sigma v\rangle$ values are sampled in the likelihood, and the value of

Timing summary for a multi-threaded job.

Import and Load HAL, 3ML, and HAWC analysis software ~ 2 min		
Load HAWC Data ~ 5 min		
Load HAWC PDF's (Detector Resolution files) ~ 4 min		
Load Spatial Model < 1s		
Load Spectra Models <1 s	Load Spectra Models <1 s	Load Spectra Models <1 s
Calculate max LLH (Chan_0, m_{χ_1}) ... max LLH (Chan_?, m_{χ_N}) N = TOTAL/N_THREADS ~ 8 min/Spec_model	Calculate max LLH (Chan_?, m_{χ_1}) ... max LLH (Chan_?, m_{χ_N}) N = TOTAL/N_THREADS ~ 8 min/Spec_model	Calculate max LLH (Chan_?, m_{χ_1}) ... max LLH (Chan_?, m_{χ_N}) N = TOTAL/N_THREADS ~ 8 min/Spec_model
Write results to file <1 s	Write results to file <1 s	Write results to file <1 s
Join Threads and terminate < 1s		

Figure 6.6 Task chart for one multithreaded job developed for this project. Green blocks indicate a shared resource across the threads AND computation performed serially. Red blocks indicate functional parallel processing within each thread. 3 threads are represented here, yet many more can be employed during the full analysis. Jobs are defined by the SOURCE as these require unique maps to be loaded into the likelihood estimator. The m_{χ} , CHAN, and $\langle \sigma v \rangle$ variables are entered into the thread pool and allocated as evenly as possible across the threads.

1274 $\langle \sigma v \rangle$ that maximizes the likelihood is found. Although rare, fits that failed are handled on a case
1275 by case basis.

1276 6.5.3 Performance

M Tasks	$T_{p,c}$ (hr:min:s)			
	$T_{1,1}$	$T_{1,2}$	$T_{1,8}$	$T_{1,16}$
50	1:40:37.5	0:52:43.7	0:19:13.8	0:13:44.0
74	2:22:30.0	1:15:00.6	0:25:21.3	0:15:49.8
100	(3:07:51.9)	1:40:10.5	0:30:44.4	0:20:01.4
200	(6:02:20.6)	-	1:00:32.0	0:30:35.0
473	(13:58:40.3)	-	TODO: run this	1:07:53.2

Table 6.2 Timing summaries for analyses for serial and multithreaded processes. M tasks is the number of functional-parallel tasks ran for the computation. $T_{p,c}$ is a single run time in hours:minutes:seconds for runs utilizing p nodes and c threads. Runs are run interactively on the same computer to maximize consistency. Empty entries are indicated with '-'. (·) entries are estimated entries extrapolated from data earlier in the column.

1277 We see a tremendous reduction to human time waiting for our dSph analyses to run. Table 6.2

1278 shows the timing summaries for analyses of different sizes and thread counts. Additionally, the
 1279 efficiency gained when consolidating the serial loading of data is also apparent in our ability to
 1280 study many more tasks in about the same amount of wall time as a smaller serial computation. Trials
 1281 represented in the table were run on an AMD Opteron® processor 6344 with 48 cores, 2 threads
 1282 per core; 2.6 GHz clock. This is not the same architecture used for analysis on the computing
 1283 cluster however they are similar enough that results shown here are reasonably representative of
 1284 computing on the HAWC computing cluster. I use the Tab. 6.2 for the inferences and conclusions
 1285 in the following paragraphs.

1286 First, we want to find T_s , the time of serial computation. From Fig. 6.5, the timing for our
 1287 coding pattern can be written as

$$T_s + Mt_p = T_{1,1}^M. \quad (6.6)$$

1288 M is the number of functional-parallel tasks (represented as column 1 of Tab. 6.2), and t_p is the
 1289 average time to complete a single parallel task. $T_{1,1}^M$ is the total time for a parallel program to run if
 1290 only 1 processor is allocated for M parallel task. With two runs of different M ($M1$ and $M2$), we
 1291 can use a system of equations to derive

$$T_s = T_{1,1}^{M1} - M1 \left(\frac{T_{1,1}^{M1} - T_{1,1}^{M2}}{M1 - M2} \right). \quad (6.7)$$

1292 We also extract t_p using the same methods:

$$t_p = \frac{T_{1,1}^{M1} - T_{1,1}^{M2}}{M1 - M2}. \quad (6.8)$$

1293 From Tab. 6.2, we set $M1 = 50$ and $M2 = 74$ and take their corresponding $T_{1,1}$ from the table to
 1294 calculate T_s and t_p .

$$T_s = 803.1\text{s} \text{ and } t_p = 104.6\text{s} \quad (6.9)$$

1295 Now, we have specific estimation for the fraction of serial computing time, F_s :

$$F_s = \frac{803.1}{803.1 + 104.6 \cdot M}. \quad (6.10)$$

1296 The maximum M for this study is 473 which evaluates using Eq. (6.10): $F_s = 0.016$ or 1.6% of
 1297 computing time. Table 6.3 shows the resulting speedups.

M Tasks	F_s	$S_{1,2}$	$S_{1,8}$	$S_{1,16}$
50	1.33 E-1	1.90 [1.76]	5.23 [4.14]	6.35 [5.34]
74	9.40 E-2	1.90 [1.83]	5.62 [4.82]	9.00 [6.64]
100	7.13 E-2	1.88 [1.87]	6.11 [5.34]	9.38 [7.73]
200	3.70 E-2	- [1.93]	5.98 [6.36]	11.85 [10.29]
473	1.60 E-2	- [1.97]	[7.20]	12.35 [12.91]

Table 6.3 Speed up summaries for analyses for serial and multithreaded processes. M tasks is the number of functional-parallel tasks ran for the computation. $S_{p,c}$ is a single speedup comparison for runs utilizing p nodes and c threads. [·] are the estimated speedups calculated from Tab. 6.2, Eq. (6.10), and Eq. (6.5). Empty entries are indicated with '-'.

1298 We see a speedup that generally exceeds expectations from Eq. (6.5) for real trail runs. We also
 1299 see that there are diminishing returns as the number of threads increases. For small jobs with large c ,
 1300 both the expected and observed speedup are significantly smaller than c . One thing not considered
 1301 in Eq. (6.5) is the time incurred via communication latency. Communication latency increases
 1302 with the number of threads and contributes to diminishing returns. Additionally, these values are
 1303 for single runs and do not consider the stochastic variation expected in a shared high performance
 1304 computing resource. Therefor, these results are not strictly conclusive, yet demonstrate the merits
 1305 of multi-threading. We see very clearly that there is a lot to gain, and this new coding pattern will
 1306 expand HAWC's analysis capabilities.

1307 6.6 Analysis Results

1308 3 of the 43 \mathcal{LS} dSphs considered for the multithreaded analysis. These dSph are analyzed for
 1309 emission from DM annihilation according to the likelihood method described in Section 5.4. The 3
 1310 likelihood profiles are then stacked to synthesize a combined limit on the dark matter cross-section,
 1311 $\langle\sigma v\rangle$. This combination is done for the 17 SM annihilation channels. Figure 6.7 and Fig. 6.8 show
 1312 the combined limits for all annihilation channels with HAWC's observations. Test statistics of the
 1313 best fit $\langle\sigma v\rangle$ values for each DM mass and SM annihilation channels are shown in Fig. 6.9 and
 1314 Fig. 6.10. We also compare these limits to HAWC's Glory Duck limits shown in Section 5.5. The
 1315 comparison to Glory Duck are featured in Fig. 6.11 for all the DM annihilation channels studied
 1316 for Glory Duck. A full comparison is provided in the appendix in Fig. B.2, Fig. B.3, and Fig. B.4.
 1317 Here, we show updated limits for $\chi\chi \rightarrow b\bar{b}, e\bar{e}, \mu\bar{\mu}, \tau\bar{\tau}, t\bar{t}, W^+W^-$, $\gamma\gamma$ and ZZ . For the first time

ever, we show limits for $\chi\chi \rightarrow c\bar{c}$, $s\bar{s}$, $u\bar{u}$, $d\bar{d}$, $\nu_e\bar{\nu}_e$, $\nu_\mu\bar{\nu}_\mu$, $\nu_\tau\bar{\nu}_\tau$, gg , and hh .

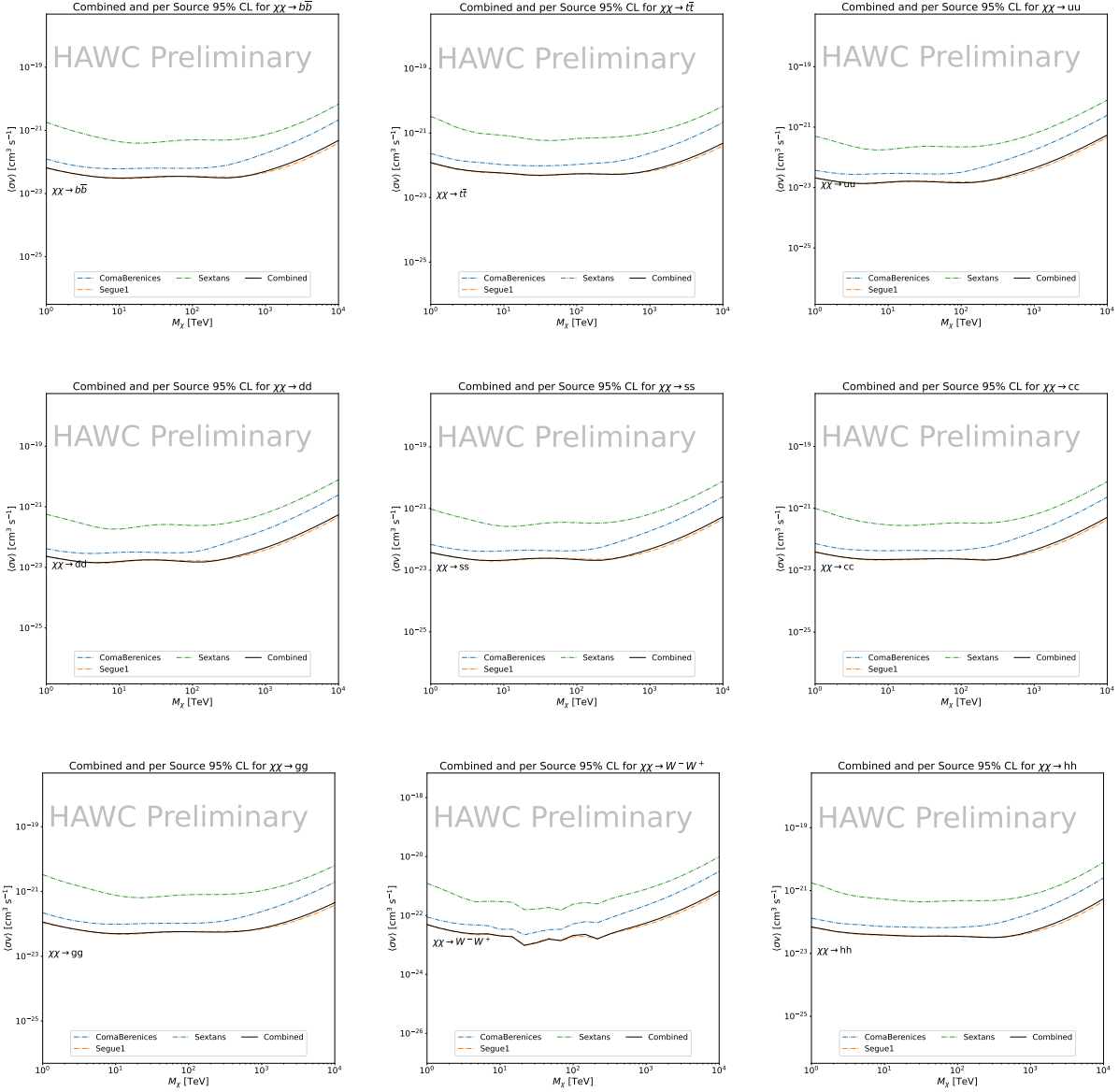


Figure 6.7 HAWC upper limits at 95% confidence level on $\langle\sigma v\rangle$ versus DM mass for $\chi\chi \rightarrow b\bar{b}$, $t\bar{t}$, $u\bar{u}$, $d\bar{d}$, $s\bar{s}$, $c\bar{c}$, gg , W^+W^- , and hh . Limits are with \mathcal{LS} J -factors [65]. The solid line represents the observed combined limit. Dashed lines represent limits from individual dSphs.

No DM was found in HAWC observations. The largest excess found in HAWC data was for DM annihilating to W -bosons for $m_\chi = 10\text{TeV}$ at 2σ . HAWC's limits and excesses are dominated by Segue1. Coma Berenices shows excess at higher DM mass, yet no similar excesses were observed in Segue1. Sextans did not contribute significantly to signal excess or the combined limit as it is

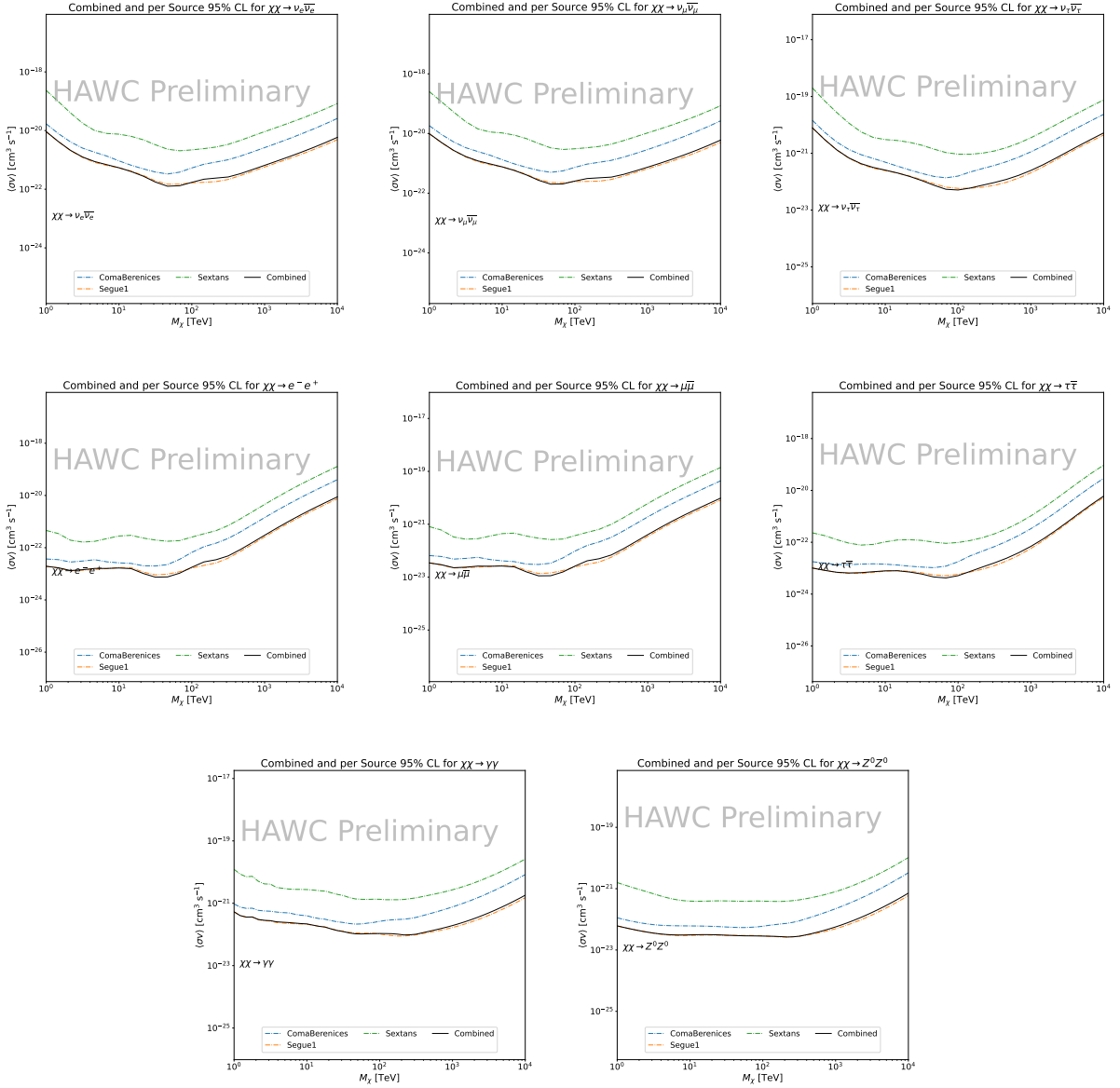


Figure 6.8 HAWC upper limits at 95% confidence level on $\langle\sigma v\rangle$ versus DM mass for $\chi\chi \rightarrow \nu_e \bar{\nu}_e$, $\nu_\mu \bar{\nu}_\mu$, $\nu_\tau \bar{\nu}_\tau$, $e^- e^+$, $\mu \bar{\mu}$, $\tau \bar{\tau}$, $\gamma \gamma$ and ZZ . Limits use $\mathcal{L}S J$ factors [65]. The solid line represents the observed combined limit. Dashed lines represent limits from individual dSphs.

at high zenith. Draco was not included as the PDF of some of our analysis bins were wider than what is reasonable for a point source analysis. Draco is at a high zenith for HAWC, so the effort required to include it was not justified by the benefits.

We were not able to generate background trials in time of writing this thesis. These are not shown and are an immediate next step for this analysis before publication.

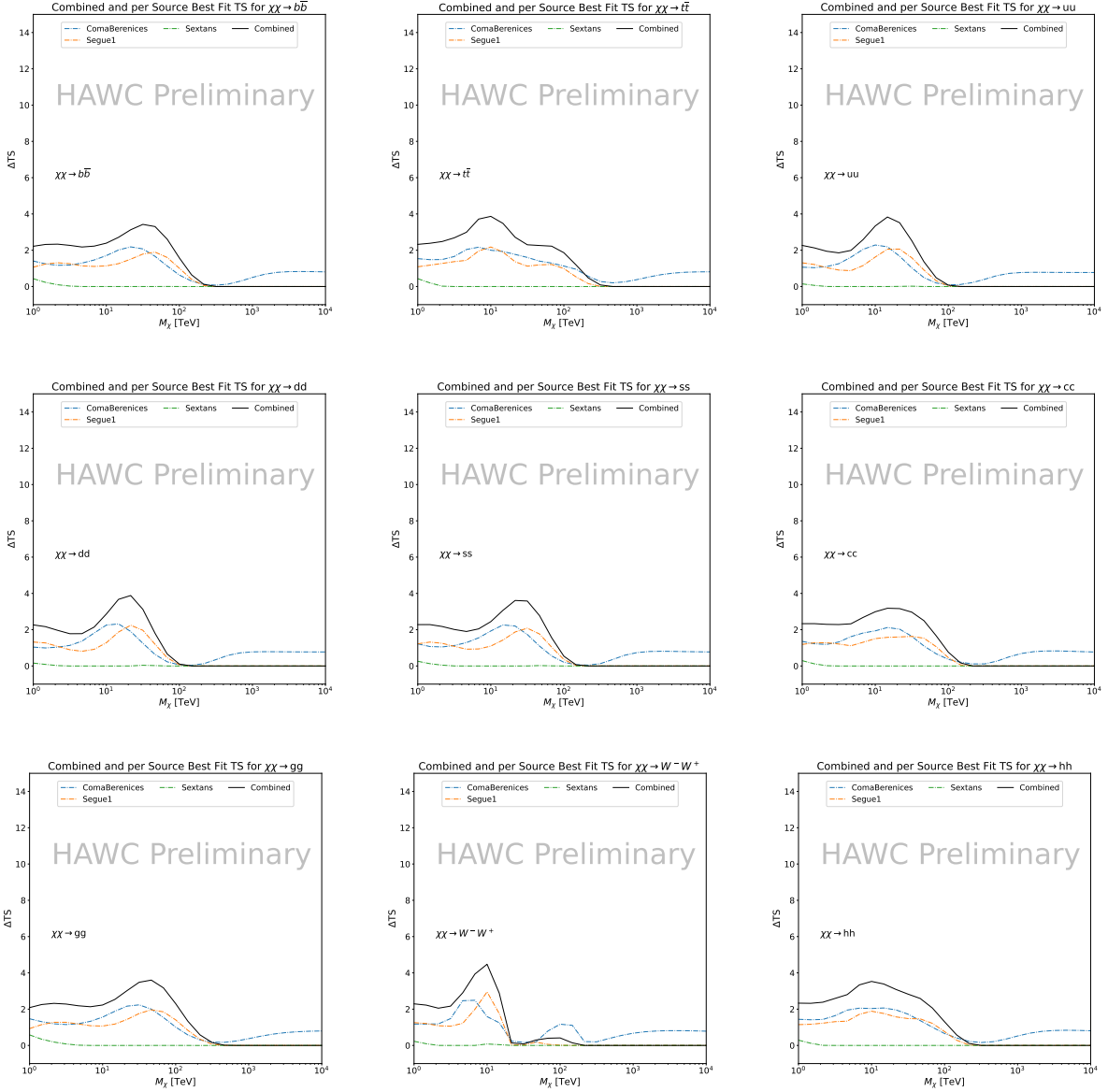


Figure 6.9 HAWC TS values for best fit $\langle\sigma v\rangle$ versus m_χ for SM annihilation channels: $\chi\chi \rightarrow b\bar{b}$, $t\bar{t}$, $u\bar{u}$, $d\bar{d}$, $s\bar{s}$, $c\bar{c}$, gg , W^-W^+ , and hh . Limits use $\mathcal{L}\mathcal{S} J$ factors. The solid black line shows the combined best fit TS values. The colored, dashed lines are the TS values from each dSph.

When comparing these results to Section 5.5, we see an overall decrease to the confidence limit therefore improvement to HAWC's expected sensitivity. This improvement is generally stronger than a doubling of data, or a factor $\sqrt{2}$ decrease. The comparison is somewhat complex and dependent on the dSph and SM annihilation channel. Figure 6.11 shows the comparisons of limits calculated for this analysis and Glory Duck (Section 5.5). Segue 1 and Coma Berenices are low

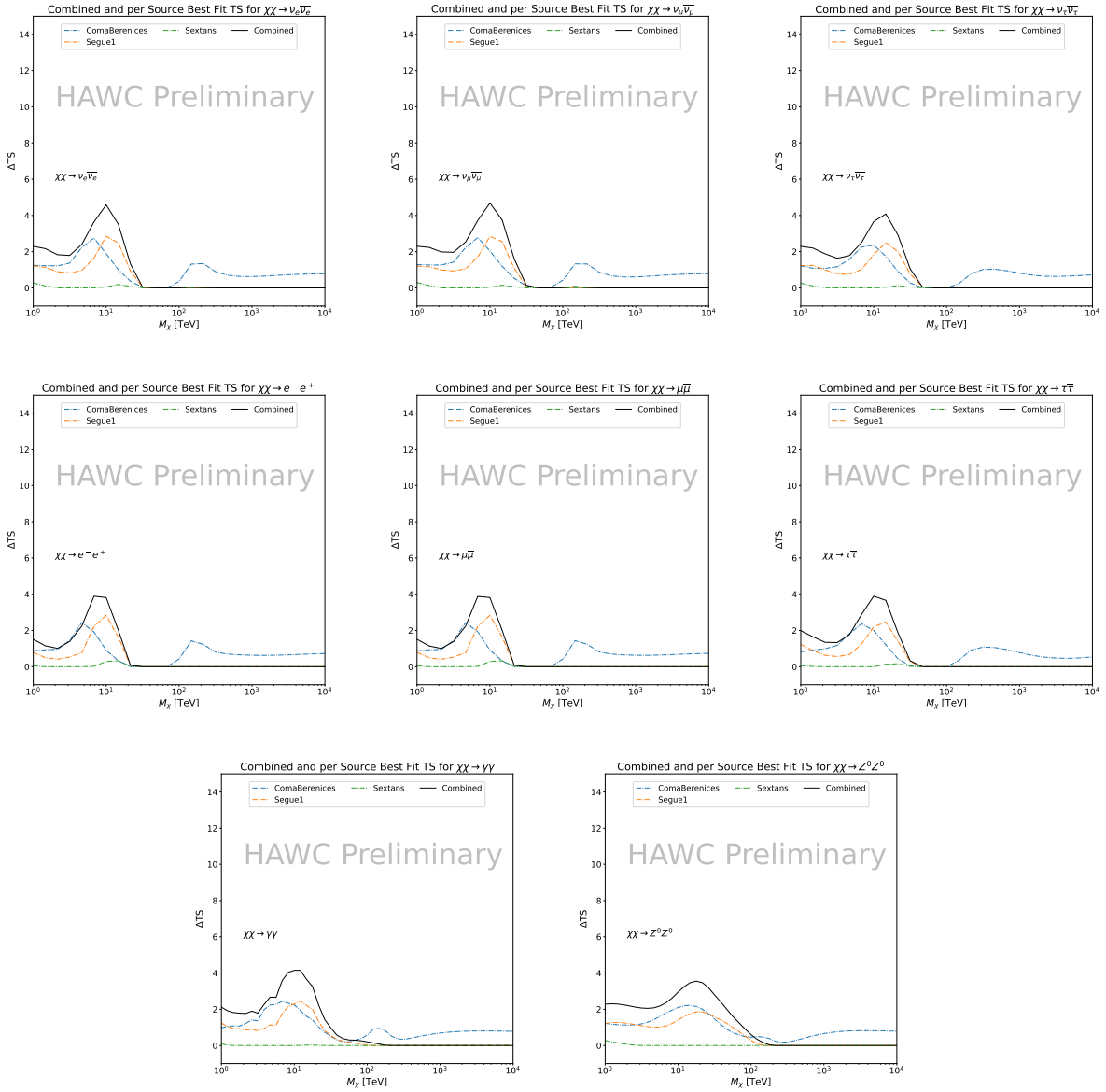


Figure 6.10 HAWC TS values for best fit $\langle\sigma v\rangle$ versus m_χ for SM annihilation channels: $\chi\chi \rightarrow \nu_e \bar{\nu}_e$, $\nu_\mu \bar{\nu}_\mu$, $\nu_\tau \bar{\nu}_\tau$, $e \bar{e}$, $\mu \bar{\mu}$, $\tau \bar{\tau}$, $\gamma\gamma$ and ZZ . Limits use $\mathcal{L}\mathcal{S} J$ factors. The solid black line shows the combined best fit TS values. The colored, dashed lines are the TS values from each dSph.

zenith where improvements to HAWC's analysis come only from energy estimation. Differences between these two are dominantly from their differences in J -factor, half-light radii of the dSphs, and the particle physics inputs. Substantial gains in HAWC's analysis methods (pass 5.F) were made at high zenith which is important for sources like Sextans. The HDM particle physics model produces almost identical spectra to the PPPC for $\chi\chi \rightarrow e^- e^+$, so can be used to compare limits

1338 between dSph. Overhead sources see minimal improvement to the limits, while high zenith sources
1339 see an order of magnitude improvement for all DM masses. Softer SM annihilation channels see
1340 broad improvements to the limit compared to harder channels.

1341 **6.7 Systematics**

1342 These are identical to what was performed earlier in Glory Duck, Section 5.7. We are also
1343 sensitive to the choice in spatial template, and this was explored in Section 5.7.2 and Section 5.8.2.

1344 **6.8 Conclusion and Discussion**

1345 In this multithreaded analysis, we have used observations of 3 dSphs from HAWC to perform
1346 a collective DM search for annihilation signals. The data were combined across sources to signifi-
1347 cantly increase the sensitivity of the search. Advanced computational techniques were deployed to
1348 accelerate wall-time spent analyzing by an order of magnitude. We have observed no significant
1349 deviation from the null, no DM, hypothesis, and so present our results in terms of upper limits on
1350 the annihilation cross-section for seventeen potential DM annihilation channels across four decades
1351 of DM mass.

1352 This analysis serves as a proof of concept for multithreaded HAWC analyses with large parameter
1353 spaces. Larger datasets with fast techniques will be essential to tackling the DM problem. The
1354 models we used for this study include annihilation channels with neutrinos in the final state.
1355 Advanced studies could aim to merge our results with those from neutrino observatories with large
1356 data sets.

1357 A full HAWC analysis will include systematic studies of the J -factor distributions. Additionally,
1358 because of the timing reduction, the study can be doubled in size to include DM decay. We have no
1359 yet received the remaining spatial profiles to the $\mathcal{L}\mathcal{S}$ catalog, and limits can be quickly computed
1360 once these are received. Finally, statistical studies with Poisson variation of HAWC’s background
1361 are essential to a comprehensive understanding of our observed excesses.

Segue1

Coma Berenices

Sextans

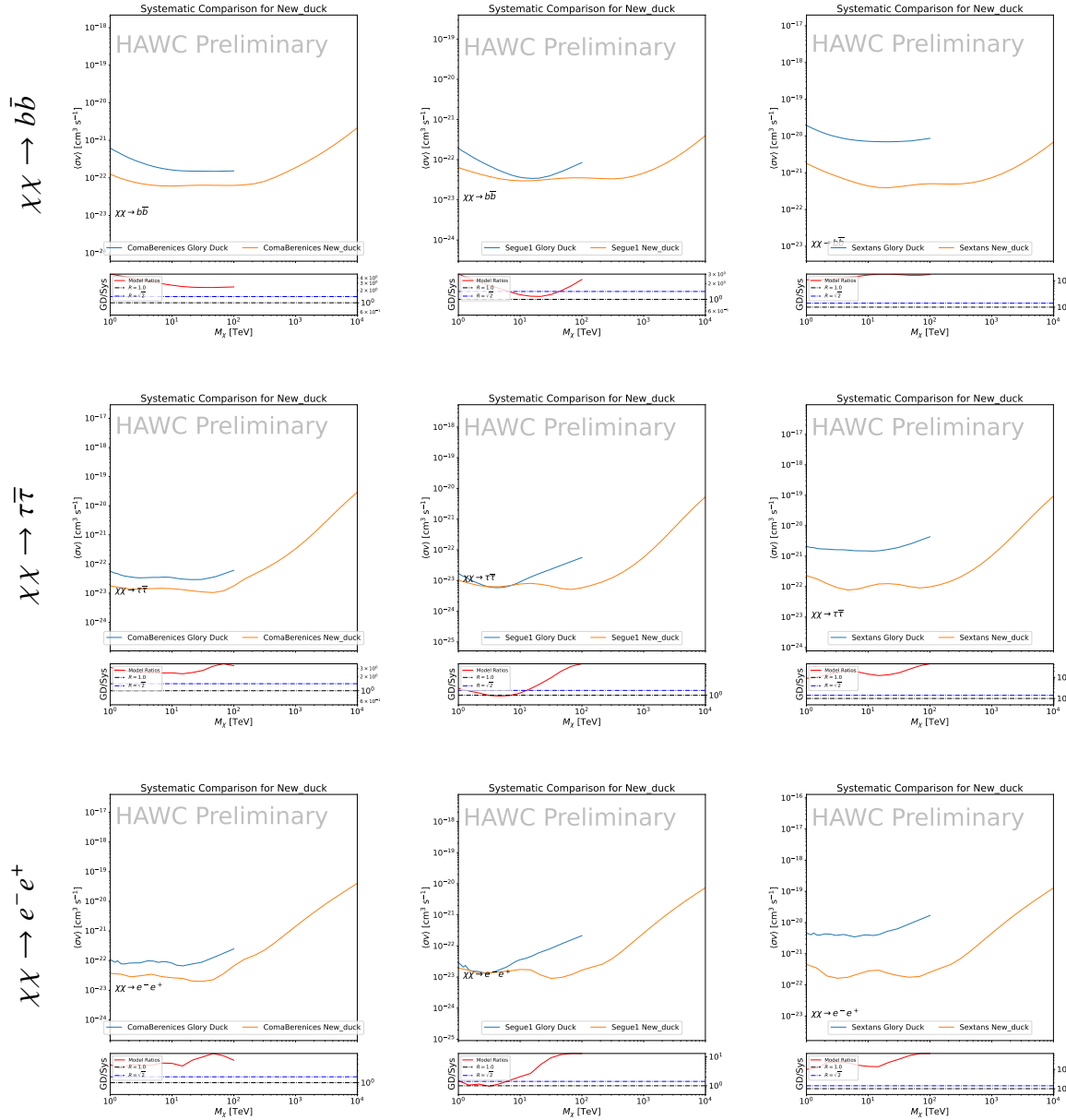


Figure 6.11 Comparison of HAWC limits from this analysis to Glory Duck (Fig. 5.5) for 3 dSphs and 3 SM annihilation channels: $b\bar{b}$, $\tau\bar{\tau}$, and $e\bar{e}$. Each sector shows the 95% confidence limit from Glory Duck (blue line) and this analysis (orange line) in the top plot. The lower plot features the ratio in log scale of Glory Duck to this analysis in a red solid line. Horizontal dashed lines are for ratios of 1.0 (black) and $\sqrt{2}$ (blue). Ratios larger than 1.0 are for limits smaller, or stricter, than Glory Duck. Ratios larger than $\sqrt{2}$ indicates limits are stricter than a simple doubling of the Glory Duck data.

CHAPTER 7

1362 HEAVY DARK MATTER ANNIHILATION SEARCH WITH ICECUBE'S NORTH SKY 1363 TRACK DATA

1364 7.1 Introduction

1365 Neutrinos are another astrophysical messenger than can travel long distances without interaction.
1366 Uniquely, they interact less readily than photons especially above PeV energies. Neutrinos thereofre
1367 provide another window through which we can perform dark matter searches. Neutrinos come in
1368 three flabors and so this triples the multiplicity of the particles we are searching for.

1369 Icecube has not done a DM annihilation analysis towards dwarf galaxies for a while. **TODO:**
1370 [cite 2013 paper](#). This is in spite of the potentially crucial sensitivity afforded from neutrino spectral
1371 lines [TODO: cite dan hooper and neutrino lines](#). A lot has changed in IC3 since that last analysis (we
1372 have more strings, we have much more sophisticated analysis methods, and the theory modeling
1373 has made significant leaps.) Therefore it is time to finally do a DM search toward dSphs. The hope
1374 is that by laying down the important statistical foundation as well, that this work can be meshed
1375 with gamma-ray data. IceCube is sensitive to annihilating DM to the DM ranges above 1 TeV
1376 and can produce competitive results relative to gamma ray observatories in spectral models that
1377 produce sharp neutrino features. The goal of this analysis is to perform a DM annihilation search
1378 using the new datasets NST. The search will only be towards dwarf spheroidal galaxies (dSph).
1379 These sources are known for their low backgrounds and high DM contents. Since the dataset is
1380 sensitive to the north and south, as many dSph as possible will be included. Additionally, with
1381 annihilation, these sources can be treated as point sources with little loss to sensitivity or model
1382 dependence on how the DM is distributed. DM masses from 500 GeV to 100 PeV are considered
1383 for this analysis. All standard model annihilation channels available from the HDMspectra are
1384 studied in this analysis.

1385 Additional work is done to extract the Likelihood profiles for each DM, source hypothesis so
1386 that these data can be combined with gamma-ray observatories. This work is considered a separate
1387 project as the statistical treatment is unique from many IceCube analyses. The wiki for [the

1388 combined analysis] **TODO: instead point to chapter**This chapter presents the analysis work for
1389 IC3 for DM searches toward dSphs. This section describes the various steps and features of the
1390 analysis. It is structure first introduces the data and how it is treated, then systematic studies of the
1391 dwarves individually. Finally, the stacked analysis and results are presented.

1392 **7.2 Dataset and Background**

1393 This section enumerates the data and background methods used for IceCube's study of dSphs.
1394 Section 7.2.1 and Section 7.2.2 are most useful for fellow IceCube collaborators looking to replicate
1395 this analysis.

1396 **7.2.1 Itemized IceCube files**

- 1397 • Software Environment: CVMFS Py3-v4.1.1
- 1398 • Data Sample: Northern Tracks NY86v5p1
- 1399 • Analysis Software: csky ([nu_dark_matter](#))
- 1400 • Analysis wiki: https://wiki.icecube.wisc.edu/index.php/Dark_Matter_Annihilation_Search_towards_dwarf_spheroidals_with_NST_and_DNN_Cascades
- 1402 • Project repository

1403 **7.2.2 Software Tools and Development**

1404 This analysis was performed inside IceCube's CVMFS (3.4.1.1) software environment using
1405 csky for likelihood calculations. Csky did not come with dark matter spectral models nor could
1406 accomodate custom flux models. We developed these capacities for single source and stacked
1407 source studies for this analysis. The analysis code is held in a separate repository from csky. The
1408 [nu_dark_matter](#) branch of csky manages the input of custom dark matter spectra and accompanied
1409 DM astrophysical source then calculates likelihoods with a selected data sample. The [IceCube Dark](#)
1410 [Matter dSph repository](#) manages the generation of spectral models for neutrinos, physics parameter
1411 extraction from n_{sig} , J -factor per source inputs, and bookkeeping for the large parameter space.
1412 The project repository required a secondary software environment for neutrino oscillations. How

1413 to launch and run those calculations are documented in the project repository and the Docker image
1414 is additionally saved in Section C.1

1415 **7.2.3 Data Set and Background Description**

1416 For this analysis, I use the Northern Sky Tracks (NST) Sample (Version V005-P01). The sample
1417 contains up-going track-like events, usually from ν_μ and ν_τ and has a superior angular resolution
1418 compared to the cascade dataset. This sample covers 10.4 years of data (IC86_2011-2021). The
1419 accepted neutrino energy range used for the analysis is unique from most other IceCube searches
1420 because DM spectra are very hard. The sampled energy range is $1 < \log(E_\nu/\text{GeV}) < 9.51$ with
1421 step size 0.125.

1422 The strength of a dwarf analysis is that there is no additional background consideration beyond
1423 nominal, baseline background estimations. For NST, the nominal contribution comes from atmo-
1424 spheric neutrinos and isotropic astrophysical neutrinos. We estimate the background by scrambling
1425 NST data along Right Ascension.

1426 **7.3 Analysis**

1427 The expected differential neutrino flux from DM-DM annihilation to standard model particles,
1428 $d\Phi_\nu/dE_\nu$, over solid angle, Ω is described by the familiar equation.

$$\frac{d\Phi_\nu}{dE_\nu} = \frac{\langle\sigma v\rangle}{8\pi m_\chi^2} \frac{dN_\nu}{dE_\nu} \times \int_{\text{source}} d\Omega \int_{l.o.s} \rho_\chi^2 dl(r, \theta') \quad (7.1)$$

1429 This is identical to past examples except that there are 3 neutrino flavors, so there are a corresponding
1430 3 flux equations. Section 5.3 has a complete description of all the terms. Additionally, neutrinos
1431 oscillate between flavors which needs to be considered for the expected neutrino flux at Earth.
1432 Section 7.3.1 presents the particle physics model for DM annihilation. Section 7.3.2 presents the
1433 spatial distributions built for each dSph.

1434 **7.3.1 $\frac{dN_\nu}{dE_\nu}$ - Particle Physics Component**

1435 Neutrino spectra from heavy dark matter annihilation were generated using HDMSSpectra [64]
1436 and χ arrov [68]. HDMSSpectra simulates the decay and annihilation of heavy dark matter, for
1437 different dark matter masses and SM primary annihilation channels. The simulation includes

1438 electroweak radiative corrections and higher order loop corrections with quarks. This publication
 1439 also pushes the simulated DM mass to the Plank scale (1 EeV), however this study will not explore
 1440 that high.

1441 An important novel feature in the spectra is that neutrino line channels will be accompanied
 1442 with a low energy tail. Thus the earth will not fully attenuate a neutrino SM channel signal from
 1443 high declination sources where the neutrino flux must first traverse through the Earth. The SM
 1444 annihilation channels that feature lines include all leptonic channels. ($\nu_{e,\mu,\tau}$, e , μ , and τ) We use
 1445 [Xarov](#) to propagate and oscillate the neutrinos from the source to Earth. Because these sources are
 1446 quite large in absolute terms, and also far (order 10 kpc or more), the resulting flavor spectra are
 1447 the averages of the transition probabilities [68]:

$$P(\nu_\alpha \rightarrow \nu_\beta) \approx \begin{bmatrix} 0.55 & 0.18 & 0.27 \\ 0.18 & 0.44 & 0.38 \\ 0.27 & 0.38 & 0.35 \end{bmatrix} \quad (7.2)$$

1448 When calculating the expected contribution to n_s , only ν_μ , ν_τ are considered as NST's effective
 1449 area to ν_e is essentially 0. With these consideration, the expected composite neutrino spectrum
 1450 is a average of the two flavors: $(\nu_\mu + \nu_\tau)/2$. The spectral tables are then converted to splines to
 1451 condense information, enable random sampling of the spectra, and enable faster computation times.
 1452 The spectral splines are finally implemented as a DM class in csky. Examples of the spectra before
 1453 and after propagation are shown in Fig. 7.1.

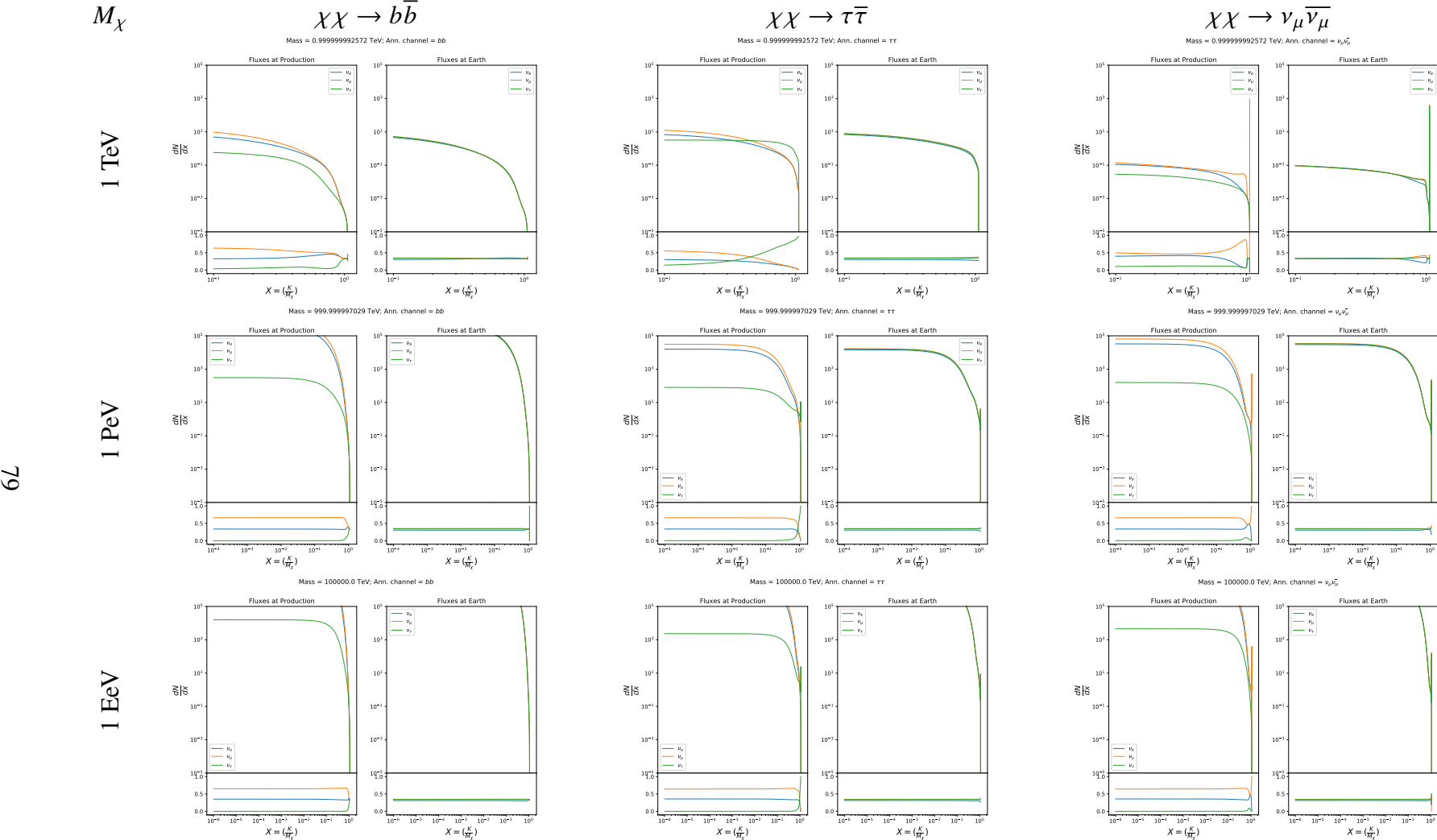


Figure 7.1 Neutrino spectra at production (left panels) and after oscillation at Earth (right panels). Blue, orange, and green lines are the ν_e , ν_μ , and ν_τ spectra respectively. Top panels show the spectra in $\frac{dN}{dE}$. Lower panels plot the flavor ratio to $\nu_e + \nu_\mu + \nu_\tau$. SM annihilation channels $b\bar{b}$, $\tau\bar{\tau}$, and $\nu_\mu \bar{\nu}_\mu$ are shown for $M_\chi = 1 \text{ PeV}$, TeV , and EeV .

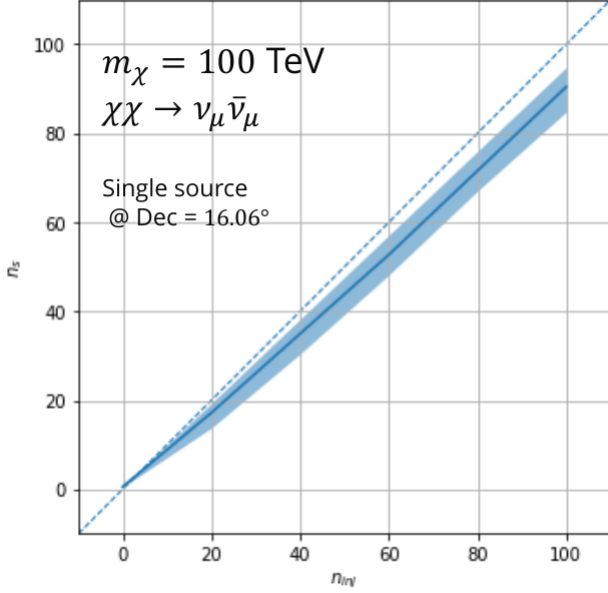


Figure 7.2 Signal recovery for 100 TeV DM annihilation into $\nu_\mu \bar{\nu}_\mu$ for a source at Dec = 16.06°. n_{inj} is the number of injected signal events in simulation. n_s is the number of reconstructed signal events from the simulation. Although the uncertainties are small and tight, the reconstructed n_s are systematically underestimated.

7.3.1.1 Treatment of Neutrino Line Features

All leptonic DM annihilation channels $\chi\chi \rightarrow [\nu_{e,\mu,\tau}, e, \mu, \tau]$ develop a prominent and narrow spectral line feature. For all neutrino flavors, this line is visible and prominent in all mass models studied for this analysis. For charged leptons, the feature only really shows up at the larger DM mass models. Examples for lines in both neutrinos and charged leptons annihilation are provided in Fig. 7.1. This line feature is so narrow relative the sampled energy range that the MC rarely samples within the neutrino line. As a result, often the best fit to simulation of background will always floor to TS = 0 and the signal recovery tends to be conservative.

To remedy this, a similar approach to the IceCube’s decay analysis [TODO: refer to Minjin’s page](#). 2 kernels were tested (Gaussian, uniform (flat)) to smooth out the line feature. The widths were tuned such that the signal recovery approached unity for DM mass 100 TeV to 1 PeV. Additionally, the tuning was performed only for a source at declination 16.06 (Segue 1). This is to avoid confusion loss in signal recovery from too narrow a line and from Earth’s attenuation of high energy neutrinos. The convolution also needed to as close as possible preserve the integrated counts of neutrinos. The optimized kernel window for all lines is summarized as:

- 1469 • Gaussian kernel w/ 2σ width = $3.5E-3 \cdot m_\chi$
- 1470 • Minimum energy included in convolution = $\text{MIN}[0.995 \cdot m_\chi, En(\nu_{line}) - 4\sigma]$
- 1471 • Maximum energy included in convolution = $\text{MAX}[1.005 \cdot m_\chi, En(\nu_{line}) + 4\sigma]$

1472 where $En(\nu_{line})$ is the neutrino energy where the neutrino line is at the maximum.

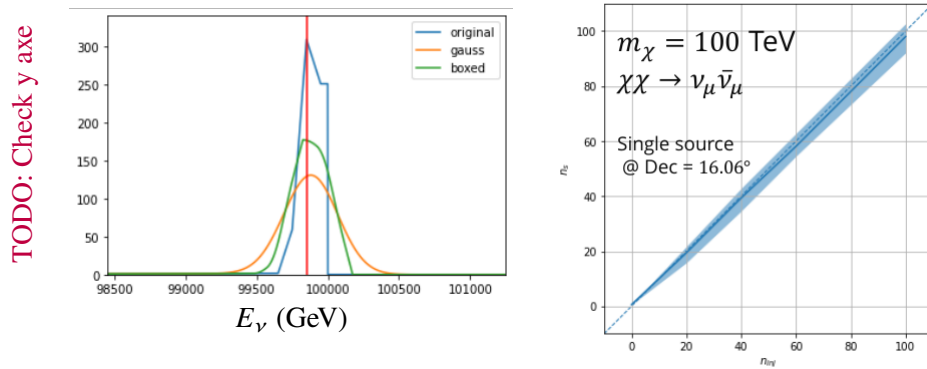


Figure 7.3 Top left panel shows the two kernels overlaid the original spectrum from Charon. delta I is the difference in the integral of the peaks with respect to the original spectrum. The vertical red line indicated where the original neutrino line is maximized. Lower right shows the signal recoveries of the DM model using the Gaussian kernel with parameters enumerated above.

1473 These parameters broadly improved the signal recovery of the line spectra. An example is
1474 provided below. Signal recovery plots of the full analysis are provided much further down.

1475 7.3.1.2 Spline Fitting

1476 In an effort to reduce computational work, memory burden, and align with point source methods
1477 used for NGC1068 and Seyfert analyses, spectral splines were created and adopted for estimating
1478 the neutrino flux for the different annihilation. Software was written to generate, handle, and
1479 calculate values on the splines. When using splines, one has to be careful of the goodness to fit.
1480 There are critical caveats when testing the goodness to fit to MC generated above for all channels.

- 1481 • The splines must be Log10(*) in Energy and dN/dE to account for the exponential nature of
1482 the flux
- 1483 • The fidelity of the fit matters more at $E_\nu \approx m_\chi$ where the model uncertainties are minimal
1484 and physical considerations (like the cut-off) are most apparent.

- 1485 • The fidelity of the fit matters less at low E_ν as the model uncertainties are large AND
 1486 IceCube's sensitivity diminishes significantly below 500 GeV

- 1487 • Total integrated counts should be well preserved, however, the resolution of the MC is much
 1488 higher than IceCube's energy resolution.

1489 – Meaning over several steps in E, the integral is preserved

1490 – the step size enters the cost function

1491 – Oscillating residuals, so long as they are very small and well centered, are not penalized
 1492 as this gets averaged out.

1493 The resulting cost function to evaluate the goodness of fit was used to account for the above
 1494 considerations.

$$e_i = x_i \cdot \left(\frac{dN_i}{dE_i} - 10^{\hat{e}_i} \right) \quad (7.3)$$

1495 Where \hat{e}_i is the spline estimator's value for x_i . $x_i = E_{\nu_i}/m_\chi$. $\frac{dN_i}{dE_i}$ is the flux value from MC.

$$\text{err} = \sqrt{\frac{1}{x_{\max} - x_{\min}} \int_{x_{\min}}^{x_{\max}} e^2 dx} \quad (7.4)$$

1496 I then take the RMS of the error distribution and the resulting value (err) is used to evaluate
 1497 the fidelity of the spectral spline. Each SM channel had different tolerances for 'err'. Channels
 1498 with very hard cut-offs had looser tolerance for err because a lot of error would be generated from
 1499 the cut-off being estimated to occur slightly early or late. Soft channels don't have this issue and
 1500 therefore the tolerance is very strict. The table blow summarizes the tolerances for the SM channels.

1502 **7.3.2 J- Astrophysical Component**

$\chi\chi \rightarrow$	GOOD	OK	FAIL	Limits of err calc [X_{min}, X_{max}]
$Z^0 Z^0, W^+ W^-$	1.0E-3	1.0E-3, 1.0E-2	1.0E-2	MAX[100GeV/ m_χ , 10^{-6}], 1.0
$t\bar{t}, hh$	1.0E-5	1.0E-5, 1.0E-4	1.0E-4	MAX[100GeV/ m_χ , 10^{-6}], 1.0
$b\bar{b}, d\bar{d}, u\bar{u}$	9.0E-7	9.0E-7, 9.0E-6	9.0E-6	MAX[100GeV/ m_χ , 10^{-6}], 1.0
$\nu\bar{\nu}_{e,\mu,\tau}$	1.0E-3	1.0E-3, 1.0E-2	1.0E-2	MAX[100GeV/ m_χ , 10^{-6}], MIN[0.995, ($En(\nu_{line}) - 4\sigma$)/ M_χ]
$e\bar{e}, \mu\bar{\mu}, \tau\bar{\tau}$	1.0E-3	1.0E-3, 1.0E-2	1.0E-2	MAX[100GeV/ m_χ , 10^{-6}], MIN[0.995, ($En(\nu_{line}) - 4\sigma$)/ M_χ]

Table 7.1 TODO: fill me daddy

1503

CHAPTER 8

NU DUCK

APPENDIX A

MULTI-EXPERIMENT SUPPLEMENTARY FIGURES

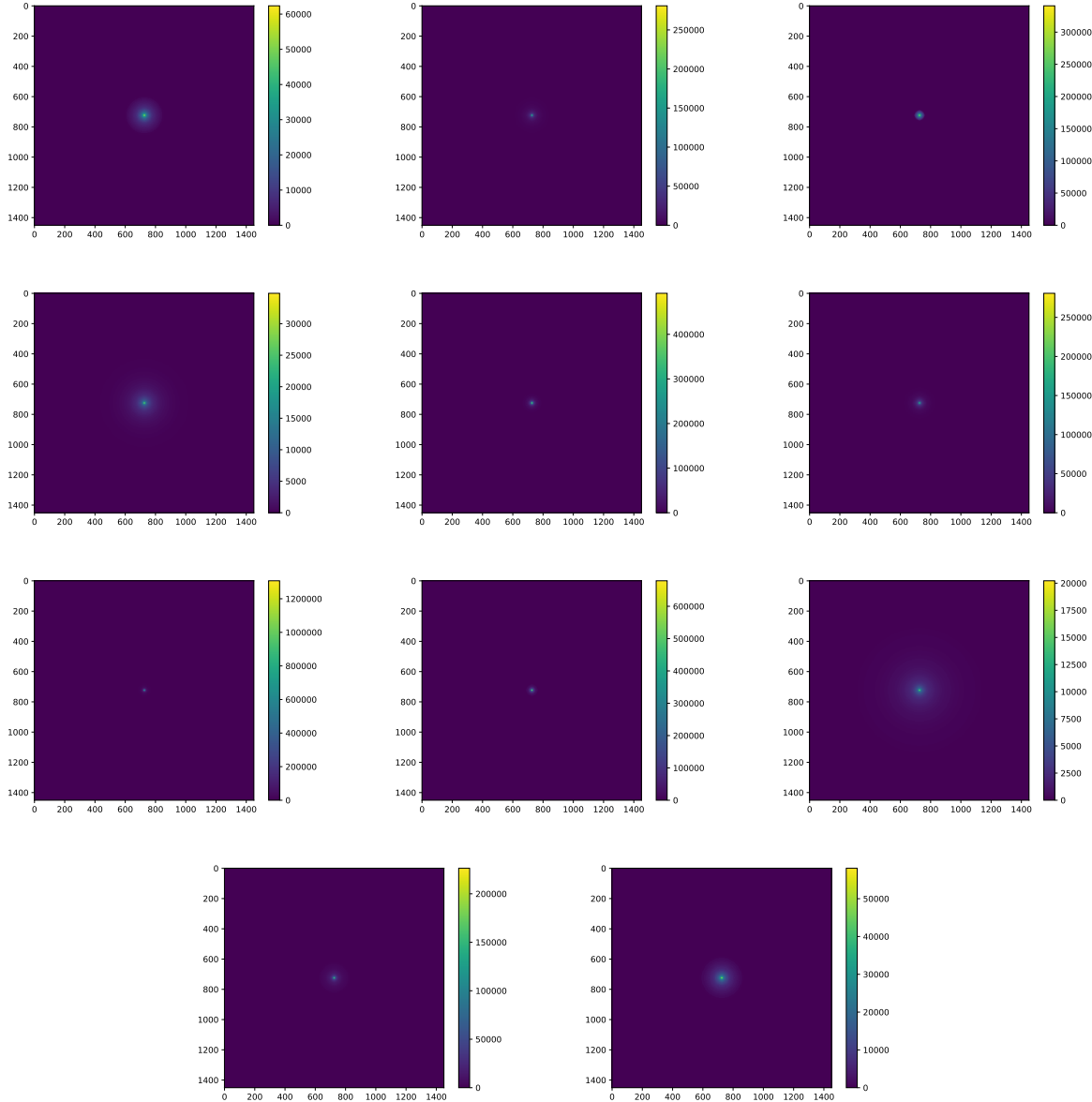


Figure A.1 Sister figure to Figure 5.3. Sources in the first row from left to right: Bootes I, Canes Venatici I, II. In second row: Draco, Hercules, Leo I. In the first row: Leo II, Leo IV, Sextans. In the final row: Ursa Major I, Ursa Major II.

APPENDIX B

1505 MULTITHREADING DARK MATTER ANALYSES SUPPLEMENTARY MATERIAL

1506 B.1 Remaining Spectral Models

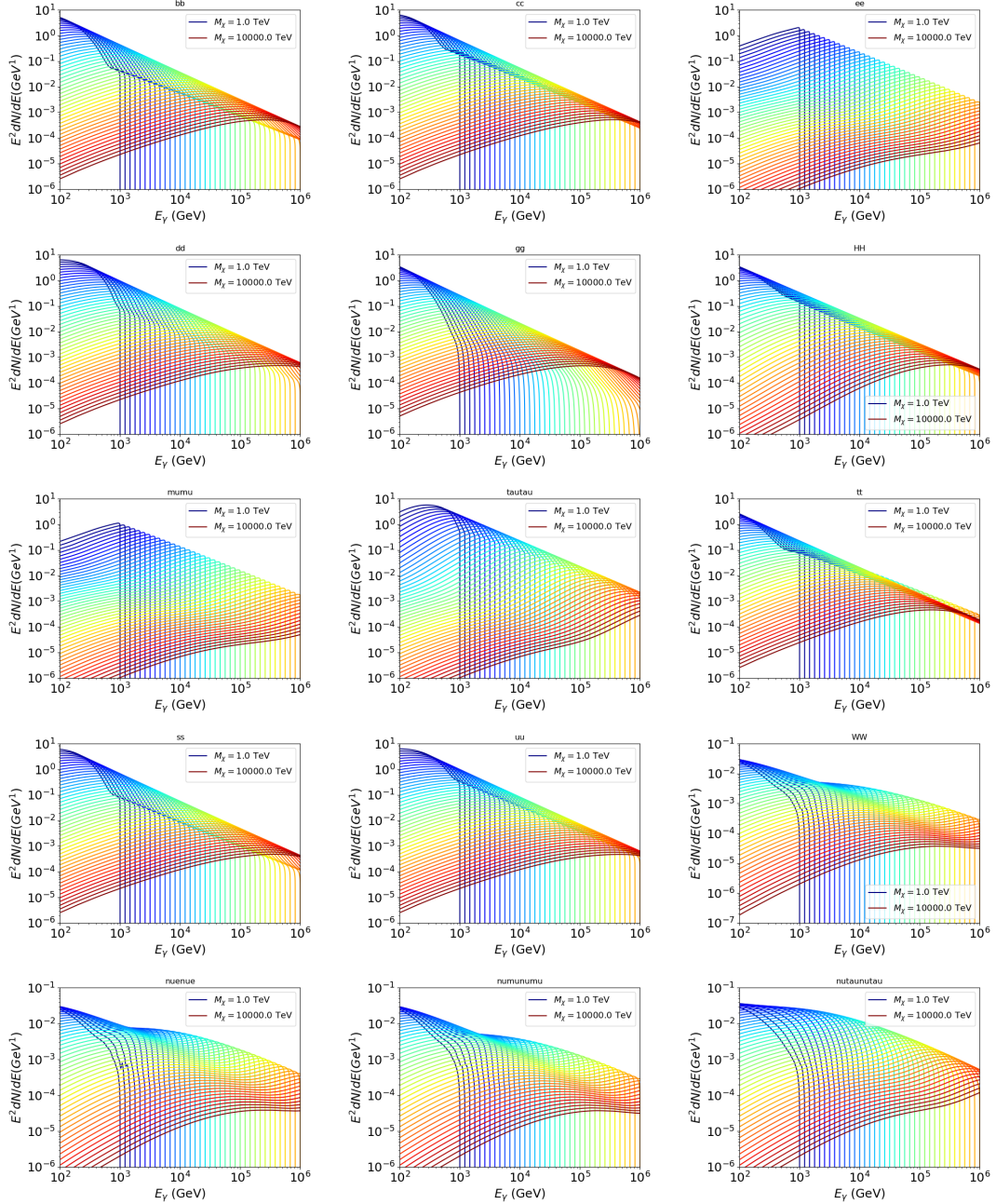


Figure B.1 Sister figure to Figure 6.2 for remaining SM primary annihilation channels studied for this thesis. These did not require any post generation smoothing and so are directly pulled from [64] with a binning scheme most helpful for a HAWC analysis.

1507 B.2 mpu_analysis.py

```
15081 import warnings
15092 with warnings.catch_warnings():
15103     warnings.simplefilter("ignore")
15114 # Python base libraries
15125 import os
15136 import sys
15147 import time
15158 # Import general libraries with namespace
15169 import matplotlib
15170 # Necessary for computing on cluster
15181 matplotlib.use("agg")
15192 import numpy as np
15203 import multiprocessing as mp
15214 # Import HAWC software
15225 sys.path.insert(1, os.path.join(os.environ['HOME'], 'hawc_software', 'threeML-
1523     analysis-scripts', 'fitModel'))
15246 from analysis_modules import *
15257 from threeML import *
15268 from hawc_hal import HAL, HealpixConeROI
15279 from threeML.minimizer.minimization import FitFailed
15280 # Import Dark Matter HAWC Libraries
15291 import analysis_utils as au
15302 import spectra as spec
15313 import sources as srcs
15324
15335 #* READ ONLY PATHS This block will change eventually
15346 MASS_LIST = './plotting/studies/nd/masses.txt'
15357 CHAN_LIST = './plotting/studies/nd/chans.txt'
15368
15379 #* WRITE PATHS, default location is to scratch
15380 OUT_PATH = os.path.join(os.environ["SCRATCH"], os.environ["USER"], 'New_duck')
```

```

15391 print('Our out path is going to be {}'.format(OUT_PATH))
15402
15413 # Define parallel Function. Can also be run serially
15424 def some_mass_fit(sigVs, datalist, shape, dSph, jfactor, mass_chan,
15435                 progress=None, log_file='', queue=None, i_job=0):
15446
15457     if progress is None:
15468         progress = [0]
15479     else: # Create log files for each thread
15480         log_file = log_file.replace('.log', '_ThreadNo_')
15491         log_file = log_file + str(i_job) + ".log"
15502         sys.stdout = open(log_file, "w")
15513
15524     fits = []
15535
15546     try:
15557         for m_c in mass_chan:
15568             print(f'Mass chan tuple: {m_c}')
15579             mass = int(m_c[0])
15580             ch = m_c[1]
15591             # Build path to output files
15602             outPath = os.path.join(OUT_PATH, ch, dSph)
15613             au.ut.ensure_dir(outPath)
15624
15635             if progress[i_job] < 0:
15646                 # If the master gets a Keyboard interrupt, commit suicide.
15657                 break
15668
15679                 ### Start Model Building for DM mass and SM channel #####
15680                 spectrum = spec.DM_models.HDMSpectra()
15691                 spectrum.set_channel(ch)
15702
15713                 myDwarf = ExtendedSource(dSph, spatial_shape=shape,

```

```

15724                     spectral_shape=spectrum)
15735
15746             spectrum.J = jfactor * u.GeV**2 / u.cm**5
15757             spectrum.sigmav = 1e-24 * u.cm**3 / u.s
15768             spectrum.set_dm_mass(mass * u.GeV)
15779
15780             spectrum.sigmav.bounds = (1e-30, 1e-12)
15791             model = Model(myDwarf)
15802             ##### End model Building #####
15813
15824             jl = JointLikelihood(model, datalist, verbose=False)
15835
15846             try:
15857                 result, lhdf = jl.fit(compute_covariance=False)
15868                 ts = -2.* (jl.minus_log_like_profile(1e-30) - jl.
1587 _current_minimum)
15889                 # Also profile the LLH vs sv
15890                 ll = jl.get_contours(spectrum.sigmav, sigVs[0],
15901                               sigVs[-1], len(sigVs),
15912                               progress=False, log=['False'])
15923
15934                 sigv_ll = au.ut.calc_95_from_profile(ll[0], ll[2])
15945                 # Write results to file
15956                 outFileLL = outPath+f"/LL_{dSph}_{ch}_mass{int(mass)}_GD.txt"
15967                 np.savetxt(outFileLL, (sigVs, ll[2]),
15978                               delimiter='\t', header='sigV\tLL\n')
15989
15990                 with open(outPath+f"/results_{dSph}_{ch}_mass{int(mass)}_GD.
1600 txt", "w") as results_file:
16011                     results_file.write("mDM [GeV]\tsigV_95\tsigV_B.F.\n")
16022
16033                     results_file.write("%i\t%.5E\t%.5E\t%.5E"%(mass, sigv_ll,
16044                                         ts, result.value[0]))

```

```

16055         # End write to file
16056
16057     except FitFailed: # Don't kill all threads if a fit fails
16058         print("Fit failed. Go back and calculate this spectral model
16059             later")
16060
16061         fits.append((ch, mass, -1, -1))
16062
16063     with open(log_file+'.fail', 'w') as f_file:
16064         f_file.write(f'{ch}, {mass}\n')
16065
16066
16067     progress[i_job] += 1
16068
16069     matplotlib.pyplot.close() # Prevent leaky memory
16070
16071
16072     fits.append((ch, mass, result.value[0], ts))
16073
16074     progress[i_job] += 1
16075
16076     matplotlib.pyplot.close()
16077
16078 except KeyboardInterrupt:
16079     progress[i_job] = -1
16080
16081
16082     fits = np.array(fits)
16083
16084     if queue is None:
16085
16086         return fits
16087
16088     else:
16089
16090         queue.put((i_job, fits))
16091
16092
16093 def main(args):
16094
16095     masses = np.loadtxt(MASS_LIST, dtype=int)
16096
16097     chans = np.loadtxt(CHAN_LIST, delimiter=',', dtype=str)
16098
16099     mass_chan = au.ut.permute_lists(chans, masses)
16100
16101
16102     print(f"DM masses for this study are: {masses}")
16103
16104     print(f"SM Channels for this study are XX -> {chans}")
16105
16106     print(mass_chan)
16107
16108
16109     # extract information from input argument

```

```

16387 dSph = args.dSph
16398 data_mngr = au.ut.Data_Selector('P5_NN_2D')
16409 dm_profile = srcts.Spatial_DM(args.catalog, dSph, args.sigma, args.decay)
16410
16421 ##### Extract Source Information #####
16432 if dm_profile.get_dec() < -22.0 or dm_profile.get_dec() > 62.0:
16443     raise ValueError("HAWC can't see this source D: Exitting now...")
16454
16465 print(f'{dSph} information')
16476 print(f'jfac: {dm_profile.get_factor()}\tRA: {dm_profile.get_ra()}\tDec: {dm_profile.get_dec()}\n')
1648
16497
16508 shape = SpatialTemplate_2D(fits_file=dm_profile.get_src_fits())
16519 ##### Finish Extract Source Information #####
16520
16531 ##### LOAD HAWC DATA #####
16542 roi = HealpixConeROI(data_radius=2.0, model_radius=8.0,
16553                         ra=dm_profile.get_ra(), dec=dm_profile.get_dec())
16564 bins = choose_bins.analysis_bins(args, dec=dm_profile.get_dec())
16575
16586 hawc = HAL(dSph, data_mngr.get_datmap(), data_mngr.get_detres(), roi)
16597 hawc.set_active_measurements(bin_list=bins)
16608 datalist = DataList(hawc)
16619 ##### FINISH LOAD HAWC DATA #####
16620
16631 # set up SigV sampling. This sample is somewhat standardized
16642 sigVs = np.logspace(-28,-18, 1001, endpoint=True) # NOTE This will change
1665 whith HDM
16663
16674 if args.n_threads == 1:
16685     # No need to start || programming just iterate over the masses
16696     kw_arg = dict(sigVs=sigVs, datalist=datalist, shape=shape, dSph=dSph,
16707                     jfactor=dm_profile.get_factor(), mass_chan=mass_chan,

```

```

16718                 log_file=args.log)
16729             some_mass_fit(**kw_arg)
16730         else:
16741             # I Really want to suppress TQMD output
16752             from tqdm import tqdm
16763             from functools import partialmethod
16774             tqdm.__init__ = partialmethod(tqdm.__init__, disable=True)
16785
16796             x = np.array_split(mass_chan, args.n_threads)
16807             n_jobs = len(x)
16818
16829             print("Thread jobs summary by mass and SM channel")
16830             for xi in x:
16841                 print(f'{xi}')
16852
16863             queue = mp.Queue()
16874             progress = mp.Array('i', np.zeros(n_jobs, dtype=int))
16885
16896             # Define task pool that will be split amongsts threads
16907             kw_args = [dict(sigVs=sigVs, datalist=datalist, shape=shape,
16918                             dSph=dSph, jfactor=dm_profile.get_factor(),
16929                             mass_chan=mass_chan, progress=progress,
16930                             queue=queue, i_job=i, log_file=args.log)
16941                 for i, mass_chan in enumerate(x)]
16952
16963             # Define each process
16974             procs = [mp.Process(target=some_mass_fit, kwargs=kw_args[i]) \
16985                 for i in range(n_jobs)]
16996
17007             ### Start MASTER Thread only code block ###
17018             # Begin running all child threads
17029             for proc in procs: proc.start()
17030

```

```

17041     try:
17052         # In this case, the master does nothing except monitor progress of
1706         the threads
17073         # In an ideal world, the master thread also does some computation.
17084         n_complete = np.sum(progress)
17095         while_count = 0
17106
17117         while n_complete < len(mass_chan):
17128
17139             if np.any(np.asarray(progress) < 0):
17140                 # This was no threads are stranded when killing the script
17151                 raise KeyboardInterrupt()
17162             if while_count%1000 == 0:
17173                 print(f"{np.sum(progress)} of {len(mass_chan)} finished")
17184
17195             n_complete = np.sum(progress)
17206             time.sleep(.25)
17217             while_count += 1
17228
17239         except KeyboardInterrupt:
17240             # signal to jobs that it's time to stop
17251                 for i in range(n_jobs):
17262                     progress[i] = -2
17273                     print('\nKeyboardInterrupt: terminating early.')
17284             ### End MASTER Thread only code block ###
17295
17306             fitss = [queue.get() for proc in procs]
17317             print(fitss)
17328             print(f'Thread statuses: {progress[:]}')
17339
17340             # putting results in a file
17351
17362             print("QUACK! All Done!")

```

```

17373
17384
17395 if __name__ == '__main__':
17406     import argparse
17417
17428     p = argparse.ArgumentParser(description="Run a DM annihilation analysis on
1743         a dwarf spheroidal for a specific SM channel for DM masses [1 TeV to 10
1744         PeV]")
17459
17460     # Dwarf spatial modeling arguements
17471     p.add_argument("-ds", "--dSph", type=str,
17482             help="dwarf spheroidal galaxy to be studied", required=
1749     True)
17503     p.add_argument("-cat", "--catalog", type=str, choices=['GS15', 'LS20'],
17514             default='LS20', help="source catalog used")
17525     p.add_argument("-sig", "--sigma", type=int, choices=[-1, 0, 1], default=0,
17536             help="Spatial model uncertainty. 0 corresponds to the
1754 median. +/-1 correspond to the +/-1sigma uncertainty respectively.")
17557
17568     # Arguements for the energy estimators
17579     p.add_argument("-e", "--estimator", type=str,
17580             choices=['P5_NHIT', 'P5_NN_2D'],
17591             default="P5_NN_2D", required=False,
17602             help="The energy estimator choice. Options are: P5_NHIT,
1761 P5_NN_2D. GP not supported (yet).")
17623     p.add_argument("--use-bins", default=None, nargs="*",
17634             help="Bins to use for the analysis", dest="use_bins")
17645     p.add_argument('--select_bins_by_energy', default=None, nargs="*",
17656             help="Does nothing. May fill in later once better
1766 understood")
17677     p.add_argument('--select_bins_by_fhit', default=None, nargs="*",
17688             help="Also does nothing see above")
17699     p.add_argument( '-ex', "--exclude", default=None, nargs="*",

```

```

17700         help="Exclude Bins", dest="exclude")

17751

17722 # Computing and logging arguements.

17733 p.add_argument('-nt', '--n_threads', type=int, default=1,
17744                         help='Maximum number of threads spawned by script. Default
17755 is 4')

17765 p.add_argument('-log', '--log', type=str, required=True,
17776                         help='Name for log files. Especially needed for threads')

17787

17798 p.add_argument('--decay', action="store_true",
17809                         help='Set spectral DM hypothesis to decay')

17810

17821 args = p.parse_args()

17832 print(args.decay)

17843 if args.exclude is None: # default exclude bins 0 and 1
17854     args.exclude = ['B0C0Ea', 'B0C0Eb', 'B0C0Ec', 'B0C0Ed', 'B0C0Ee']

17865

17876 if args.decay: OUT_PATH += '_dec'
17887 else: OUT_PATH += '_ann'

17898

17909 OUT_PATH = OUT_PATH + '_' + args.catalog
17910 if args.sigma != 0: OUT_PATH += f'_{args.sigma}sig'

17921

17932 main(args)

```

1794 B.3 Comparison with Glory Duck

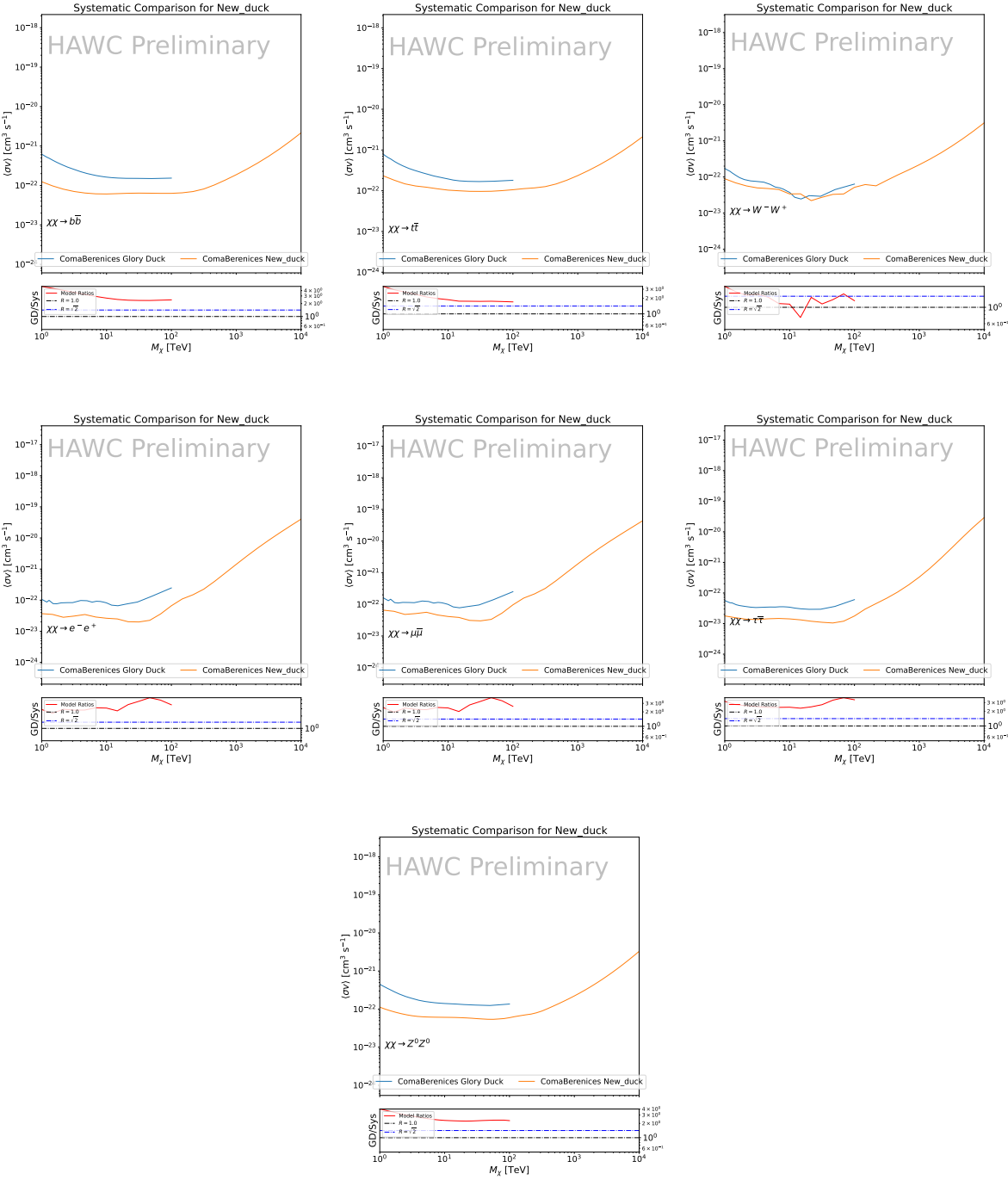


Figure B.2 TODO: fill this out

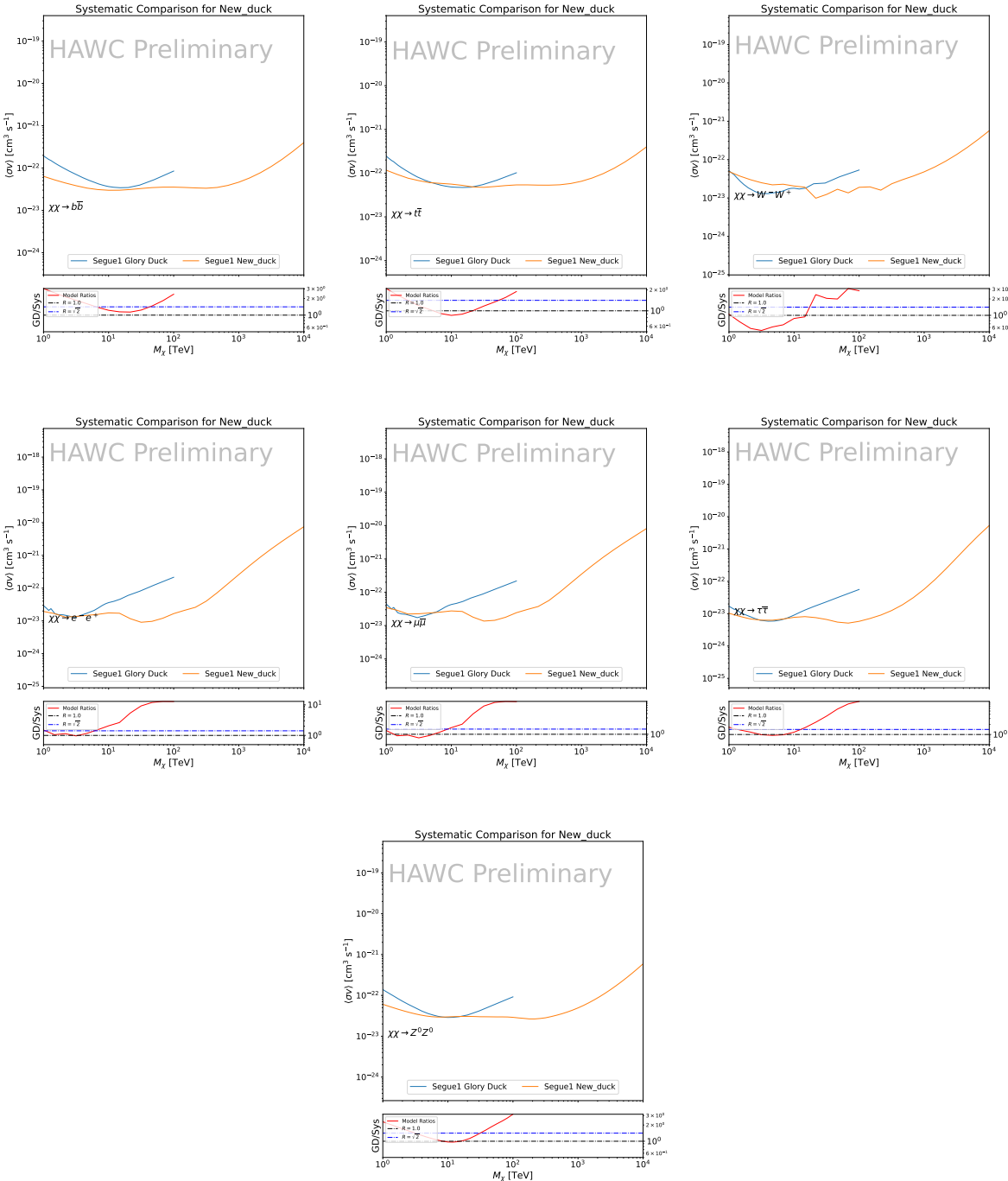


Figure B.3 TODO: fill this out

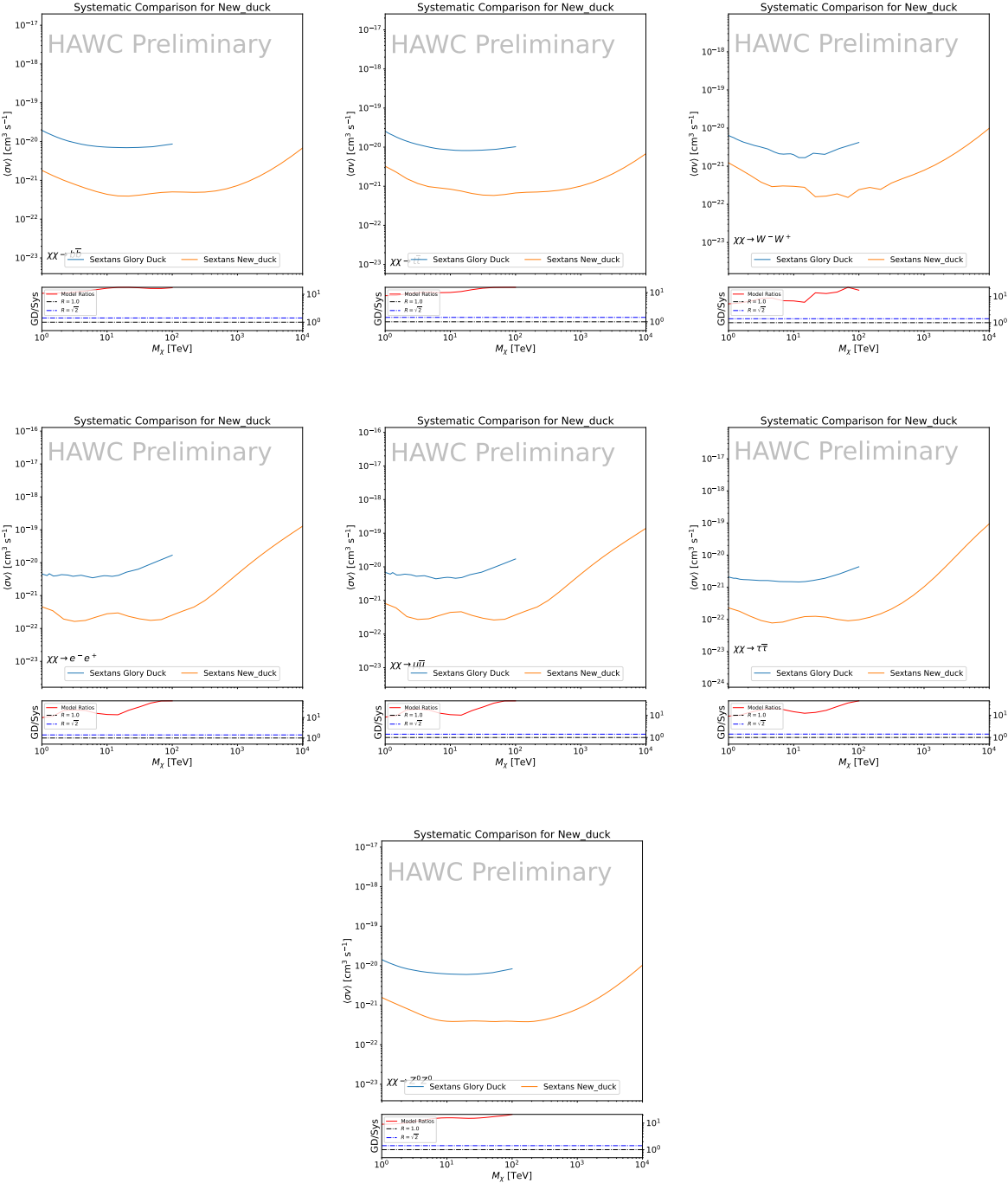


Figure B.4 TODO: fill this out

APPENDIX C

1795 ICECUBE HEAVY DARK MATTER ANALYSIS SUPPLEMENTARY MATERIAL

1796 C.1 Docker Image for Oscillating Neutrino Spectra

```
17971 FROM ubuntu:18.04
17982
17993 # Execute commands to install software packages
18004 RUN apt -y update
18015
18026     # Install utility programs
18037 RUN apt -y install vim wget git cmake
18048
18059 ARG DEBIAN_FRONTEND=noninteractive
18060
18071     # Install python
18082 RUN apt -y install python python-dev python-pip libjpeg-dev zlib1g-dev
18093
18104     # We need Python2 for installing Charon.
18115 RUN apt -y install python-numpy python-sympy python-matplotlib \
18126             python-sympy python-h5py python-astropy python-ipython
18137
18148     # Install dependencies of Charon : SQuIDS, NuSQuIDS
18159 RUN apt -y install libgsl-dev libgslcblas0 libgsl23 gsl-bin pkg-config
18160     # Install SQuIDS
18171 RUN mkdir /home/SQuIDS /home/SQuIDS_install
18182 WORKDIR /home/SQuIDS
18193 RUN git clone https://github.com/jsalvado/SQuIDS.git
18204 WORKDIR /home/SQuIDS/SQuIDS
18215 RUN git checkout 7ad9ba7c6ad06d1f0fa8418f937ebf1a403fef90
18226     # Before executing "make install" an environmental variable has to be set.
18237 ENV PKG_CONFIG_PATH=/home/SQuIDS/SQuIDS/lib
18248 RUN ./configure --prefix=../SQuIDS_install \
```

```

18259     && make
18260 RUN make install
18271
18282     # Set up an environmental variable that is required to install nuSQuIDS..
18293 ENV SQuIDS=/home/SQuIDS/SQuIDS
18304 ENV LD_LIBRARY_PATH=$SQuIDS/lib:$LD_LIBRARY_PATH
18315
18326     # Install NuSQuIDS
18337 RUN mkdir /home/nuSQuIDS
18348 WORKDIR /home/nuSQuIDS
18359 RUN git clone https://github.com/qrliu/nuSQuIDS.git
18360 WORKDIR /home/nuSQuIDS/nuSQuIDS
18371 RUN git checkout 072d8ef740e2fc7330f1fabaea94f0f4540c46f9
18382 RUN apt -y install libhdf5-dev hdf5-tools
18393 RUN apt -y install libboost1.65-all-dev
18404 RUN ./configure --with-squids=$SQuIDS --with-python-bindings --prefix=../
1841     nuSQuIDS_install \
18425     && make \
18436     && make install
18447
18458     # Set up an environmental variable for nuSQuIDS.
18469 ENV nuSQuIDS=/home/nuSQuIDS/nuSQuIDS
18470 ENV LD_LIBRARY_PATH=$nuSQuIDS/lib:$LD_LIBRARY_PATH
18481
18492     # Build the python bindings
18503 WORKDIR /home/nuSQuIDS/nuSQuIDS/resources/python/src
18514 RUN make
18525
18536     # Set up an environmental variable for the python bindings.
18547 ENV PYTHONPATH=$nuSQuIDS/resources/python/bindings/:$PYTHONPATH
18558
18569     # Install Charon in the /home/Charon/charon directory.
18570 RUN mkdir /home/Charon

```

```
18581 WORKDIR /home/Charon
18592 RUN git clone https://github.com/icecube/charon.git \
18603     && apt -y install unzip python-scipy
18614 WORKDIR charon
18625 RUN git checkout c531efe4e01dc364a60d1c83f950f04526ccd771
18636 RUN unzip ./charon/xsec/xsec.zip -d charon/xsec/ \
18647
18658 # Download neutrino spectra tables in the /home/Charon/charon/data directory
18669 .
18679     && mkdir ./charon/data
18680 WORKDIR ./charon/data
18691 RUN wget --no-check-certificate https://icecube.wisc.edu/~qliu/charon/
1870     SpectraEW.hdf5 \
18712     && wget --no-check-certificate https://icecube.wisc.edu/~qliu/charon/
1872     Spectra_PYTHIA.hdf5 \
18733     && wget --no-check-certificate https://icecube.wisc.edu/~qliu/charon/
1874     Spectra_noEW.hdf5
18754
18765 WORKDIR ../..
18776 RUN python setup.py install
18787 WORKDIR /home
```

BIBLIOGRAPHY

- [1] Anne M. Green. “Dark matter in astrophysics/cosmology”. In: *SciPost Phys. Lect. Notes* (2022), p. 37. doi: [10.21468/SciPostPhysLectNotes.37](https://doi.org/10.21468/SciPostPhysLectNotes.37). URL: <https://scipost.org/10.21468/SciPostPhysLectNotes.37>.
- [2] Bing-Lin Young. “A survey of dark matter and related topics in cosmology”. In: *Frontiers of Physics* 12 (Oct. 2016). doi: <https://doi.org/10.1007/s11467-016-0583-4>. URL: <https://doi.org/10.1007/s11467-016-0583-4>.
- [3] Gianfranco Bertone, Dan Hooper, and Joseph Silk. “Particle dark matter: evidence, candidates and constraints”. In: *Physics Reports* 405.5 (2005), pp. 279–390. issn: 0370-1573. doi: <https://doi.org/10.1016/j.physrep.2004.08.031>. URL: <https://www.sciencedirect.com/science/article/pii/S0370157304003515>.
- [4] Gianfranco Bertone and Dan Hooper. “History of dark matter”. In: *Rev. Mod. Phys.* 90 (4 Aug. 2018), p. 045002. doi: [10.1103/RevModPhys.90.045002](https://doi.org/10.1103/RevModPhys.90.045002). URL: <https://link.aps.org/doi/10.1103/RevModPhys.90.045002>.
- [5] Fritz Zwicky. “The Redshift of Extragalactic Nebulae”. In: *Helvetica Physica Acta* 6. (1933), pp. 110–127. doi: [10.5169/seals-110267](https://doi.org/10.5169/seals-110267).
- [6] Vera C. Rubin and Jr. Ford W. Kent. “Rotation of the Andromeda Nebula from a Spectroscopic Survey of Emission Regions”. In: *ApJ* 159 (Feb. 1970), p. 379. doi: [10.1086/150317](https://doi.org/10.1086/150317).
- [7] K. G. Begeman, A. H. Broeils, and R. H. Sanders. “Extended rotation curves of spiral galaxies: dark haloes and modified dynamics”. In: *Monthly Notices of the Royal Astronomical Society* 249.3 (Apr. 1991), pp. 523–537. issn: 0035-8711. doi: [10.1093/mnras/249.3.523](https://doi.org/10.1093/mnras/249.3.523). eprint: <https://academic.oup.com/mnras/article-pdf/249/3/523/18160929/mnras249-0523.pdf>. URL: <https://doi.org/10.1093/mnras/249.3.523>.
- [8] *Different types of gravitational lenses*. website. Feb. 2004. URL: <https://esahubble.org/images/heic0404b/>.
- [9] Douglas Clowe et al. “A Direct Empirical Proof of the Existence of Dark Matter”. In: *apjl* 648.2 (Sept. 2006), pp. L109–L113. doi: [10.1086/508162](https://doi.org/10.1086/508162). arXiv: [astro-ph/0608407 \[astro-ph\]](https://arxiv.org/abs/astro-ph/0608407).
- [10] Planck Collaboration and N. et. al. Aghanim. “Planck 2018 results I. Overview and the cosmological legacy of Planck”. In: *A&A* 641 (2020). doi: [10.1051/0004-6361/201833880](https://doi.org/10.1051/0004-6361/201833880). URL: <https://doi.org/10.1051/0004-6361/201833880>.
- [11] Wayne Hu. *Matter Density Animation*. web. 2024. URL: <http://background.uchicago.edu/~whu/animbut/anim2.html>.

- 1913 [12] Wenlong Yuan et al. “A First Look at Cepheids in a Type Ia Supernova Host with JWST”. in:
1914 *The Astrophysical Journal Letters* 940.1 (Nov. 2022). doi: [10.3847/2041-8213/ac9b27](https://doi.org/10.3847/2041-8213/ac9b27).
1915 URL: <https://dx.doi.org/10.3847/2041-8213/ac9b27>.
- 1916 [13] Wendy L. Freedman. “Measurements of the Hubble Constant: Tensions in Perspective”. In:
1917 *The Astrophysical Journal* 919.1 (Sept. 2021), p. 16. doi: [10.3847/1538-4357/ac0e95](https://doi.org/10.3847/1538-4357/ac0e95).
1918 URL: <https://dx.doi.org/10.3847/1538-4357/ac0e95>.
- 1919 [14] Jodi Cooley. “Dark Matter direct detection of classical WIMPs”. In: *SciPost Phys. Lect.*
1920 *Notes* (2022), p. 55. doi: [10.21468/SciPostPhysLectNotes.55](https://doi.org/10.21468/SciPostPhysLectNotes.55). URL: <https://scipost.org/10.21468/SciPostPhysLectNotes.55>.
- 1922 [15] “Search for new phenomena in events with an energetic jet and missing transverse momentum
1923 in pp collisions at $\sqrt{s} = 13$ TeV with the ATLAS detector”. In: *Phys. Rev. D* 103
1924 (11 July 2021), p. 112006. doi: [10.1103/PhysRevD.103.112006](https://doi.org/10.1103/PhysRevD.103.112006). URL: <https://link.aps.org/doi/10.1103/PhysRevD.103.112006>.
- 1926 [16] *Jetting into the dark side: a precision search for dark matter*. website. July 2020. URL:
1927 <https://atlas.cern/updates/briefing/precision-search-dark-matter>.
- 1928 [17] Celine Armand et. al. “Combined dark matter searches towards dwarf spheroidal galaxies
1929 with Fermi-LAT, HAWC, H.E.S.S., MAGIC, and VERITAS”. in: *Proceedings of Science*.
1930 Vol. 395. Mar. 2022. doi: <https://doi.org/10.22323/1.395.0528>.
- 1931 [18] Tracy R. Slatyer. “Les Houches Lectures on Indirect Detection of Dark Matter”. In: *SciPost*
1932 *Phys. Lect. Notes* (2022), p. 53. doi: [10.21468/SciPostPhysLectNotes.53](https://doi.org/10.21468/SciPostPhysLectNotes.53). URL:
1933 <https://scipost.org/10.21468/SciPostPhysLectNotes.53>.
- 1934 [19] Christian W Bauer, Nicholas L. Rodd, and Bryan R. Webber. “Dark matter spectra from
1935 the electroweak to the Planck scale”. In: *Journal of High Energy Physics* 2021.1029-8479
1936 (June 2021). doi: [https://doi.org/10.1007/JHEP06\(2021\)121](https://doi.org/10.1007/JHEP06(2021)121).
- 1937 [20] Riccardo Catena and Piero Ullio. “A novel determination of the local dark matter density”.
1938 In: *Journal of Cosmology and Astroparticle Physics* 2010.08 (Aug. 2010), p. 004. doi:
1939 [10.1088/1475-7516/2010/08/004](https://doi.org/10.1088/1475-7516/2010/08/004). URL: <https://dx.doi.org/10.1088/1475-7516/2010/08/004>.
- 1941 [21] B. P. Abbott et al. “Observation of Gravitational Waves from a Binary Black Hole Merger”.
1942 In: *Phys. Rev. Lett.* 116 (6 Feb. 2016), p. 061102. doi: [10.1103/PhysRevLett.116.061102](https://doi.org/10.1103/PhysRevLett.116.061102). URL: <https://link.aps.org/doi/10.1103/PhysRevLett.116.061102>.
- 1944 [22] R. Abbasi et. al. “Observation of high-energy neutrinos from the Galactic plane”. In: *Science*
1945 380.6652 (June 2023), pp. 1338–1343.
- 1946 [23] NASA Goddard Space Flight Center. *Fermi’s 12-year view of the gamma-ray sky*. website.

- 1947 2022. URL: <https://svs.gsfc.nasa.gov/14090>.
- 1948 [24] Marco Cirelli et al. “PPPC 4 DM ID: a poor particle physicist cookbook for dark matter
1949 indirect detection”. In: *Journal of Cosmology and Astroparticle Physics* 2011.03 (Mar.
1950 2011), p. 051. doi: [10.1088/1475-7516/2011/03/051](https://doi.org/10.1088/1475-7516/2011/03/051). URL: <https://dx.doi.org/10.1088/1475-7516/2011/03/051>.
- 1952 [25] Javier Rico. “Gamma-Ray Dark Matter Searches in Milky Way Satellites—A Comparative
1953 Review of Data Analysis Methods and Current Results”. In: *Galaxies* 8.1 (Mar. 2020), p. 25.
1954 doi: [10.3390/galaxies8010025](https://doi.org/10.3390/galaxies8010025). arXiv: [2003.13482 \[astro-ph.HE\]](https://arxiv.org/abs/2003.13482).
- 1955 [26] W. B. Atwood et al. “The Large Area Telescope on the Fermi Gamma-Ray Space Telescope
1956 Mission”. In: *apj* 697.2 (June 2009), pp. 1071–1102. doi: [10.1088/0004-637X/697/2/1071](https://doi.org/10.1088/0004-637X/697/2/1071). arXiv: [0902.1089 \[astro-ph.IM\]](https://arxiv.org/abs/0902.1089).
- 1958 [27] M. Ackermann et al. “Searching for Dark Matter Annihilation from Milky Way Dwarf
1959 Spheroidal Galaxies with Six Years of Fermi Large Area Telescope Data”. In: *prl* 115.23,
1960 231301 (Dec. 2015), p. 231301. doi: [10.1103/PhysRevLett.115.231301](https://doi.org/10.1103/PhysRevLett.115.231301). arXiv:
1961 [1503.02641 \[astro-ph.HE\]](https://arxiv.org/abs/1503.02641).
- 1962 [28] Mattia Di Mauro, Martin Stref, and Francesca Calore. “Investigating the effect of Milky
1963 Way dwarf spheroidal galaxies extension on dark matter searches with Fermi-LAT data”.
1964 In: *Phys. Rev. D* 106 (12 Dec. 2022), p. 123032. doi: [10.1103/PhysRevD.106.123032](https://doi.org/10.1103/PhysRevD.106.123032).
1965 URL: <https://link.aps.org/doi/10.1103/PhysRevD.106.123032>.
- 1966 [29] F. et al. Aharonian. “Observations of the Crab Nebula with H.E.S.S.”. In: *Astron. Astrophys.*
1967 457 (2006), pp. 899–915. doi: [10.1051/0004-6361:20065351](https://doi.org/10.1051/0004-6361:20065351). arXiv: [astro-ph/0607333](https://arxiv.org/abs/astro-ph/0607333).
- 1969 [30] J. Albert et al. “VHE γ -Ray Observation of the Crab Nebula and its Pulsar with the MAGIC
1970 Telescope”. In: *The Astrophysical Journal* 674.2 (Feb. 2008), p. 1037. doi: [10.1086/525270](https://doi.org/10.1086/525270). URL: <https://dx.doi.org/10.1086/525270>.
- 1972 [31] N. Park. “Performance of the VERITAS experiment”. In: *Proceedings, 34th International
1973 Cosmic Ray Conference (ICRC2015): The Hague, The Netherlands, July, 30th July - 6th
1974 August*. Vol. 34. 2015, p. 771. arXiv: [1508.07070 \[astro-ph.IM\]](https://arxiv.org/abs/1508.07070).
- 1975 [32] A. Abramowski et al. “H.E.S.S. constraints on Dark Matter annihilations towards the Sculptor
1976 and Carina Dwarf Galaxies”. In: *Astropart. Phys.* 34 (2011), pp. 608–616. doi: [10.1016/j.astropartphys.2010.12.006](https://doi.org/10.1016/j.astropartphys.2010.12.006). arXiv: [1012.5602 \[astro-ph.HE\]](https://arxiv.org/abs/1012.5602).
- 1978 [33] A. Abramowski et al. “Search for dark matter annihilation signatures in H.E.S.S. observations
1979 of Dwarf Spheroidal Galaxies”. In: *Phys. Rev. D* 90 (2014), p. 112012. doi: [10.1103/PhysRevD.90.112012](https://doi.org/10.1103/PhysRevD.90.112012). arXiv: [1410.2589 \[astro-ph.HE\]](https://arxiv.org/abs/1410.2589).

- 1981 [34] H. Abdalla et al. “Searches for gamma-ray lines and ‘pure WIMP’ spectra from Dark
1982 Matter annihilations in dwarf galaxies with H.E.S.S”. in: *JCAP* 11 (2018), p. 037. doi:
1983 [10.1088/1475-7516/2018/11/037](https://doi.org/10.1088/1475-7516/2018/11/037). arXiv: [1810.00995 \[astro-ph.HE\]](https://arxiv.org/abs/1810.00995).
- 1984 [35] J. Aleksić et al. “Optimized dark matter searches in deep observations of Segue 1 with
1985 MAGIC”. in: *JCAP* 1402 (2014), p. 008. doi: [10.1088/1475-7516/2014/02/008](https://doi.org/10.1088/1475-7516/2014/02/008).
1986 arXiv: [1312.1535 \[hep-ph\]](https://arxiv.org/abs/1312.1535).
- 1987 [36] V.A. Acciari et al. “Combined searches for dark matter in dwarf spheroidal galaxies observed
1988 with the MAGIC telescopes, including new data from Coma Berenices and Draco”. In: *Physics of the Dark Universe* (2021), p. 100912. issn: 2212-6864. doi: <https://doi.org/10.1016/j.dark.2021.100912>. URL: <https://www.sciencedirect.com/science/article/pii/S2212686421001370>.
- 1992 [37] M. L. Ahnen et al. “Indirect dark matter searches in the dwarf satellite galaxy Ursa Major II
1993 with the MAGIC Telescopes”. In: *JCAP* 1803.03 (2018), p. 009. doi: [10.1088/1475-7516/2018/03/009](https://doi.org/10.1088/1475-7516/2018/03/009). arXiv: [1712.03095 \[astro-ph.HE\]](https://arxiv.org/abs/1712.03095).
- 1995 [38] S. et al. Archambault. “Dark matter constraints from a joint analysis of dwarf Spheroidal
1996 galaxy observations with VERITAS”. in: *prd* 95.8 (Apr. 2017). doi: [10.1103/PhysRevD.95.082001](https://doi.org/10.1103/PhysRevD.95.082001). arXiv: [1703.04937 \[astro-ph.HE\]](https://arxiv.org/abs/1703.04937).
- 1998 [39] Louise Oakes et al. “Combined Dark Matter searches towards dwarf spheroidal galaxies with
1999 Fermi-LAT, HAWC, HESS, MAGIC and VERITAS”. in: *Proceedings of Science*. 2019.
- 2000 [40] Celine Armand et al. on behalf of the Fermi-LAT, HAWC, HESS, MAGIC, VERITAS.
2001 “Combined Dark Matter searches towards dwarf spheroidal galaxies with Fermi-LAT,
2002 HAWC, HESS, MAGIC and VERITAS”. in: *Proceedings of Science*. 2021.
- 2003 [41] Daniel Kerszberg et al. on behalf of the Fermi-LAT, HAWC, HESS, MAGIC, and VER-
2004 TIAS collaborations. “Search for dark matter annihilation with a combined analysis of
2005 dwarf spheroidal galaxies from Fermi-LAT, HAWC, H.E.S.S., MAGIC and VERITAS”. in:
2006 *Proceedings of Science*. 2023.
- 2007 [42] A. U. Abeysekara et al. “Observation of the Crab Nebula with the HAWC Gamma-Ray
2008 Observatory”. In: *The Astrophysical Journal* 843.1 (June 2017), p. 39. doi: [10.3847/1538-4357/aa7555](https://doi.org/10.3847/1538-4357/aa7555). URL: <https://doi.org/10.3847/1538-4357/aa7555>.
- 2010 [43] Giacomo Vianello et al. *The Multi-Mission Maximum Likelihood framework (3ML)*. 2015.
2011 arXiv: [1507.08343 \[astro-ph.HE\]](https://arxiv.org/abs/1507.08343).
- 2012 [44] Marco Cirelli et al. “PPPC 4 DM ID: a poor particle physicist cookbook for dark matter
2013 indirect detection”. In: *Journal of Cosmology and Astroparticle Physics* 2011.03 (Mar.
2014 2011). issn: 1475-7516. doi: [10.1088/1475-7516/2011/03/051](https://doi.org/10.1088/1475-7516/2011/03/051). URL: <http://dx.doi.org/10.1088/1475-7516/2011/03/051>.

- 2016 [45] Alex Geringer-Sameth, Savvas M. Koushiappas, and Matthew Walker. “DWARF GALAXY
 2017 ANNIHILATION AND DECAY EMISSION PROFILES FOR DARK MATTER EXPERI-
 2018 MENTS”. in: *The Astrophysical Journal* 801.2 (Mar. 2015), p. 74. ISSN: 1538-4357. doi:
 2019 [10.1088/0004-637X/801/2/74](https://doi.org/10.1088/0004-637X/801/2/74). URL: <http://dx.doi.org/10.1088/0004-637X/801/2/74>.
- 2021 [46] A. Albert et al. “Dark Matter Limits from Dwarf Spheroidal Galaxies with the HAWC
 2022 Gamma-Ray Observatory”. In: *The Astrophysical Journal* 853.2 (Feb. 2018), p. 154. ISSN:
 2023 1538-4357. doi: [10.3847/1538-4357/aaa6d8](https://doi.org/10.3847/1538-4357/aaa6d8). URL: <http://dx.doi.org/10.3847/1538-4357/aaa6d8>.
- 2025 [47] V. Bonnivard et al. “Spherical Jeans analysis for dark matter indirect detection in dwarf
 2026 spheroidal galaxies - Impact of physical parameters and triaxiality”. In: *Mon. Not. Roy.
 2027 Astron. Soc.* 446 (2015), pp. 3002–3021. doi: [10.1093/mnras/stu2296](https://doi.org/10.1093/mnras/stu2296). arXiv:
 2028 [1407.7822 \[astro-ph.HE\]](https://arxiv.org/abs/1407.7822).
- 2029 [48] M. Ackermann et al. “Searching for Dark Matter Annihilation from Milky Way Dwarf
 2030 Spheroidal Galaxies with Six Years of Fermi Large Area Telescope Data”. In: *prl* 115.23,
 2031 231301 (Dec. 2015), p. 231301. doi: [10.1103/PhysRevLett.115.231301](https://doi.org/10.1103/PhysRevLett.115.231301). arXiv:
 2032 [1503.02641 \[astro-ph.HE\]](https://arxiv.org/abs/1503.02641).
- 2033 [49] M. L. Ahnen et al. “Limits to Dark Matter Annihilation Cross-Section from a Combined
 2034 Analysis of MAGIC and Fermi-LAT Observations of Dwarf Satellite Galaxies”. In: *JCAP*
 2035 1602.02 (2016), p. 039. doi: [10.1088/1475-7516/2016/02/039](https://doi.org/10.1088/1475-7516/2016/02/039). arXiv: [1601.06590](https://arxiv.org/abs/1601.06590)
 2036 [astro-ph.HE].
- 2037 [50] Javier Rico et al. *gLike: numerical maximization of heterogeneous joint
 2038 likelihood functions of a common free parameter plus nuisance parameters*.
<https://doi.org/10.5281/zenodo.4601451>. Version v0.09.03. Mar. 2021. doi: [10.5281/zenodo.4601451](https://doi.org/10.5281/zenodo.4601451). URL: <https://doi.org/10.5281/zenodo.4601451>.
- 2041 [51] Tjark Miener and Daniel Nieto. *LklCom: Combining likelihoods from different experiments*.
<https://doi.org/10.5281/zenodo.4597500>. Version v0.5.3. Mar. 2021. doi: [10.5281/zenodo.4597500](https://doi.org/10.5281/zenodo.4597500). URL: <https://doi.org/10.5281/zenodo.4597500>.
- 2044 [52] T. Miener et al. “Open-source Analysis Tools for Multi-instrument Dark Matter Searches”.
 2045 In: *arXiv e-prints*, arXiv:2112.01818 (Dec. 2021), arXiv:2112.01818. arXiv: [2112.01818](https://arxiv.org/abs/2112.01818)
 2046 [astro-ph.IM].
- 2047 [53] Alex Geringer-Sameth and Matthew Koushiappas Savvas M. and Walker. “Dwarf galaxy
 2048 annihilation and decay emission profiles for dark matter experiments”. In: *Astrophys.
 2049 J.* 801.2 (2015), p. 74. doi: [10.1088/0004-637X/801/2/74](https://doi.org/10.1088/0004-637X/801/2/74). arXiv: [1408.0002](https://arxiv.org/abs/1408.0002)
 2050 [astro-ph.CO].
- 2051 [54] Gianfranco Bertone, Dan Hooper, and Joseph Silk. “Particle dark matter: evidence, can-

- 2052 didates and constraints”. In: *Physics Reports* 405.5-6 (Jan. 2005), pp. 279–390. ISSN:
2053 0370-1573. doi: [10.1016/j.physrep.2004.08.031](https://doi.org/10.1016/j.physrep.2004.08.031). URL: <http://dx.doi.org/10.1016/j.physrep.2004.08.031>.
- 2055 [55] V. Bonnivard et al. “Dark matter annihilation and decay in dwarf spheroidal galaxies: The
2056 classical and ultrafaint dSphs”. In: *Mon. Not. Roy. Astron. Soc.* 453.1 (2015), pp. 849–867.
2057 doi: [10.1093/mnras/stv1601](https://doi.org/10.1093/mnras/stv1601). arXiv: [1504.02048 \[astro-ph.HE\]](https://arxiv.org/abs/1504.02048).
- 2058 [56] A. et al. Albert. “Searching for Dark Matter Annihilation in Recently Discovered Milky Way
2059 Satellites with Fermi-LAT”. in: *Astrophys. J.* 834.2 (2017), p. 110. doi: [10.3847/1538-4357/834/2/110](https://doi.org/10.3847/1538-4357/834/2/110). arXiv: [1611.03184 \[astro-ph.HE\]](https://arxiv.org/abs/1611.03184).
- 2061 [57] Mattia Di Mauro and Martin Wolfgang Winkler. “Multimessenger constraints on the dark
2062 matter interpretation of the Fermi-LAT Galactic Center excess”. In: *prd* 103.12, 123005
2063 (June 2021), p. 123005. doi: [10.1103/PhysRevD.103.123005](https://doi.org/10.1103/PhysRevD.103.123005). arXiv: [2101.11027 \[astro-ph.HE\]](https://arxiv.org/abs/2101.11027).
- 2065 [58] HongSheng Zhao. “Analytical models for galactic nuclei”. In: *Mon. Not. Roy. Astron. Soc.*
2066 278 (1996), pp. 488–496. doi: [10.1093/mnras/278.2.488](https://doi.org/10.1093/mnras/278.2.488). arXiv: [astro-ph/9509122 \[astro-ph\]](https://arxiv.org/abs/astro-ph/9509122).
- 2068 [59] H. C. Plummer. “On the Problem of Distribution in Globular Star Clusters: (Plate 8.)”
2069 In: *Monthly Notices of the Royal Astronomical Society* 71.5 (Mar. 1911), pp. 460–470.
2070 ISSN: 0035-8711. doi: [10.1093/mnras/71.5.460](https://doi.org/10.1093/mnras/71.5.460). eprint: <https://academic.oup.com/mnras/article-pdf/71/5/460/2937497/mnras71-0460.pdf>. URL:
2072 <https://doi.org/10.1093/mnras/71.5.460>.
- 2073 [60] Daniel R. Hunter. “Derivation of the anisotropy profile, constraints on the local velocity
2074 dispersion, and implications for direct detection”. In: *JCAP* 02 (2014), p. 023. doi:
2075 [10.1088/1475-7516/2014/02/023](https://doi.org/10.1088/1475-7516/2014/02/023). arXiv: [1311.0256 \[astro-ph.CO\]](https://arxiv.org/abs/1311.0256).
- 2076 [61] Barun Kumar Dhar and Liliya L. R. Williams. “Surface mass density of the Einasto family
2077 of dark matter haloes: are they Sersic-like?” In: *Mon. Not. Roy. Astron. Soc.* (2010). doi:
2078 [10.1111/j.1365-2966.2010.16446.x](https://doi.org/10.1111/j.1365-2966.2010.16446.x).
- 2079 [62] M. Baes and E. Van Hese. “Dynamical models with a general anisotropy profile”. In:
2080 *Astron. Astrophys.* 471 (2007), p. 419. doi: [10.1051/0004-6361:20077672](https://doi.org/10.1051/0004-6361:20077672). arXiv:
2081 [0705.4109 \[astro-ph\]](https://arxiv.org/abs/0705.4109).
- 2082 [63] Matthew G. Walker, Edward W. Olszewski, and Mario Mateo. “Bayesian analysis of re-
2083 solved stellar spectra: application to MMT/Hectochelle observations of the Draco dwarf
2084 spheroidal”. In: *mnras* 448.3 (Apr. 2015), pp. 2717–2732. doi: [10.1093/mnras/stv099](https://doi.org/10.1093/mnras/stv099).
2085 arXiv: [1503.02589 \[astro-ph.GA\]](https://arxiv.org/abs/1503.02589).
- 2086 [64] Nicholas L. Rodd et al. “Dark matter spectra from the electroweak to the Planck scale”. In:

- 2087 *J. High Energy Physics* 121.10.1007 (June 2021).
- 2088 [65] Pace, Andrew B and Strigari, Louis E. “Scaling relations for dark matter annihilation and
2089 decay profiles in dwarf spheroidal galaxies”. In: *Monthly Notices of the Royal Astronomical
2090 Society* 482.3 (Oct. 2018), pp. 3480–3496. ISSN: 0035-8711. doi: [10.1093/mnras/sty2839](https://doi.org/10.1093/mnras/sty2839).
- 2092 [66] Albert, A. et al. “Search for gamma-ray spectral lines from dark matter annihilation in
2093 dwarf galaxies with the High-Altitude Water Cherenkov observatory”. In: *Phys. Rev. D* 101 (10 May 2020), p. 103001. doi: [10.1103/PhysRevD.101.103001](https://doi.org/10.1103/PhysRevD.101.103001). URL:
2094 <https://link.aps.org/doi/10.1103/PhysRevD.101.103001>.
- 2096 [67] Victor Eijkhout and Edmund Show and Robert van de Geijn. *The Science of Computing.
2097 The Art of High Performance Computing*. Vol. 3. Open Copy published under CC-BY 4.0
2098 license, 2023, pp. 63–66.
- 2099 [68] Qinrui Liu and Jeffrey Lazar and Carlos A. Argüelles and Ali Kheirandish. “ χ aro: a tool
2100 for neutrino flux generation from WIMPs”. In: *Journal of Cosmology and Astroparticle
2101 Physics* 2020.10 (Oct. 2020), p. 043. doi: [10.1088/1475-7516/2020/10/043](https://doi.org/10.1088/1475-7516/2020/10/043). URL:
2102 <https://dx.doi.org/10.1088/1475-7516/2020/10/043>.